January 2021

Impacts Of Vertical Grid Resolution On The Representation Of A Convective Environment

Caitlyn Mensch

Follow this and additional works at: https://commons.und.edu/theses

IMPACTS OF VERTICAL GRID RESOLUTION ON THE REPRESENTATION OF A
CONVECTIVE ENVIRONMENT

by

Caitlyn Ann Mensch
Bachelor of Science, State University of New York at Oswego, 2017

A Thesis
Submitted to the Graduate Faculty

of the

University of North Dakota

in partial fulfillment of the requirements

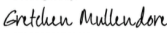for the degree of
Master of Science

Grand Forks, North Dakota

May
2021

Name: Caitlyn Mensch

Degree: Master of Science

This document, submitted in partial fulfillment of the requirements for the degree from the University of North Dakota, has been read by the Faculty Advisory Committee under whom the work has been done and is hereby approved.
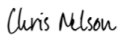
DocuSigned by:

Gretchen Mullendore
8F8CCA74AE4A495...

Gretchen Mullendore

DocuSigned by:

7765189778979460...

Aaron Kennedy

DocuSigned by:

Catherine Finley
9AB347FA88FB427...

Catherine Finley

This document is being submitted by the appointed advisory committee as having met all the requirements of the School of Graduate Studies at the University of North Dakota and is hereby approved.

DocuSigned by:

Chris Nelson
2E0AE088C733403...

Chris Nelson
Dean of the School of Graduate Studies

5/7/2021

Date

PERMISSION

Title   Impacts of Vertical Grid Resolution on the Representation of a Convective Environment

Department   Atmospheric Sciences

Degree   Master of Science

In presenting this thesis in partial fulfillment of the requirements for a graduate degree from the University of North Dakota, I agree that the library of this University shall make it freely available for inspection. I further agree that permission for extensive copying for scholarly purposes may be granted by the professor who supervised my thesis work or, in his absence, by the Chairperson of the department or the dean of the School of Graduate Studies. It is understood that any copying or publication or other use of this thesis or part thereof for financial gain shall not be allowed without my written permission. It is also understood that due recognition shall be given to me and to the University of North Dakota in any scholarly use which may be made of any material in my thesis.

<div align="right">

Caitlyn Ann Mensch
May 7 2021

</div>

TABLE OF CONTENTS

LIST OF FIGURES

LIST OF TABLES

ACKNOWLEDGMENTS

I would like to thank my thesis advisor, Gretchen Mullendore, for the amazing amount of help and support. I would also like to thank my committee members, Aaron Kennedy and Catherine Finley for their helpful comments and edits throughout the thesis process.

Additionally, I would like to thank Clark Evans at University of Milwaukee for the helpful feedback during the process of this project and Emily Archer, a UND student, for helping with the quality control processing specific to this project. I would also like to thank NCAR EOL and the ARM Data Center for the availability, processing, and quality control of the sounding datasets utilized. Also, I'd like to thank the ARM Mobile Facility (MAO) Manacapuru, Amazonas, Brazil; AMF1 (M1) and the ARM Data Center for collection and processing of sounding data.

Lastly, I would like to thank my family and friends who have supported me throughout this process. 2020 and 2021 have been challenging years, but I am thankful for the continued support that enabled me to successfully finish this project. I'd also like to thank the wonderful group of graduate students at UND for their support

ABSTRACT

In a pre-convective environment, modeled atmospheric conditions can be presented as discrete parameters, which serve as valuable resources both in forecasting potential severe weather events and also in assessing changes in convective potential over time. However, the value of these parameters may depend on the vertical resolution of the simulation that is used to do the calculation. Upper-air radiosonde sounding data from various research campaigns (e.g., PECAN, DC3, TRMM-LBA, etc.) in both midlatitude and tropical convective regimes are analyzed and later interpolated to the pressure levels in a range of atmospheric reanalysis and operational models. Indices such as CAPE, CIN, bulk shear, and strength of capping inversion are then calculated using both the raw sounding and the interpolated soundings. Interpolated soundings consistently underestimated CAPE, although models with a larger number of vertical levels underestimated CAPE less (e.g., ERA5). Kinematic parameters; however, were well correlated to the observed. The accurate representation of the capping inversion was found to be sensitive to both the number and distribution of levels in the first several kilometers. Increasing vertical resolution from previous model versions, may improve accuracy of parameters (e.g., ERA5, GFSv16). Based on vertical resolution alone, this study shows that decreased vertical resolution can impact the ability of convective parameters to represent a potentially convective environment.

CHAPTER 1

INTRODUCTION

There are a large number of hazards associated with storms. Accurate forecasting of these storms can help mitigate the public safety risks. Forecasters use both observations and model guidance to predict potentially hazardous weather. It is also important for forecasters to understand the model limitations when analyzing model guidance. Calculated convective parameters are commonly used by forecasters as a supplementary resource in their convective forecasting procedure. These parameters serve as proxies to help identify how favorable an environment is for convection (Craven and Brooks 2004). The accuracy of thermodynamic (e.g., CAPE, CIN) and kinematic (e.g., bulk shear) indices as well as structures such as the capping inversion strongly depend on the data provided in the vertical profile.

In forecasted convective parameters, the accuracy will in part depend on the number of data points in the profile. For example, sharp changes in the vertical profile may be inaccurately represented if the model vertical resolution is too coarse. When a model has a relatively coarse resolution, it is less likely that smaller-scale atmospheric features will be resolved. Numerous studies have investigated the impacts of grid resolution on the simulation of convection (e.g., Bryan et al. 2003, Homeyer 2015, Aligo et al. 2009, Barber et al. 2017). Not surprisingly, these studies have shown that the small-scale features of these phenomena are better represented at higher grid resolution.

In addition to forecast models, reanalysis models have proven to be vital tools when analyzing long-term trends in convective environments and the relationships between

convection and synoptic patterns. Reanalysis models intake various types of observations and place them on a spaced grid also accompanied by gridded model data (Kalnay and Coauthors 1996). This fills in the "holes" which may result from sparse observations thus providing a more consistent representation of a region (King and Kennedy 2019). These characteristics make reanalysis models favorable for analyzing long-term trends in distributions of optimal convective environments. Reanalysis models have been used in various climatological studies that investigated favorable convective environments (e.g., Brooks et al. 2003; Gensini and Ashley 2011; Romero et al. 2007; Taszarek et al).

However, like operational models, reanalysis models have limited vertical resolution. Although coarse vertical resolution may present few issues in general climatological studies, it may be a limitation to consider for a convective climatologies. Previous studies using reanalysis data have mentioned that lower vertical resolution may contribute to issues regarding representation of a convective environment (e.g., King and Kennedy 2019; Gensini et al. 2014; Coniglio and Parker 2020).

Correct representation of convective parameters and thus the overall convective environment is important both for forecasting and for analysis of past events. It is hypothesized that the accuracy of these measurements may be impacted in model output with limited vertical resolution. This study will investigate the impacts of vertical resolution on calculated parameters in order to provide additional insight on limitations of select reanalysis and operational models. Unlike past research, this study will use high-resolution soundings from both midlatitude and tropical field campaigns and coarsen the grid spacing to match the resolution of selected operational and reanalysis models. This approach

uniquely identifies biases that are due to resolution only, and not due to other model issues

that cause misrepresentation of convective features (e.g., parameterization issues).

CHAPTER 2

BACKGROUND

2.1. Overview

From both an operational and research perspective, atmospheric models are a valuable tool to evaluate the potential for convection or characteristics of a convective environment. As discussed in Chapter 1, it is important when analyzing model data to be aware of the data limitations. Coarse vertical resolution is hypothesized to impact representativeness of the environment, especially relating to variables that vary in the vertical profile. Convective parameters are calculated from the vertical profile and serve as proxies in assessing convective potential as well as other related aspects. The impacts of reduced vertical grid resolution will be further investigated in this study.

Section 2.2 presents an overview of previous research studies that relate to this project. Specifically, both a review of studies that have utilized model profiles to investigate convective environments and also findings from studies that highlighted the impacts of vertical resolution. The remaining sections provide additional background on the indices and structures that will be calculated for this project: common convective parameters (2.3), capping inversion (2.4), and level of neutral buoyancy (2.5).

2.2. Previous Research

Atmospheric reanalyses and operational models are both used to help identify long term trends and distributions of favorable convective environments and associated synoptic patterns e.g., Brooks et al. 2003; Gensini and Ashley 2011; Romero et al. 2007; Taszarek

et al 2020). While operational models are utilized for forecasting purposes, reanalyses models are utilized in the research sector.

Previous studies have mentioned the importance of sufficient vertical resolution on representativeness of the convective environment (e.g., King and Kennedy 2019; Gensini et al. 2014; Coniglio and Parker 2020). King and Kennedy (2019) remarked on sufficient vertical resolution being one of the several important factors when representing a convective environment accurately. This study evaluated the performance of various model reanalyses in representing North American supercell environments by comparing RUC-2 soundings to the nearest grid point derived sounding from atmospheric reanalyses. Parameters such as convective available potential energy (CAPE), convective inhibition (CIN), bulk wind difference (BWD), storm relative helicity (SRH) and other supercell-related parameters were calculated across selected reanalyses models. When compared to higher resolution RUC-2 model, negative biases were consistently found in the thermodynamic variables (e.g., CAPE) while kinematic variables (e.g., BWD) were more accurately represented. Coniglio and Parker (2020) used observational radiosonde data to gain insight on supercell environments. The limited vertical resolution associated with RUC/RAP model soundings was mentioned as a limiting factor when accurately representing a convective environment. Radiosonde observations from research campaigns were utilized in the study in order to ensure high resolution data and therefore more accurate representation of the vertical profile.

Other studies have studies further investigated the impacts of vertical resolution on representation of a convective environment (Gensini et al. 2014; Gartzke et al. 2017). In Gensini et al. (2014), proximity soundings derived from North American Regional

Reanalysis (NARR) were compared to collocated observational soundings. This study hypothesized that limited vertical resolution in reanalyses models may have contributed to the noted biases in calculated convective parameters in past studies. The study concluded that NARR calculated thermodynamic parameters exhibited the most biases and recommended analyzing NARR sounding calculations with caution due to issues resolving sharp changes in the profile. Gartzke et al. (2017) calculated CAPE from satellite, reanalysis, and smoothed radiosonde profiles and compared values with CAPE calculated from radiosonde soundings to better understand the impacts of reduced vertical resolution. Analysis of CAPE distributions found underestimations of CAPE in satellite and reanalysis data when compared to ARM-radiosonde calculated values.

2.3. Common Convective Parameters

Convective parameters are values derived from vertical atmospheric profiles that can aid in assessing the potential for severe weather, including instability, moisture, and lift. Vertical wind shear, in sufficient amounts, can also play a role in the maintenance of convection (Rotunno et al. 1988). Parameters such as CAPE, CIN, and vertical wind shear (e.g., 0-1 km, 0-3 km, 0-6 km) have shown to be vital in analyzing a potential severe storm environment. These practical calculations assess a wide range of meteorological aspects that can create a sufficient environment for convection. Convective available potential energy (CAPE) measures the vertically integrated buoyant energy of a rising air parcel thus quantifying the energy available if convection were to initiate (Blanchard 1998; Doswell and Rasmussen 1994). In other words, CAPE expresses the instability of an environment. Convective inhibition (CIN, Colby 1984) is a measure of the vertically integrated negative buoyant energy (Doswell and Rasmussen 1994). Rising air parcels must overcome the

negatively buoyant air in order to reach the level of free convection (LFC) and under the right atmospheric conditions, initiate convection.

Vertical wind shear measures how the wind magnitude and direction of the wind profile changes with height. Derived from vertical shear, the bulk-shear parameter calculates the bulk wind difference in a specified layer (e.g.,0-6 km, 0-3 km AGL). Storm type, organization, and longevity have been shown to be dependent on the environmental vertical wind shear profile. In a convectively favorable environment, larger magnitude of shear can enhance convective organization thus increasing the life-span of a storm if convection initiated (Rotunno et al. 1988; Weisman and Klemp 1982).

2.3. Capping Inversion

A common structure in the vertical profile related to convection initiation is the capping inversion. The capping inversion can be identified by a steeper positive lapse rate over some depth in the atmosphere (Coniglio et al. 2013). This stable layer of relatively warmer air "caps" the boundary layer below it by inhibiting vertical motion (i.e., rising parcels remain colder than the environment). In certain cases, if a capping inversion is strong it will allow large amounts of CAPE to build and once CIN is overcome convection can initiate (Markowski and Richardson 2010). A capping inversion can suppress initiation of convection in a favorable environment while also allowing additional moisture to build in the boundary layer below. Once this inversion is overcome or "broken", convection can rapidly develop. As a result, the capping inversion serves as an additional index that can help assess the potential for a convective environment, particularly severe convection. Given that the capping inversion is a structure identifiable in and based on the vertical profile, lower vertical resolution may impact its ability to be represented.

7

Studies have been conducted analyzing the performance of numerical models on the depiction of the capping inversion. Comparisons of WRF forecasts to radiosonde date in to test PBL schemes concluded that strong capping inversion cases tended to correspond to underestimated MLCIN valued due to a smoothed profile (Coniglio et al. 2013). In a mesoscale modeling study by Hanna and Yang (2001), output data from previous studies were utilized to evaluate performance of mesoscale models for boundary layer and near-surface measurements. A dataset obtained from Tesche and McNally (1999), contained MM5 and RAMS data for periods during the Lake Michigan Ozone Study. Models used to simulate the boundary layer had varying vertical grid increments within the first 1000 m; with 10 m at the surface then decreasing to 200 m at a height of 1000 m. Despite using relatively fine vertical resolution, the model simulated capping inversion was weaker than the observed (radiosonde data). This was noted to be a result of the decrease in vertical grid spacing towards 1000 m decreasing ability to accurately resolution a small depth structure. Another study by Coniglio et al. (2013) focused on the performance of numerical models in representing the planetary boundary layer (PBL). Vertical profiles were evaluated from WRF simulations with differing PBL schemes. Analysis of the model output and observed soundings showed that model forecasts with differing PBL schemes "damped" the capping inversion in the strong cap cases. Model-related factors contributing to a weakened capping inversion were further investigated in Burlingame et al. (2017) and Nevius and Evans (2018). Different planetary boundary layer schemes were evaluated in Burlingame et al. (2017) to determine if they had an impact on the representation of the capping inversion; however, no one scheme resulted in a significant improvement. The potential of implicit damping by third-order-accurate vertical advection schemes were investigated in Nevius

and Evans (2018) to determine if it was responsible mechanism for smoothing of the capping inversion. Results displayed that usage of a fourth-order scheme did not improve the cap, but did demonstrate that the capping inversions were consistently weak meaning that other damping mechanisms could be responsible for the visible smoothing of the cap.

2.3. Level of Neutral Buoyancy

The level of neutral buoyancy (LNB), also known as the equilibrium level, is defined to be the level at which an idealized parcel begins to decelerate and the parcel becomes less buoyant than the environment. This structure has been used as a proxy for storm structure, updraft strength/depth, and estimating detrainment levels (Mullendore et al. 2013). The level of maximum detrainment (LMD), is defined as the level at which maximum mass is detrained (Mullendore et al. 2009). The LMD is a level vital to the mass transport of atmospheric constituents during deep convection. The relationship between the LMD and the LNB is important to understanding how well parcel theory represents the observed storms. Therefore, the LNB must be accurately depicted in order to properly assess this relationship.

Previous studies have evaluated the performance of reanalyses models and operational models in representing the tropopause, a structure often used as a proxy for LNB (e.g., Starzec et al. 2020). Solomon et al. (2016) and Homeyer et al. (2010) compared radiosonde data to model data. In a small percentage of cases, ERA-Interim was unable to correctly represent the tropopause (Solomon et al. 2016). The GFS approximated the tropopause relatively well in most cases with RMS differences around 600 m for tropopause height (Homeyer et al. 2010). Both studies found a cluster of cases noted where model analysis overestimated the tropopause height. These larger errors, collocated with the

9

subtropical jet (and often double-tropopause structures), were surmised to be a result of low

vertical resolution and weakness of the stability in some cases.

CHAPTER 3

METHODOLOGY

3.1. Sounding Data

Radiosondes are launched regularly in order obtain real-time data of the vertical profile of the atmosphere. This provides extensive atmospheric information that can be input into numerical weather prediction models to improve predictability. Soundings also provide detailed analysis of the local environment which have proven to be vital in assessing convective environments. In particular, soundings are used to calculate convective-related parameters. The impacts of vertical resolution on these convective parameters will be assessed by interpolating sounding observations to the vertical levels used by each model (in some cases, both raw and coarsened output resolutions will be considered).

3.1.1. Research Campaigns

Most radiosonde observations for this study were obtained from the NCAR Earth Observing Laboratory (EOL) field project data archive with one dataset obtained from the Atmospheric Radiation Measurement (ARM) data archive. Datasets were retrieved from several field campaigns that were conducted in various geographical areas. Campaign datasets were divided into two categories: Midlatitude ($\varphi > 30°$) and tropical ($\varphi < 30°$) regimes. Table 1 lists the campaigns that will be utilized in this study along with the corresponding number of sounding utilized from each campaign. With the exception of TRMM-LBA, sample sizes exceeded 500 soundings per dataset. Importantly, these datasets consisted of high-resolution soundings which serve as "ground-truth" once they are later interpolated to vertical model levels. Brief summaries of the campaigns are provided below:

11

- Plains Elevated Convection at Night (PECAN; Geerts and Coauthors 2017): This campaign was conducted from June 2015 to Mid-July 2015. The resulting Multi-Network Composite Highest Resolution Upper Air dataset was used for analysis in this project. This dataset contains high resolution sounding data came from several sounding platforms including the National Weather Service. Sounding observations were taken in the United States, with the majority centralized over the Great Plains region (Fig. 1). Data was collected prior to nighttime severe convection to gain additional information on nocturnal convective initiation, growth processes, and prediction (UCAR/NCAR - Earth Observing Laboratory. 2017. Multi-Network Composite Highest Resolution Radiosonde Data).

- Deep Convective Clouds and Chemistry Project (DC3; Barth et al. 2015): This field campaign investigated the deep convection in the midlatitudes from May 2012 to June 2012, focusing on the impacts of deep convective clouds and lightning processes on composition of the upper tropospheric structure and chemistry. The resulting Multi-Network Composite Highest Resolution Upper Air dataset was used for analysis in this project. Data from multiple sounding platforms including the National Weather Service was used and majority of sounding data was sampled in the central United States (Fig. 1). Sounding data was high resolution containing 1-2 second resolution (UCAR/NCAR - Earth Observing Laboratory. 2013. Multi-Network Composite Highest Resolution Upper Air Data).

- Verification of the Origins of Rotation in Tornadoes Experiment 2 (VORTEX2; Wurman et al. 2012): This campaign was conducted to better understand tornado formation, structure, strength, and longevity. From May 2009 to June 2010, detailed

observations were taken in tornadic events to better understanding tornados thus improving future forecasts and warnings. For this project, the multi-network composite highest resolution upper air data set was used consisting of multiple sounding platforms including the National Weather Service. Most of the soundings had 1-2 second resolution was taken in the central United States (Fig. 1; UCAR/NCAR - Earth Observing Laboratory. 2010. Multi-Network Composite Highest Resolution Upper Air Data).

- Observations and Modeling of the Green Ocean Amazon (GOAMAZON; Martin et al. 2016): This campaign was conducted from January 2014 to November 2015 to gain observations to better understand and model tropical convection. Sounding observations were taken downwind of Manaus, Brazil (Fig. 1; Atmospheric Radiation Measurement (ARM) user facility. 2014, SONDEWNPN. ARM Mobile Facility (MAO), Manacapuru, Amazonas, Brazil; AMF1 (M1). Compiled by E. Keeler, R. Coulter, J. Kyrouac and D. Holdridge. ARM Data Center. http://dx.doi.org/10.5439/1021460.). Data was retrieved from the Atmospheric Radiation Measurement (ARM) Climate Research Facility, a U.S. Department of Energy Office of Science user facility sponsored by the Office of Biological and Environmental Research.

- Dynamics of the Madden-Julien Oscillation (DYNAMO; Yoneyama et al. 2013): This campaign was conducted from October 2011 to March 2012 in order to further analyze the MJO initiation processes and prediction of the MJO. Retrieval of sounding observations took place in the central equatorial region of the Indian Ocean (Fig. 2). Given the large selection of sounding data sites, upon

recommendation, 6 high resolution sounding sites were selected. Coastal sites include Diego Garcia (UCAR/NCAR- Earth Observing Laboratory. 2012), Gan ARM (UCAR/NCAR - Earth Observing Laboratory. 2012), Gan MMS (UCAR/NCAR - Earth Observing Laboratory. 2013), and Male (UCAR/NCAR - Earth Observing Laboratory. 2012). Ship observations are: R/V Revelle (UCAR/NCAR-Earth Observing Laboratory. 2014) and R/V Mirai (Yoneyama, K., Japan Agency for Marine-Earth Science and Technology (JAMSTEC). 2013).

- <u>Tropical Rainfall Measuring Mission - Large Scale Biosphere-Atmosphere Experiment in Amazonia</u> (TRMM-LBA; Simpson et al. 1988): This research campaign was conducted in Amazonia (Brazil) from 1 November 1998 to 28 February 1999 (Fig. 1). The goal of the campaign was to analyze processes associated with tropical convection. Radiosonde data collected from enhanced sites (Rebio-Jaru, Rolim de Moura, Rancho Grande) using 1-mb or less vertical sampling interval (Halverson et al. 2002) was utilized in this study (UCAR/NCAR - Earth Observing Laboratory, Ciesielski, P. 2019).

3.1.2. Quality Control of Campaign Datasets

Both NCAR/ EOL and DOE ARM sounding datasets underwent data quality control procedures prior to release. Missing value codes for data points of variables were processed. In the instance that one level had a missing value for a variable, the other values at that level were taken out for consistency purposes. The thermodynamic convective parameters in this study were calculated using the Sounding and Hodograph Analysis and Research Program in Python (SHARPpy) software package (Blumberg et al. 2017). During the initial CAPE calculation of the datasets, some errors were yielded from the package. As a result,

additional quality control was completed on the downloaded datasets prior to data analysis through a set of manually coded data-checks. The nature of the high-resolution datasets with many data point posed the potential for small changes in variables. These small oscillations in values triggered error flags in SHARPpy when calculating thermodynamic variables such as CAPE, yielding value errors "temperature must be monotonically increasing or monotonically decreasing". A percentage of the soundings yielding the error were associated with data points in the tropopause region. For midlatitude soundings only, the soundings were cut off at 15 km in efforts to decrease the instance of this error. This was not performed on the tropical datasets due to the tropopause region being at a much higher altitude.

Invalid height data error messages were also flagged by SHARPy as well. After further error checking, sections of no change in height (Δz) and negative Δz were present in the flagged soundings at different locations in the profile. Further quality control was done to remove soundings that were under 8 km. An additional error was caused by parcel trajectory processing of vertical profiles were that the number of vertical levels no long matched among the derived variables. What exactly caused this to happen was not diagnosed; there was no clear sounding type that caused the error and the removal of these soundings did not negatively affect the overall sample size of the soundings to be analyzed.

There were also errors that were specific to the datasets analyzed:

- <u>TRMM-LBA</u>: Errors regarding repeat height values were flagged by SHARPpy for the ABRACOS enhanced sounding site. After further investigation, surface data did contain repeat height values. In Halverson et al. (2002), issues with humidity and temperature profiles in this set of soundings were mentioned as well. Given

these factors, data from this site was not used for this study. In the remaining three sounding sites, (see field campaign details above), dewpoint temperature measurements were not originally provided in the sounding data, so this was calculated using a MetPy function. Additionally, wind data was excluded from analysis for the TRMM-LBA dataset due to larger amounts of missing wind data; therefore, bulk shear variations were not calculated.

- GOAMAZON: Some issues with data at the surface were investigated for the GOAMAZON sounding dataset. In a small number of soundings analyzed, invalid temperature data was found at the surface (Fig. 3). This resulted in visible issues in calculations of some of the convective parameters such as capping inversion strength, so soundings that presented these issues were not used.

- VORTEX2: A batch of soundings was excluded due to lower resolution of the data compared to other soundings. The Dodge City, KS site soundings had 6-second resolution compared to the 1-2 second resolution of the other soundings.

3.2. Model Datasets

In this study, no model runs were conducted. Observational sounding data were interpolated to the vertical levels of selected models. Vertical pressure levels were retrieved from model documentation from various reanalysis models and an operational model. The observed soundings were then interpolated to the model levels. This method purposely differs from ingesting the data through data assimilation (DA; reanalysis models) and/or running the model forecast (operational models) and then pulling a proximity sounding. This method allows us to study the impact of coarsened resolution only, without additional changes to the vertical profile from DA or parameterizations (e.g., boundary layer

16

parameterization). Atmospheric models, especially reanalysis models, are considered to have more coarse resolution compared to models used to forecast convection.

The selected reanalysis and operational models are summarized below. A more concise list of the models used and their corresponding levels is provided in Table 2. Modern-Era Retrospective analysis for Research and Applications, Version 2 (MERRA-2; Gelaro et al. 2017) is a NASA global reanalysis model that assimilates satellite observations of aerosols and the land-surface. The reanalysis model consists of 72 levels on the native vertical grid (Fig. 4). displays a plot of the pressure levels for MERRA-2 from 0-10 km converted to height. ERA-Interim is a global reanalysis product produced by ECMWF (Dee et al. 2011). ERA-Interim has 60 vertical levels in the native vertical grid (Fig. 5). ERA5 is the latest reanalysis model from ECMWF. ERA5 has a native vertical resolution of 137 hybrid sigma/pressure levels from surface to 80 km (Hersbach et al. 2020). As illustrated in Fig. 6, ERA-5 notably has higher vertical resolution compared to the previous reanalysis models mentioned, especially in the lower levels.

Models also consist of a set of standard pressure levels which can be utilized when obtaining data such as reanalysis data (e.g. ERA-5 derived, CFSR). Although the aforementioned ERA-5 consists of the highest vertical resolution compared to other reanalysis models, it provides the option to download data using the derived levels. There was a visible difference between the number of vertical levels of ERA-5 native and ERA-5 derived grid as shown in Fig. 6 and Fig. 7. North American Regional Reanalysis (NARR; Mesinger et al. 2006), is an NCEP model consisting of 29 pressure levels (NOAA/OAR/ESRL PSL, NCEP North American Regional Reanalysis: NARR). With fewer vertical levels, especially in the boundary layer, this results in less data which may

17

affect the accuracy of thermodynamic or even kinematic profiles (Fig. 8). In Gensini et al. 2014, the limited vertical resolution of NARR was acknowledged and NARR reanalysis data was compared to observed soundings to evaluate its limitations. Results displayed some biases amongst thermodynamic variables.

In addition to reanalysis model sets, vertical levels from an operational model was used in this study. The Global Forecast System (GFS) is an operational model produced by National Center for Environmental Prediction (NCEP). The current version, GFSv15, has 64 vertical levels (Fig. 9) and the upcoming implementation (Winter 2021), GFSv16, has 127 levels (Fig. 10).

Note that although the models do not have a true scalar point (temperature, pressure, etc.) at the surface, it is standard practice to provide output that includes surface and near surface values by interpolating between the lowest model level and the parameterized surface properties. All the model output sets list above reflect this practice except for MERRA-2, which reports its lowest output at 985 hPa. To match the other datasets, a level at 1013.25 hPa was added to MERRA-2 for the interpolated step.

Another important aspect related to vertical resolution is the distance between vertical height/pressure levels. Larger distances between levels in a layer (Δz) results in less data points. Thinning of data points can decrease the ability to represent important gradients in the atmospheric profile which may affect reliability of calculated convective parameters. Fig. 11 displays the change in height from 0-5 km for each of the model utilized in this study. NARR and the set of standard pressure levels show a similar Δz in the 0-2 km layer of the atmosphere. Both sets show a larger Δz compared to the other models. The manual addition of the surface level for MERRA-2 created a jump in Δz, but overall the

lower layer shows smaller Δz compared to the coarser models mentioned. ERA-Interim increases in Δz rather exponentially and becomes larger than MERRA-2 within the first 1 km. ERA-5 and GFSv16 show similar profiles with notably smaller Δz in the 0-5 km layer resulting from their higher vertical resolution.

3.3. Calculations of Convective Parameters

In order to assess the ability for the selected model sets to represent the convective environment, a set of convective parameters were calculated for both the observed sounding data (control) and sounding data interpolated to the vertical levels of each model. It is important to note that although a sounding may display parameter values in an ideal range, convection is not guaranteed to initiate.

Not every sounding in the selected campaign datasets are necessarily convective. In order to ensure a dataset contains soundings that are more representative of a convective environment, a CAPE threshold was set. The limitations of each parcel type were weighed when determining what variation of CAPE to use. Craven et al. (2002), concluded that the mixed-layer parcel provided a better representation of the parcel profile compared to the surface-based parcel when calculating LCL heights. This result was inferred to factor into other calculations as well such as CAPE. In some instances, the surface fields may not be representative of the thermodynamic profile in the boundary layer (e.g., high surface dewpoints, surface inversions etc.) which make SBCAPE less reliable. MUCAPE lifts the most unstable parcel within a given depth has shown to provide a better representation of elevated convection (Rochette et al. 1999). In some instances, MUCAPE and SBCAPE can be equivalent (when the most unstable profile starts at the surface) resulting in the same potential issues discussed about the surface parcel. Using a mixed-layer parcel can help

alleviate this error by providing a mean profile of temperature and moisture profiles in the lowest 100 mb by assuming a mixed-layer. The mixed-layer parcel approximation presents its own set of limitations with the assumption of a constant well-mixed layer in the 100 mb layer (Markowski and Richardson 2010, Chap. 7). In the end, the mixed-layer parcel type (MLCAPE) was selected to calculate CAPE for the threshold. The MLCAPE threshold for midlatitude campaigns was set at 1000 J/kg with the intent of having soundings representative of stronger convection. In Craven and Brooks (2004), box and whisker plots for the MLCAPE "severe" category events displayed the 50th percentile to be slightly above 500 J/kg CAPE making 1,000 J/kg a realistic threshold for severe convection. The threshold was slightly lowered to 500 J/kg for tropical regime campaigns to account for the generally lower instability compared to midlatitude regimes. Convective parameters were calculated from the soundings that have MLCAPE above their respective thresholds.

Thermodynamic variables were calculated using the Sounding and Hodograph Analysis and Research Program in Python (SHARPpy) software package (Blumberg et al. 2017). Multiple lifted parcel profile types will be used including 100 mb mixed/mean-layer (ML), surface-based (SB), and most unstable parcel (MU). The ML parcel averages temperature and dewpoint in the first 100 mb layer while SB parcel only utilizes surface observations. MU parcel type provides a trajectory of most unstable lifted parcel in the lowest 400 mb layer which is ideal for convective environments characterized by a stable layer near the surface. The SHARPpy package also uses virtual temperature correction (Doswell and Rasmussen 1994) when calculating the thermodynamic parameters. The mentioned parcel types were utilized to calculation variations of CAPE, CIN, and LNB (Table 3).

Some limitations were considered for LNB calculations, especially so for midlatitude regime campaigns. There were documented cases in which the lifted parcel remained positively buoyant at the maximum height of the sounding; therefore, the LNB could not be reached/calculated. Two types of cases were suspected to cause this; 1. The sounding was cut off or the balloon-sonde popped before the LNB was reached or 2. The LNB was higher than the artificial cutoff at 15 km (midlatitude soundings only). Further investigation calculated an average of approximately 20% of midlatitude regime soundings to contain this issue and approximately 3% of tropical regime cases. The artificial cutoff at 15 km for midlatitude regime soundings was surmised to be a factor for their higher percentage compared to tropical soundings which had no cutoff. Figure 12 displays a height vs temperature sounding from VORTEX2 where the MU and SB (not shown) parcel LNB were not calculated; however, ML parcel LNB was calculated. The ML parcel profile visibly reaches its LNB towards the top of the sounding, but the MU parcel profile still remains positively buoyant at the max height. The max height for this sounding was 15 km hinting that the sounding may have been impacted by the artificial cut-off. Another sounding picked from the VORTEX2 dataset (Fig. 13), showed both ML and MU parcel profiles remaining positively buoyant at the max height (~10 km) of the sounding. Although tropical regime soundings had a smaller percentage of soundings with this issue, some cases were noted. A sounding was selected from a tropical regime dataset, DYNAMO (Fig. 14), where all parcel variations of LNB were not calculated. At a max height of approximately 10 km, the plotted profiles show that the LNB was not reach at that height where the sounding ended. Given that the highest average percentage of occurrence was 20%, the sample size should be sufficient enough to display results.

The Metpy package (May et al. 2020) was utilized to calculated kinematic variables, 0-3 km bulk shear and 0-6 km bulk shear. To consistently keep calculations AGL, data was adjusted based on the lowest height observation for each sounding. No consistent errors were noted for the kinematic calculations with the exception of some single case outliers of non-realistic bulk shear. Those associated soundings were removed from the dataset.

The capping inversion strength was calculated by determining the maximum positive lapse rate (Coniglio 2013) in the surface-5 km layer. Prior to calculation of the max lapse rate, data points were interpolated to 100-m/Δz to prevent any "one-point" outliers in the temperature profile resulting from the high-resolution data. Previously mentioned in section 3.1.2, there were some documented cases of unrealistic capping inversion strength values as a result of erroneous surface temperature measurements which were removed from the GOAMAZON dataset. Given the simplistic nature of calculating the cap strength in this study, there were cases in which surface inversions were captured. Although surface inversions are important features that can affect the overall instability of a sounding, this study focused on elevated capping inversions. A secondary check was implemented to identify potential soundings that meet the criteria of a surface inversion by evaluating if temperature increased with height within the first section of data points of the sounding. A small percentage (< 20%) of soundings met the criteria for a surface inversion. This subset of soundings did not have cap strength calculated.

3.4. Interpolation of observational datasets

After the calculation of the convective parameters, the observed sounding data were interpolated to the pressure levels provided from the selected models (Table 2). For the initial step in the interpolation process, the set of pressure levels of the models were

adjusted to each sounding based on the first pressure value in the observed profile. Temperature, dewpoint, height, and wind variables were then interpolated based on the pressure values. Convective parameters are re-calculated on the newly interpolated datasets.

Table 1. List of field projects that sounding data was obtained from, categorized by latitude. To the right of each field project is the corresponding number of soundings used for each campaign after the application of the threshold (convective soundings).

Category 1 - Midlatitude Regime ($\phi > 30°$)	Number of Soundings (After threshold)
Plain Elevated Convection at Night (PECAN)	807
Deep Convective Clouds and Chemistry Project (DC3)	760
Verification of the Origins of Rotation in Tornadoes Experiment 2 (VORTEX2)	927
Category 2 - Tropical Regime ($\phi < 30°$)	**Number of Soundings (After threshold)**
Tropical Rainfall Measuring Mission – Large Scale Biosphere-Atmospheric Experiment in Amazonia (TRMM-LBA)	374
Dynamics of the Madden-Julien Oscillation (DYNAMO)	2268
Observations and Modeling of the Green Ocean Amazon (GOAMAZON)	2125

Table 2. List of models and their number of vertical levels.

Model	Number of Vertical Levels
ERA5	137
ERA-Interim	60
MERRA-2	72
Standard Press. Levels (e.g., ERA5 derived, CFSR)	37
NARR	29
GFSv15	64
GFSv16	127

Table 3. List of sounding-derived parameters calculated in this study

Convective Parameter	Abbreviation
Thermodynamic	
Mixed-layer convective available potential energy	MLCAPE
Surface-based convective available potential energy	SBCAPE
Most unstable convective available potential energy	MUCAPE
Mixed-layer convective inhibition	MLCIN
Surface-based convective inhibition	SBCIN
Most unstable convective inhibition	MUCIN
Kinematic	
Bulk-shear (0-6 km/0-3 km AGL)	0-3/0-6 km Bulk-shear
Other Calcuated Variables	
Capping inversion strength	CIS
Level of neutral bouyancy	ML, MU, SB
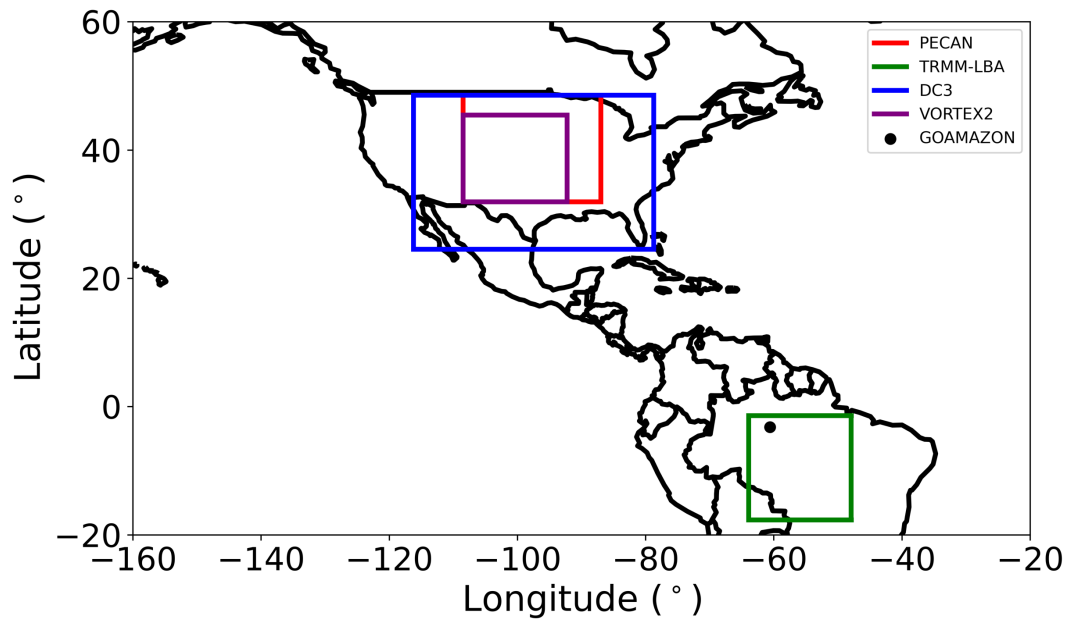
Figure 1. Western hemisphere research campaigns used in this study. Polygons show the general area from which soundings were launched. PECAN (red), DC3 (blue), VORTEX2 (purple) and TRMM-LBA (green). GOAMAZON is noted by the black dot as soundings were launched from a consistent location.
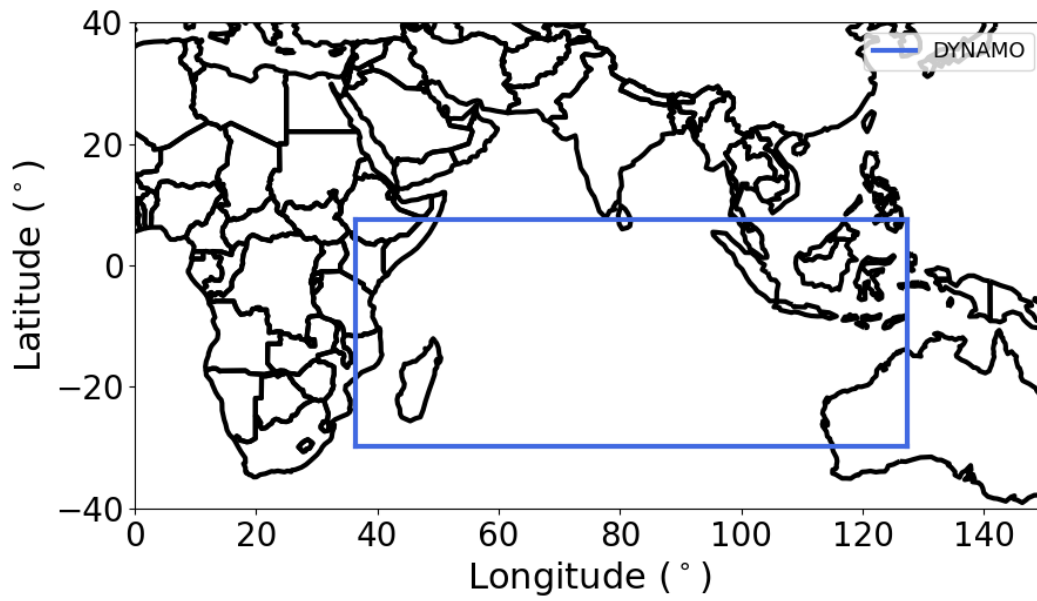
Figure 2. The plotted polygon shows the region from which soundings were launched for the one

Eastern Hemisphere campaign used in this study, DYNAMO (blue).
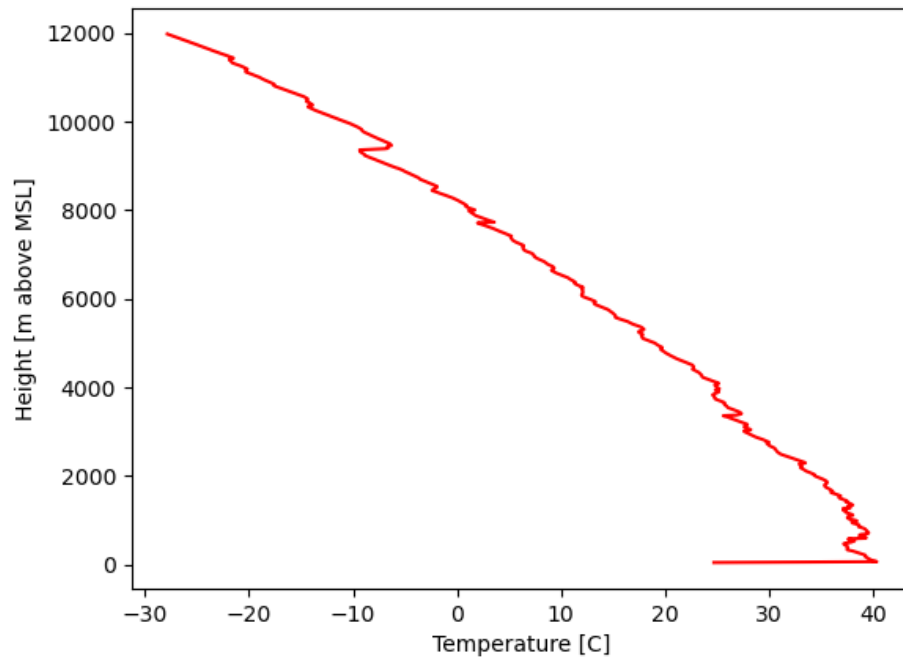
Figure 3. Example of a data quality issue with the surface temperature for GOAMAZON.

Temperature [°C].
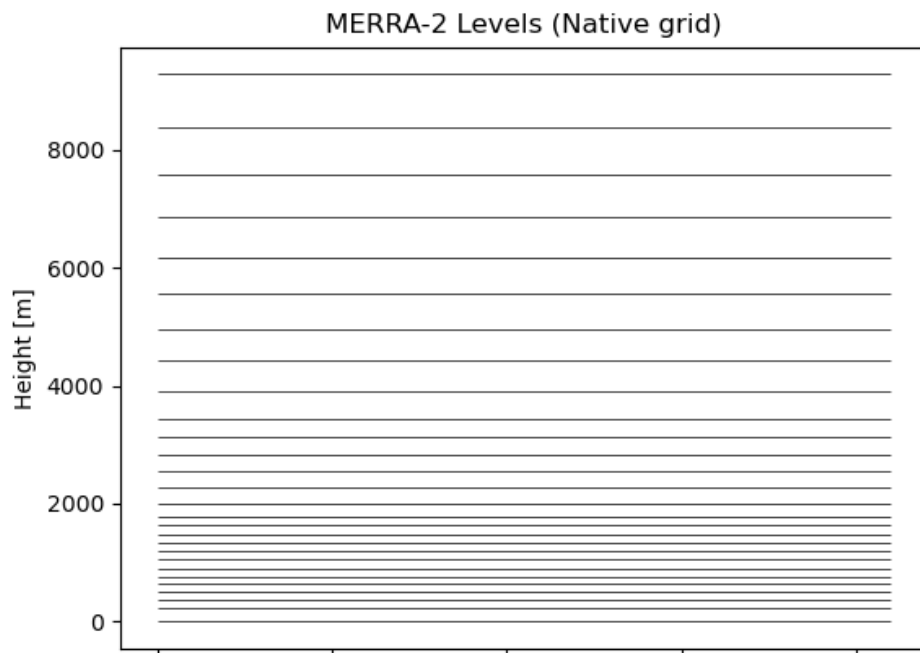
Figure 4. MERRA-2 native vertical levels from 0-10 km calculated from pressure.
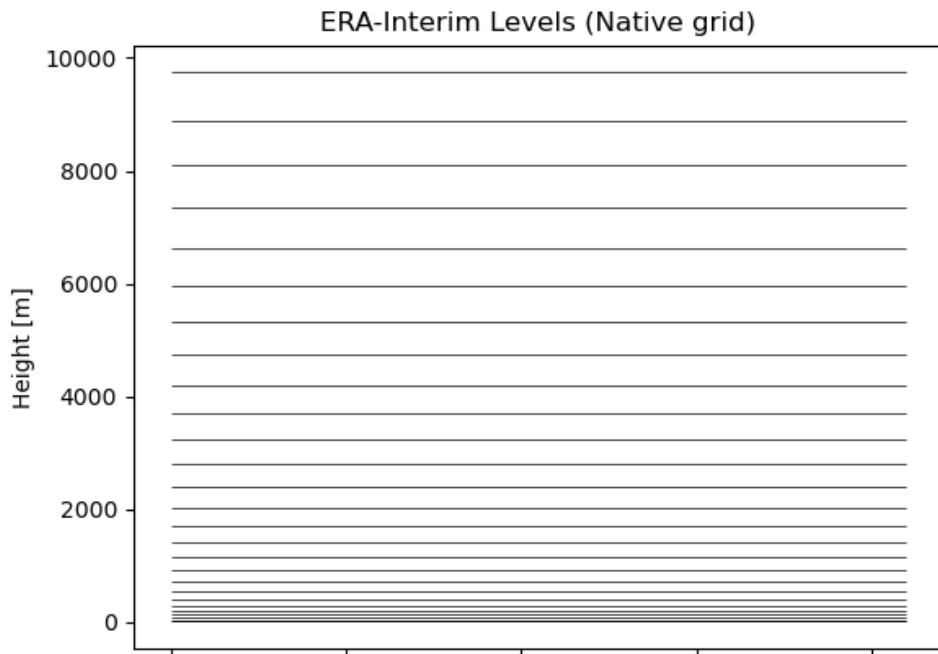
Figure 5. ERA-Interim native vertical levels from 0-10 km calculated from pressure.
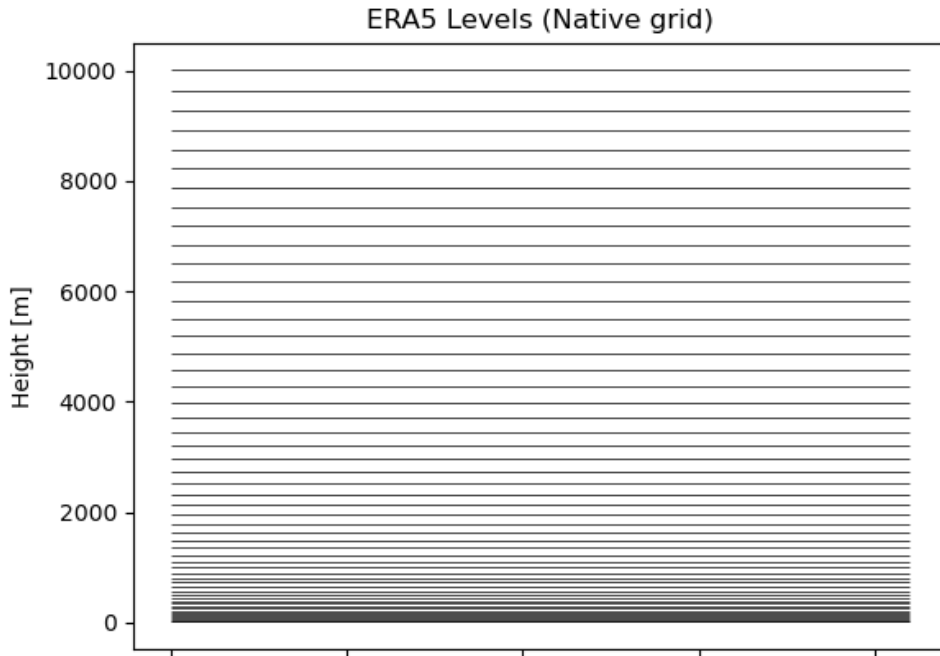
Figure 6. ERA5 native vertical levels from 0-10 km calculated from pressure.
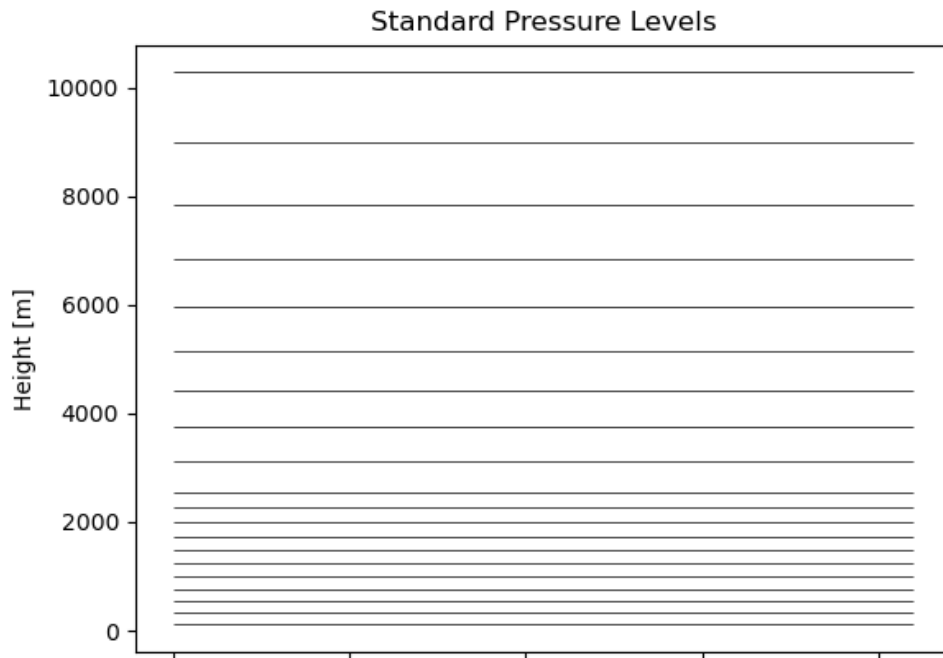
Figure 7. Vertical levels associated with standard pressure levels from 0-10 km calculated from

pressure (e.g. CFSR, ERA-5 derived levels).
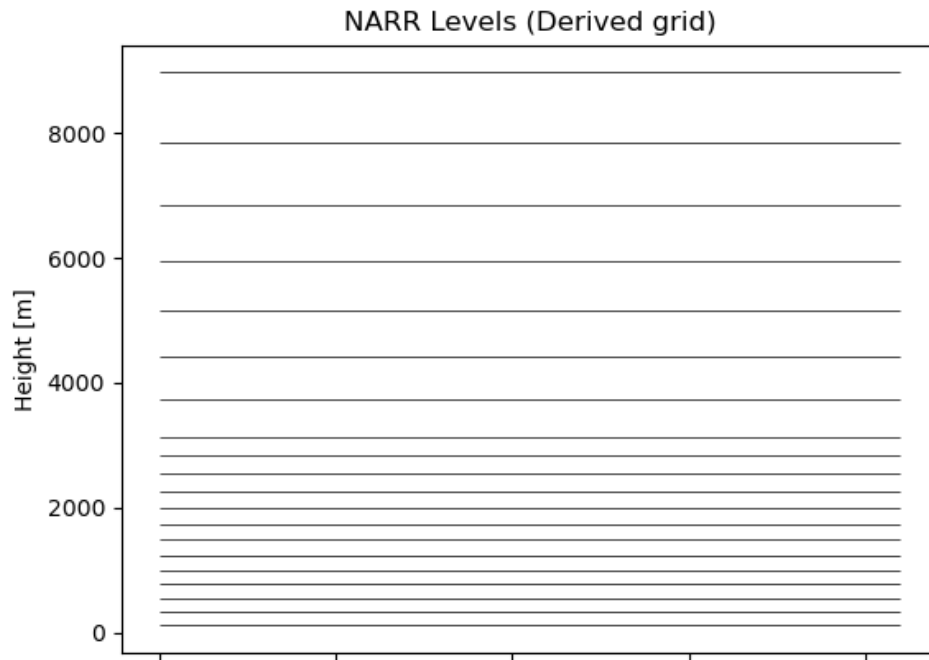
Figure 8. NARR vertical levels from 0-10 km calculated from pressure.
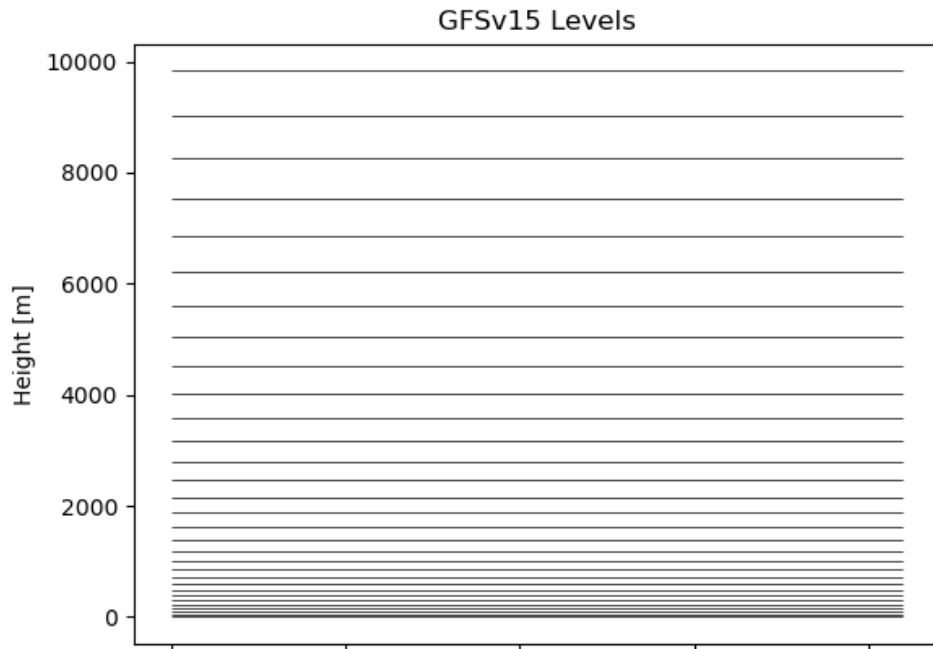
Figure 9. GFSv15 native vertical levels from 0-10 km calculated from pressure.
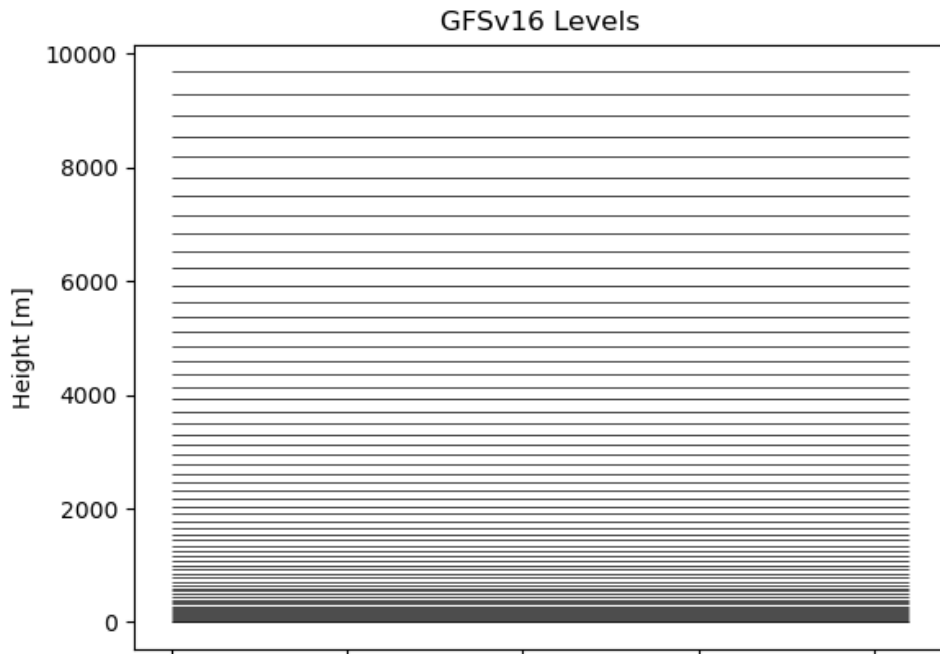
Figure 10. GFSv16 native vertical levels from 0-10 km calculated from pressure.
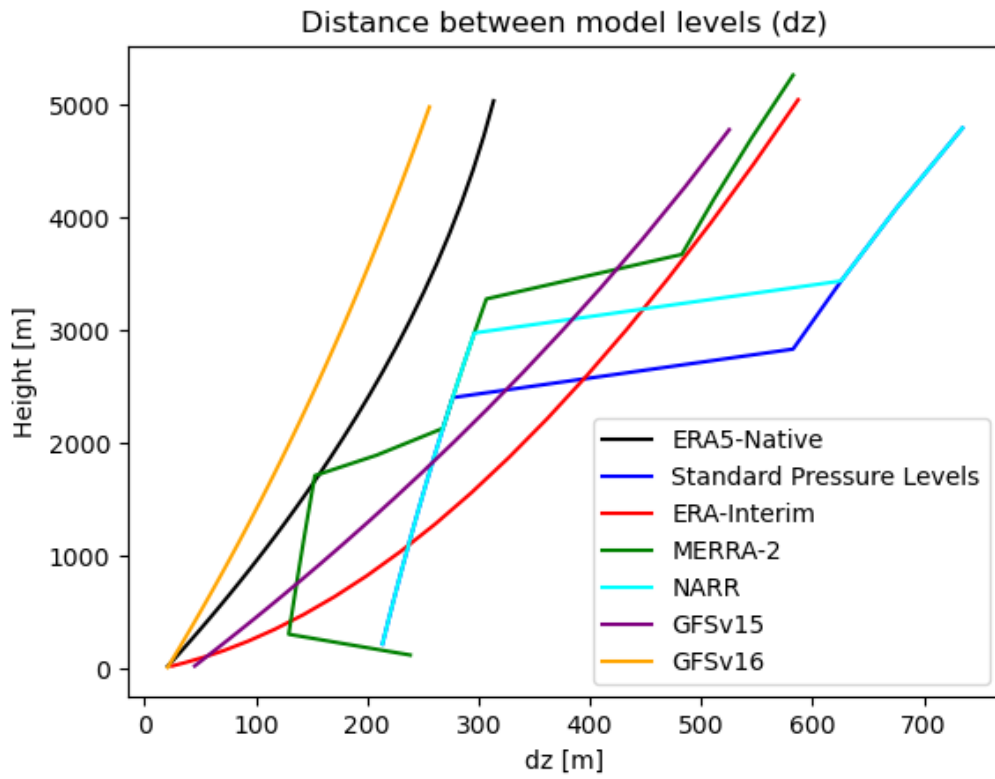
Figure 11. Calculated Δz for each corresponding set of model levels from 0-5 km.
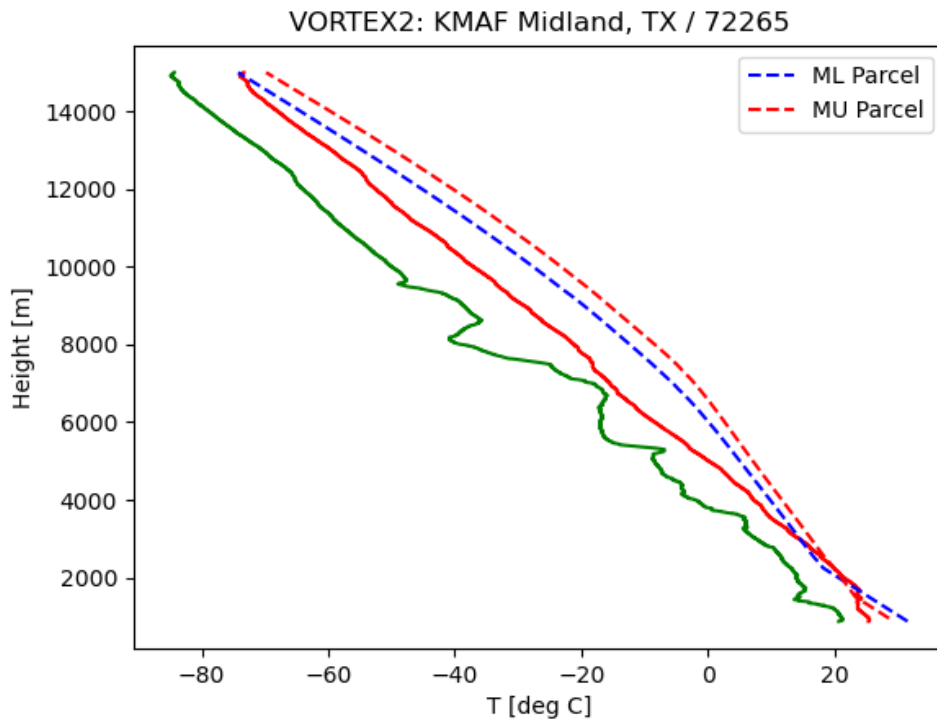
Figure 12. Plot of temperature (red) and dewpoint (green) profiles (x) with increasing height (y)

for a VORTEX2 sounding. ML (blue) and MU (red) lifted parcel profiles also plotted.
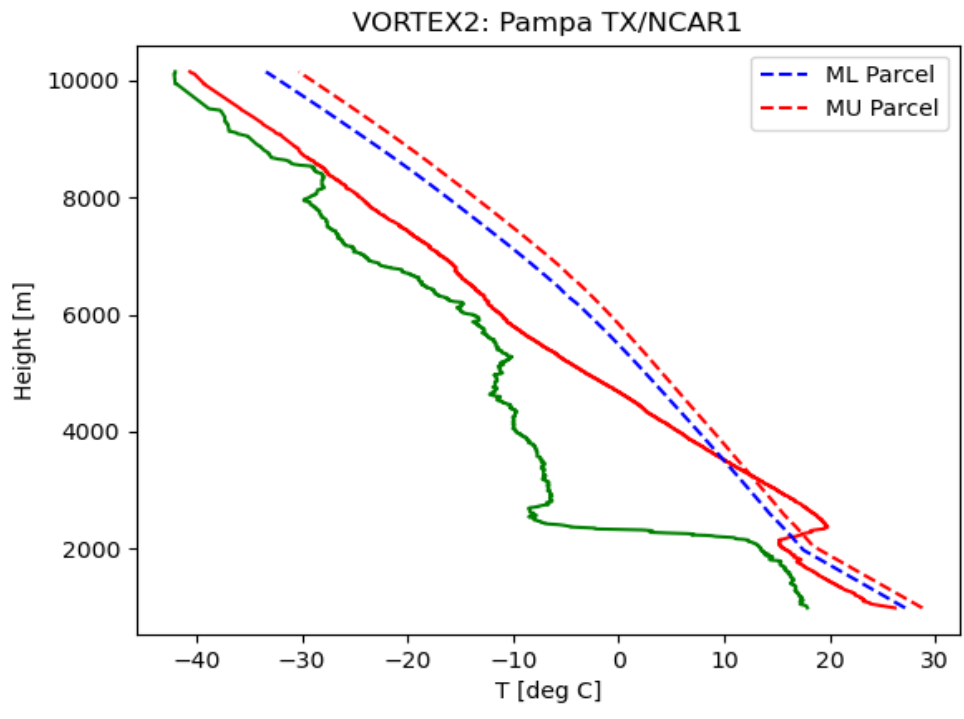
Figure 13. Same as in Fig. 12, except a different sounding from the VORTEX2 campaign dataset.
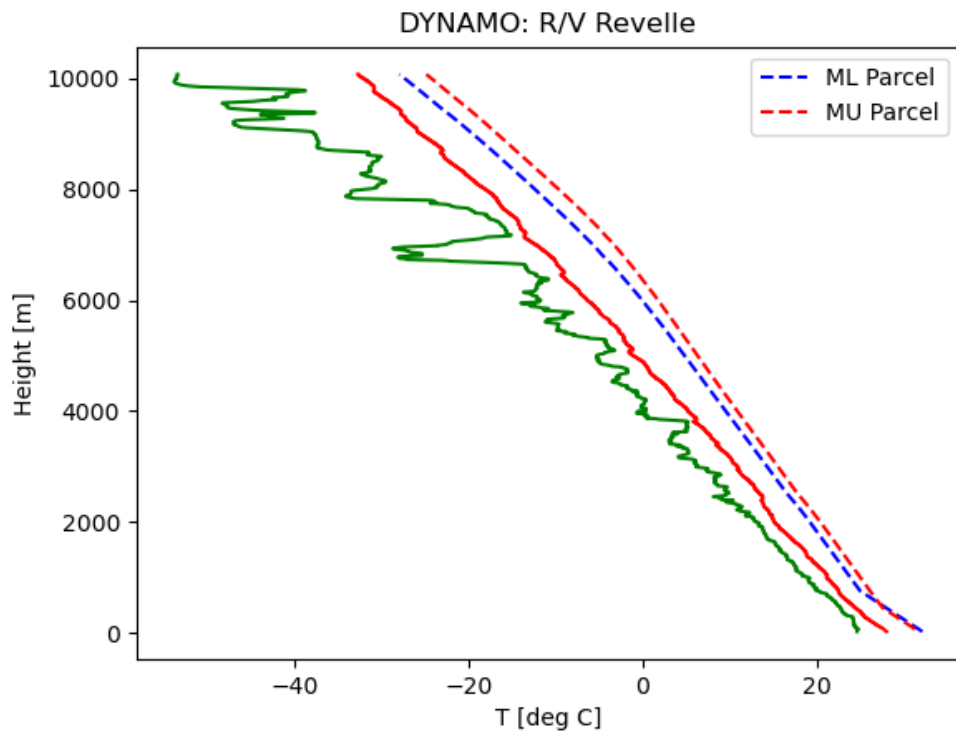
Figure 14. Same as in Fig. 12 & 13, except sounding is obtained from DYNAMO dataset.

CHAPTER 4

RESULTS

The results are broken down into multiple sections organized by parameter (Chapter 3, Table 3). All sections include scatter and histogram plots of both the total data set as well as composited subsets (e.g., composite by region). Scatterplots provide a one-to-one comparison between the observed parameter calculation for a given sounding and the corresponding calculation for the various reanalysis sets (Chapter 3, Table 2). Histograms compare the overall distributions of observed values to each of the interpolated reanalysis sets (Chapter 3, Table 2). Pearson correlation coefficient is calculated for select parameters and discussed in the *Summary and Impacts* section of this chapter.

4.1. MLCAPE

Across all interpolated reanalysis sets, Figure 15 displays a consistent trend of increasing underestimation towards the moderate to high MLCAPE cases. Both overprediction and underprediction are visible throughout the calculated soundings, with overprediction being more evident in the 1,000-3,000 J/kg range. However, a general trend of an increase in deviation from the observed is exhibited as cases of underprediction begin to be more dominant above 2,500 J/kg MLCAPE.

Figure 16 categorizes the scatterplot by regime (tropical and midaltitude). The midlatitude regime soundings show a wider range in MLCAPE values compared to those from tropical regimes. Despite the difference in range, both regime types generally display the same trend with an increase in underprediction of MLCAPE towards the upper portion of their ranges. A smaller detail evident is the slightly larger deviations shown by midlatitude regime cases shown when the two regimes overlap (1000-5000 J/kg).

41

Distributions display an increase in the number of MLCAPE values in the 1500-2500 J/kg bins across all interpolated sets when compared to the observed (Fig. 17, Fig. 18). Some reanalysis sets visibly performed better than others denoted by smaller deviations from the observed bin distribution (blue). Despite having fewer vertical levels than ERA5, ERA-Interim, GFS, and MERRA-2 performed slightly better in the 1500-2500 J/kg bins. Most interpolated sets also show a decrease in soundings in the 500-1000 J/kg bin. It is important to note this bin is likely more representative of the tropical regime campaigns since the MLCAPE threshold is 500 J/kg compared to a threshold of 1000 J/kg for midlatitude. In the bins above 3000 J/kg, a decrease in the number of soundings is evident. This trend is shown across all interpolated model sets with and is most visible in the lower vertical resolution sets (e.g., Standard pressure levels, MERRA-2, NARR).

4.2. MUCAPE

Similar to MLCAPE, MUCAPE displays an overall consistent trend with increasing underestimation in CAPE values above 1500 J/kg (Fig. 19). Note that scatter plots were cut off at 7000 J/kg for both MUCAPE and SBCAPE to display soundings with more realistic CAPE values. A small percentage of soundings (approximately < 2%) had CAPE above 7000 J/kg, so the overall sample size wasn't impacted. There are visibly less cases of overestimation of MUCAPE across all model interpolated sets compared to MLCAPE. Interestingly, some reanalysis model sets can be picked out as "performing" worse than others in Figure 16. NARR (cyan) and MERRA-2 (green), and scattered standard pressure levels (magenta) visibly show larger deviations from the observed in the form of

42

underestimation especially in the 2000-5000 J/kg observed MUCAPE range. GFS version 15 and 16 visibly perform well denoted by the stronger correlation to the observed values.

The trend of increasing underestimation of MUCAPE is consistent shown across both tropical and midlatitude regimes (Fig. 20). In regards to the more detailed differences, tropical regime soundings show some cases of larger underestimations in the 2000-4000 J/kg observed case range. Midlatitude regime soundings showed slightly more cases of over overestimation in that same range. For the highest MUCAPE values (over 6000 J/kg), midlatitude cases underestimated values more than the tropical cases.

The MUCAPE distributions (Fig. 21, Fig. 22) show a visible increase in soundings in the 500-3000 J/kg bins across all interpolated model sets compared to the observed distribution. This result mirrors the result for MLCAPE in the 1000-3000 J/kg range, but differs from MLCAPE particularly below 10000 J/kg where MLCAPE showed marked decreases in number of sounding for that range and MUCAPE shows consistent increases. Above 3000 J/kg, distributions exhibit a decrease in the number soundings for the model sets compared to the observed (similar to MLCAPE).

4.3. SBCAPE

Overall, SBCAPE presents a similar bias to MLCAPE and MUCAPE when comparing interpolated set calculations to the observed. Underestimations and overestimations of the interpolated set occur in the 0-3000 J/kg observed cases. However, towards higher CAPE cases (above 3000 J/kg) underestimation cases become more dominant. Calculated SBCAPE shows a similar trend across both regime types (Fig. 24) with larger underestimations in the midlatitude sounding cases.

The distributions in the two histograms for SBCAPE exhibit similar trends shown in both MLCAPE and MUCAPE distributions (Fig. 25, Fig. 26). The 1000-3000 J/kg range presents an increase in the number of soundings compared to the observed across all interpolated sets. Similarly shown in MLCAPE distributions (Fig. 17, Fig. 18), there is a decrease in number of soundings in the low CAPE range (0-1000 J/kg bins). Analogous to the other CAPE variations, there is a decrease in the number of soundings in the higher CAPE bins (above 3000 J/kg) for the interpolated sets. GFSv15 and v16 showed distributions slightly closer to the observed indicating better performance in the 3500-4500 J/kg bins (Fig. 26).

4.3. MLCIN

For all variations of CIN discussed in the next few sections, it is important to note that CIN values will be referred to by magnitude (e.g., high CIN > |-200| J/kg). Overall, the interpolated sets indicated little variation of MLCIN from the observed (Fig. 27). Cases of overestimation and underestimation by the interpolated sets are visible with a slight bias toward overestimation cases in the -600 to -200 J/kg range. ERA-Interim (red) and ERA5 (black) frequently overestimate MLCIN. MERRA-2 (green) underestimated MLCIN in some cases, although not clear that the underestimation is significant. When looking at the data categorized by regime type (Fig. 28), a difference in range of MLCIN values is evident between tropical and midlatitude regimes. Tropical regime sounding cases display a shorter range in MLCIN values compared to midlatitude soundings. Both regimes exhibit cases of underestimation and overestimation by interpolated sets; however, midlatitude cases are responsible for majority of the larger overestimation cases. Distributions of calculated MLCIN concur with the scatterplot (Fig. 27) that the interpolated sets do a relatively good

job calculating MLCIN as distributions are close to the observed (Fig. 29, Fig. 30). As the distribution plots do not add significant interpretive value, they will not be shown below for MUCIN or SBCIN.

4.4. MUCIN

Shown in Fig. 31, no dominant bias is evident for calculated MUCIN. A mix of both underestimation and overestimation cases persists across the full range of MUCIN cases. Overall, the interpolated set calculations appear close to the 1-1 line indicating close values to the observed. Outliers cases are present as well in both the overestimation and underestimation cases across the range of MUCIN. NARR (cyan) shows the greatest spread with no consistent bias. As in MLCIN, ERA-Interim seems to consistently overestimate the magnitude of MUCIN. Also similar to MLCIN, Fig. 32 shows midlatitude regime soundings to have a larger range of CIN than the tropical regime soundings. Both regimes display both underestimation and overestimation cases; however, the midlatitude regime datasets were responsible for the "larger" deviation from observed cases.

4.5. SBCIN

Compared to the other parcel variations of CIN, calculated SBCIN by the interpolated sets appear better correlated to the observed (Fig. 33; note changed axes); however, the extent is not clear due to differing plot axes. Interpolated sets present marginal overestimation and underestimation with a shift to primarily underestimating magnitude at SBCIN > |-300| J/kg. A few outliers are seen when the observed SBCIN is zero and corresponding interpolated sets are overestimating CIN. Both midlatitude and tropical regime soundings exhibit this trend of stronger correlation to the observed with midlatitude

regime cases displaying a larger range in SBCIN values compared to tropical regimes (Fig. 34).

4.6. 0-3 km and 0-6 km Bulk Shear

Across all interpolated model datasets, calculated 0-6 km bulk shear cases are close to the 1-1 line indicating a strong correlation between the interpolated and observed (Fig. 35). Small deviations from the observed are visible for interpolated set calculations indicating minor cases of overestimation and underestimation. Both midlatitude and tropical regimes exhibit the same trend with midlatitude regime calculations display a larger range in values of shear compared to tropical regimes (Fig. 36). Distributions (Fig. 37, Fig. 38) show little to no variation between the observed distributions and interpolated model set distributions indicating calculations close to the observed. The results for 0-3 km bulk shear were identical, so are not included here.

4.7. Capping Inversion Strength

Overall, capping inversion strength calculations of the interpolated model sets appear to have a weaker correlation to the observed as shown in Fig. 39. Majority of the interpolated set calculations are displayed below the 1-1 line indicating cases in which the capping inversion was underestimated. A general trend of increasing deviation of the underestimation cases is evident with increasing capping inversion strength (>.02 °C/m). It is visible in Fig. 39 that certain interpolated sets yielded values closer to the observed than others. Reanalysis/model sets with fewer vertical levels (e.g., NARR, Standard Pressure Levels) most consistently underestimate the inversion strength. This shift towards lower cap inversion strength can also be seen in the distribution plots (Figs. 40 and 41), with a shift to weak caps for all models. The largest shift is shown for NARR and Standard

Pressure Levels and much better representation of the cap strength distribution is seen for the highest resolution models, GFSv16 and ERA5. Interestingly, MERRA-2 and ERA-Interim performed similarly despite their considerable difference in vertical levels. Distributions (Fig. 40, Fig. 41) show the lack of bins and values calculated by the interpolated model sets towards the stronger cap cases (>.02°C/m). Interpolated sets such as NARR and standard pressure levels are examples of sets that visibly underestimated capping inversion strength while higher vertical resolution models, ERA5 and GFSv16, had distributions closer to the observed indicating more accurate calculations.

When categorized by regime, Fig. 42 shows that both midlatitude and tropical regimes display the same trend of increasing underestimation with increasing cap strength. The only differentiating characteristic between the two regimes is that midlatitude regimes unsurprisingly had a larger range in cap inversion strength cases.

4.8. MLNB

Fig. 43 displays a relatively close correlation between the observed and calculated values with cases of both overestimation and underestimation. LNB calculations below 8000 m were not included in the scatterplots as this study aims to focus on LNB values for deep convection. This will be consistent for MULNB and SBLNB analysis as well. Previously mentioned in Chapter 3, a small percentage of soundings were cut off before they reached their LNB with more instances associated with the 15 km cutoff for midlatitude soundings. Figure 44 shows a scatterplot classifying data by regime type. Observations that can be made about the range in values of LNB are limited due to the aforementioned limitations. However, it would be typical for tropical regime LNBs to be higher than midlatitude based on regime alone. In addition to this, the midlatitude regime

47

cases for both ML and MU parcel variations had smaller values of LNB in the lower half of their range. Figure 45, displays MLLNB solely from the observed datasets separated by regime. Distributions show the peak in the number of midlatitude soundings to be considerably lower than tropical regime soundings. Although both distributions overlap, there is a larger density of midlatitude soundings towards "lower" MLLNB values. Returning to Fig. 44, both regimes contain cases of overestimation and underestimation; however, tropical regime cases showed slightly larger deviation from the observed for observed MLLNB cases larger than about 11000 m.

Figures 46 and 47 display histograms of the distributions of MLLNB comparing interpolated sets to the observed distributions. Further filtering of the datasets was done due to the percentage of soundings were cut off before they reached their LNB. The following instances were denoted as a "NaN" in the dataset. Their presence was not consistent across all parcel variations of LNB which impacted the reliability of the observed and interpolated distributions when being compared. To combat this, if a NaN was denoted for either an observed or interpolated value being plotted, a NaN was inserted for both values. The same methods are applied to subsequent LNB results (MULNB, SBLNB).

A decreasing number of soundings is consistently shown across most model/reanalysis sets compared to the observed in the 10000-13500 m bins. An increase in the number of soundings is evident in the 14000 m bin across interpolated sets with the exception of MERRA-2 displaying an earlier trend of increasing soundings in the 13500 m bin. All interpolated sets except for MERRA-2 exhibited an increased number of soundings compared to the observed in the 15500 m bin. GFSv15/16 and MERRA-2 notably

performed fairly well denoted by distributions appearing closer to the observed overall for the 15500 m bin.

4.9. MULNB

Similar to MLLNB, Fig. 48 shows the interpolated set calculated MULNB to be well correlated to their corresponding observed values. Differing from MLLNB, there is a larger deviation from the observed 14000-18000 m range with NARR and MERRA-2 representing the underestimation cases. In regards to regime type, Fig. 49 displays a similar to trend to what was shown for MLLNB. Midlatitude regimes demonstrating a similar trend of lower MULNB values than tropical regimes shown in the lower half of the range in values. Tropical regime soundings correspond to the cases of "larger" underestimation. Figure 49 shows the previously mentioned underestimation cases by NARR and MERRA-2 to be tropical regime soundings. MULNB distributions overall displayed small departure of interpolated sets from the observed distributions denoting respectable performance (Fig. 50, Fig. 51). In the 16000 m bin, MERRA-2 and NARR distributions reflect the underestimation cases seen in the scatterplot (Fig. 48).

4.10. SBLNB

Similar to the ML and MU parcel type variations, Fig. 52 shows the interpolated set calculations of SBLNB to be correlated sufficiently to the observed indicating good performance. In the 8000-11000 m observed values, cases of overestimation were most common within the interpolated reanalysis/model sets. A mix of both overestimation and underestimation is visible in cases above 11000 m; however, overall there is a reasonably strong correlation seen for the higher LNB cases.

When categorizing by regime type, Fig. 53 shows a differing trend between tropical and midlatitude datasets compared to the other parcel types. MLLNB and MULNB showed overall lower values of LNB for midlatitude soundings (excluding the upper range due to 15 km cutoff). However, SBLNB shows less of a distinction between midlatitude and tropical regime values. Fig. 54 displays the observed SBLNB values for both regime types and indicates a larger overlap between regimes. However, the peaks in LNB differ in that midlatitude soundings displayed a lower peak in values compared to tropical. This is similar to what was displayed in the observed distributions for MLLNB (Fig. 45). SBLNB distributions of the interpolated sets overall demonstrate to be close to the observed distributions therefore mirroring the trend of sufficiently performing interpolated model sets (Fig. 55, Fig. 56).

4.11. Summary and Impacts

Reanalyses and operational model sets consistently demonstrated an underestimation of CAPE, especially evident in cases above 3,000 J/kg. To quantify the degree of correlation to the observed, Pearson correlation coefficients were calculated for select parameters (Table 4). A strong correlation would indicate the model set calculated values were close to the observed values. Model sets with higher vertical resolution (e.g., ERA5, GFSv16) tended to have the strongest correlations across the different parcel variations of CAPE. Sets with lower vertical resolution (e.g., ERA-Interim, NARR, standard pressure levels) displayed slightly lower correlations compared to models with more vertical levels. Interestingly, SBCAPE showed to be the least sensitive to vertical resolution with majority of model sets displaying correlations of .98. Overall, both correlation coefficients and scatterplots demonstrate the underprediction and slightly lower

50

correlation in CAPE as a result of degrading vertical resolution. Analysis of high CAPE modeled environments may be impacted if lower vertical resolution models are utilized, therefore, it is critical to acknowledge this underestimation bias.

Overall, CIN calculations by the interpolated model sets were quite close to the observed soundings and no clear bias is displayed, especially for MUCIN and MLCIN. This is demonstrated by strong correlation coefficients across all model interpolated sets for CIN calculations (Table 4). LNB calculations by the interpolated model sets demonstrated no consistent bias among the differing parcel types, but overall, interpolated cases were well correlated to the observed. Notably, MULNB displayed cases of underestimation of the LNB by NARR and MERRA-2 interpolated sets linked to tropical regime cases. Accurate calculations of the LNB are important due to its various uses as a proxy for deep convection, composite parameter calculations, and its relation to the LMD.

Both 0-3 and 0-6 km bulk shear were shown to be insensitive to decreasing vertical resolution provided by the visibly strong correlations shown in both the scatterplots (Fig. 35) and calculated correlation coefficients (Table 4).

Accurate representation of a capping inversion by a model can be critical to forecasters when assessing severe convective potential due to its relation to convection initiation, especially for midlatitude regimes. Results demonstrated that decreasing the number of vertical levels can impact the accuracy of the capping inversion magnitude. Underprediction of stronger cap cases was evident in Fig. 39. Calculated correlation coefficients displayed the lowest correlations for cap strength compared to the other parameters (Table 4). Correlation coefficients for lower vertical resolution models such as NARR, ERA-Interim, and standard pressure levels were lower than those for models of

higher vertical resolution such as ERA5 and GFSv16. This may indicate the potential for issues regarding convection strength, location, timing. In regards to using reanalysis model data, lower vertical resolution datasets (e.g., NARR, use of standard pressure levels) pose the potential for larger errors in representing strong capping inversions. Interestingly, despite a lower correlation being shown for cap strength, interpolated sets generally did well when calculating CIN which can be influenced by the occurrence of a capping inversion.
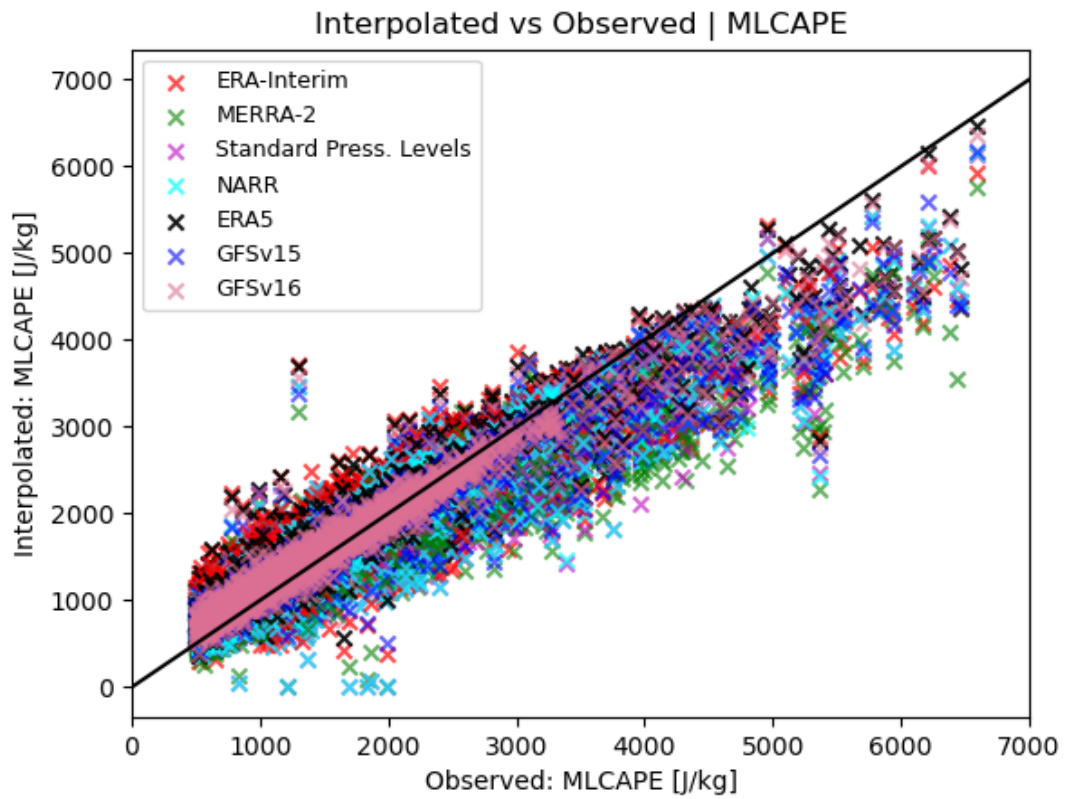
Figure 15. Scatter plot showing relationship between the interpolated (y) and observed (x) datasets for MLCAPE with all campaigns. Legend displays each interpolated model/reanalysis dataset and its corresponding color marker.
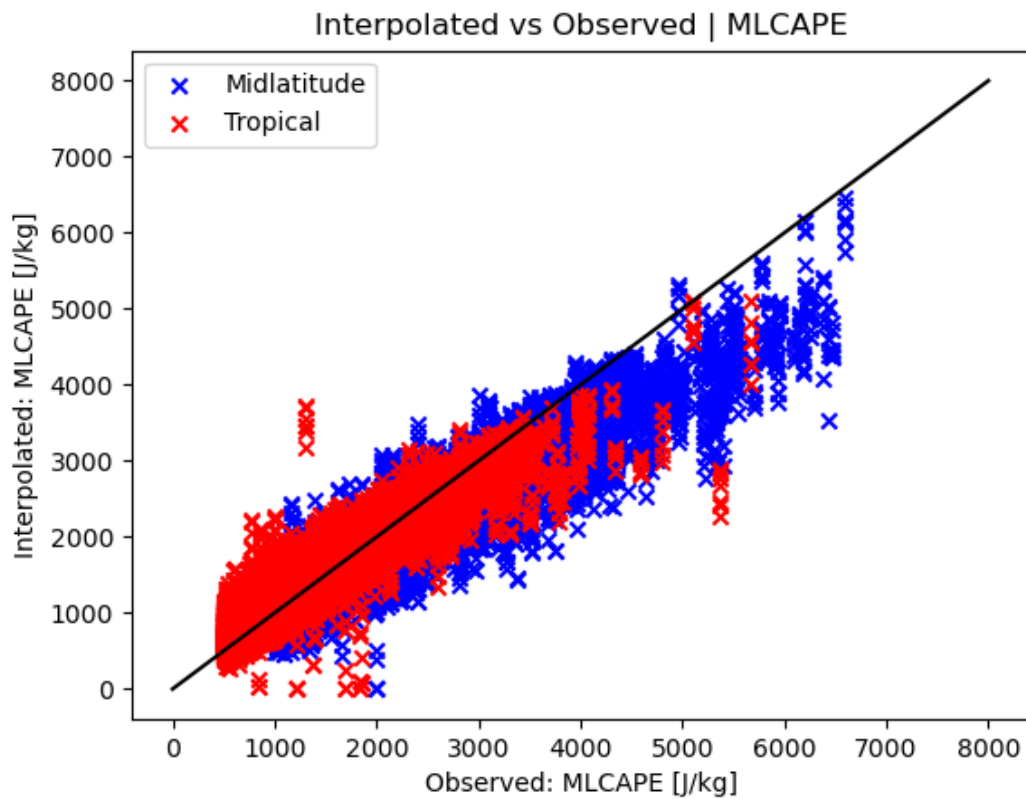
Figure 16. Scatter plot showing relationship between the interpolated (y) and observed (x)

datasets for MLCAPE with all campaigns. Midlatitude campaigns (blue) and tropical campaigns

(red).

Figure 17. Subplots of histograms displaying MLCAPE distributions for all campaigns. Each subplot compares observed (blue) to model/reanalysis interpolated (red) MLCAPE.

Figure 18. Same as in Fig. 17, but displaying operational model interpolated sets.

Figure 19. Scatter plot showing relationship between the interpolated (y) and observed (x) datasets for MUCAPE with all campaigns. Legend displays each interpolated model/reanalysis dataset and its corresponding color marker.

Figure 20. Scatter plot showing relationship between the interpolated (y) and observed (x)

datasets for MUCAPE with all campaigns. Midlatitude campaigns (blue) and tropical campaigns
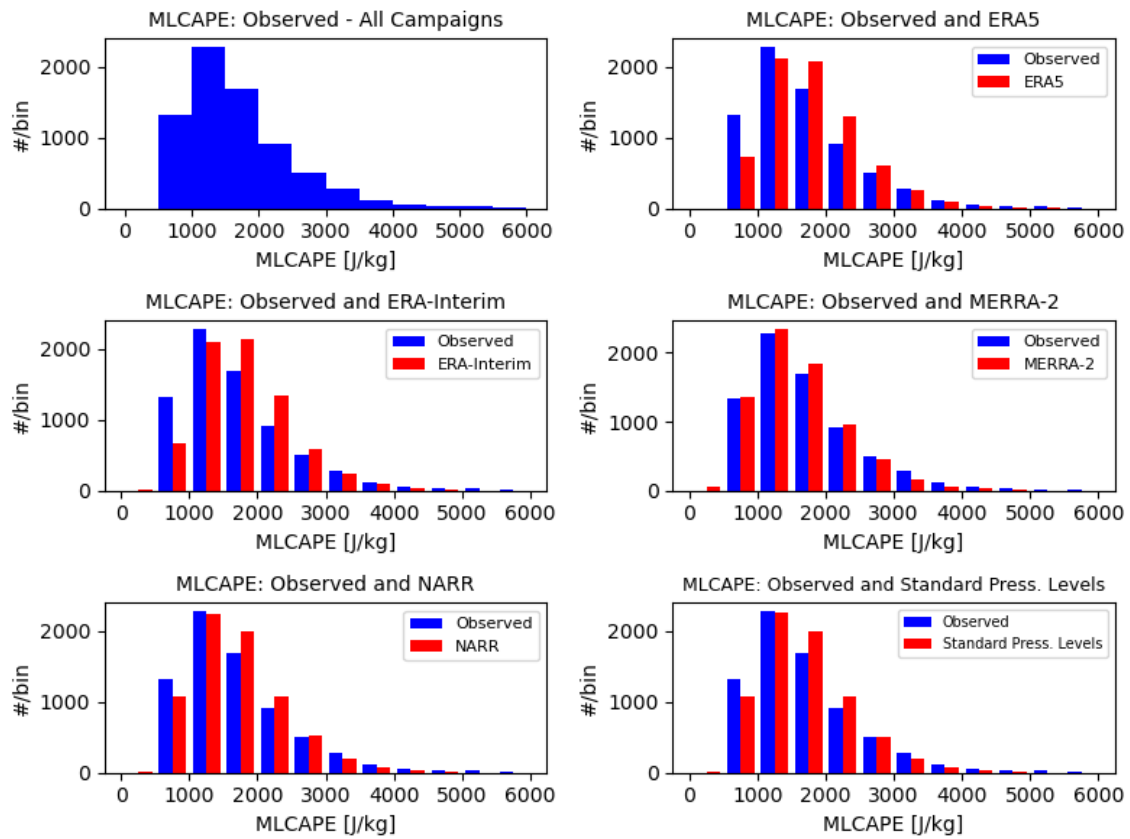
(red).

Figure 21. Subplots of histograms displaying MUCAPE distributions for all campaigns. Each subplot compares observed (blue) to model/reanalysis interpolated (red) MUCAPE.
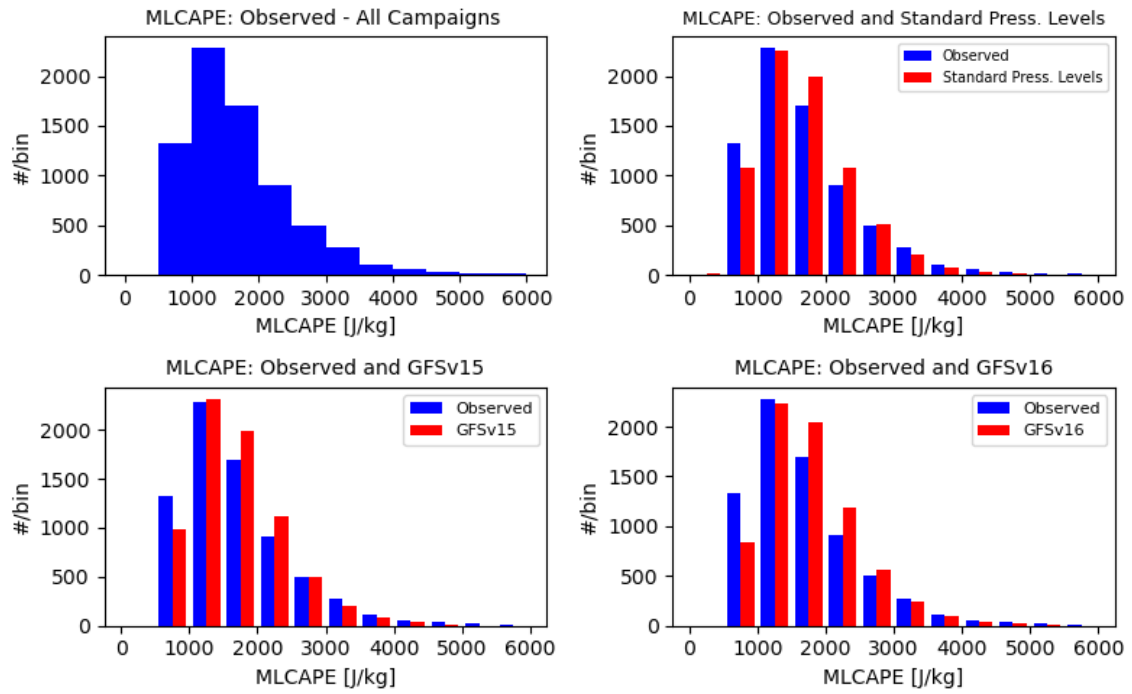
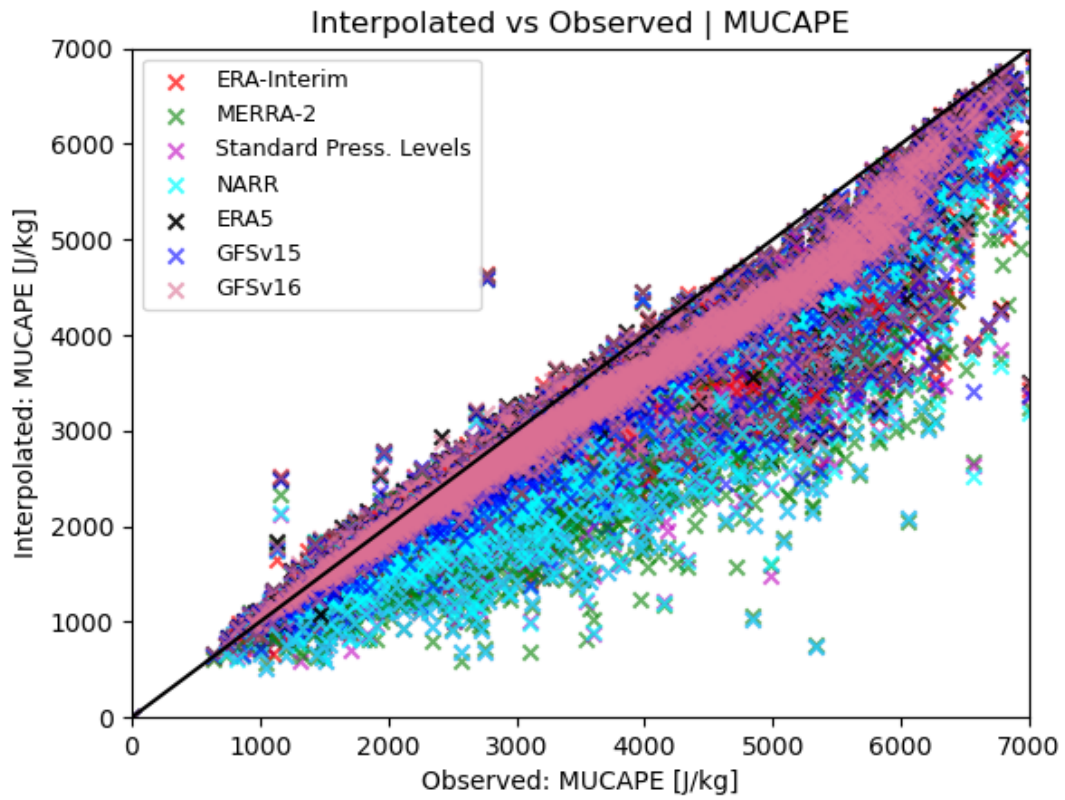Figure 22. Same as in Fig. 21, but displaying operational model interpolated sets.

Figure 23. Scatter plot showing relationship between the interpolated (y) and observed (x) datasets for SBCAPE with all campaigns. Legend displays each interpolated model/reanalysis dataset and its corresponding color marker.
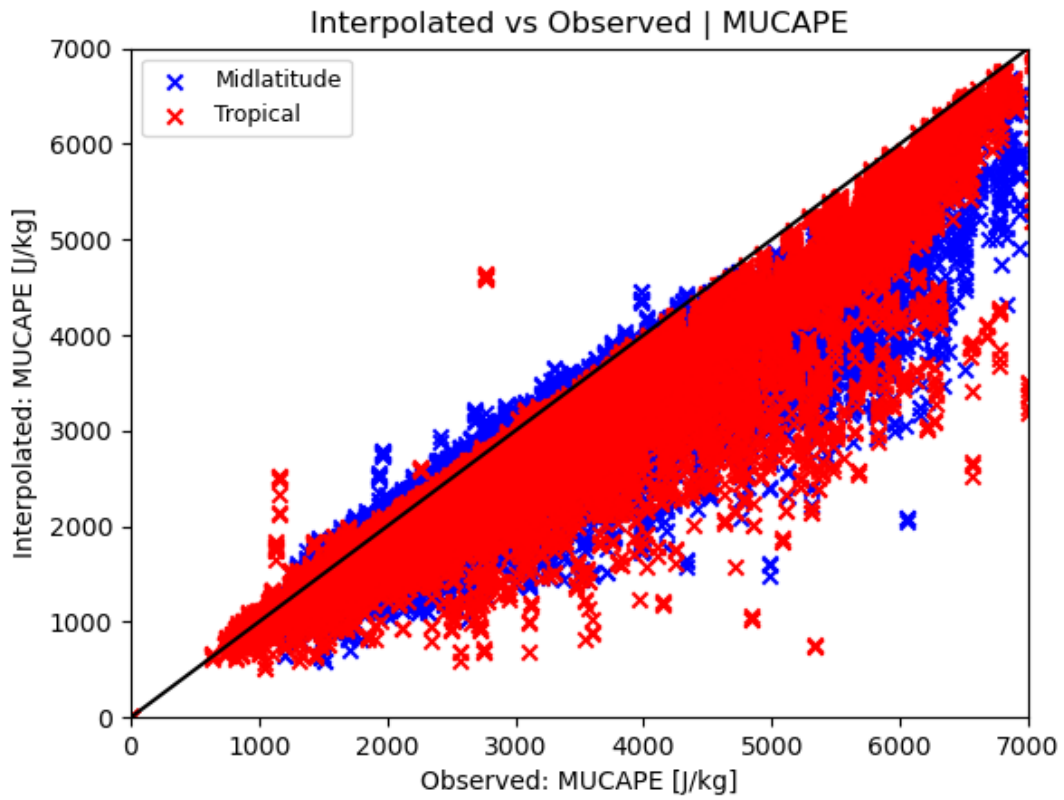
Figure 24. Scatter plot showing relationship between the interpolated (y) and observed (x) datasets for SBCAPE with all campaigns. Midlatitude campaigns (blue) and tropical campaigns (red).
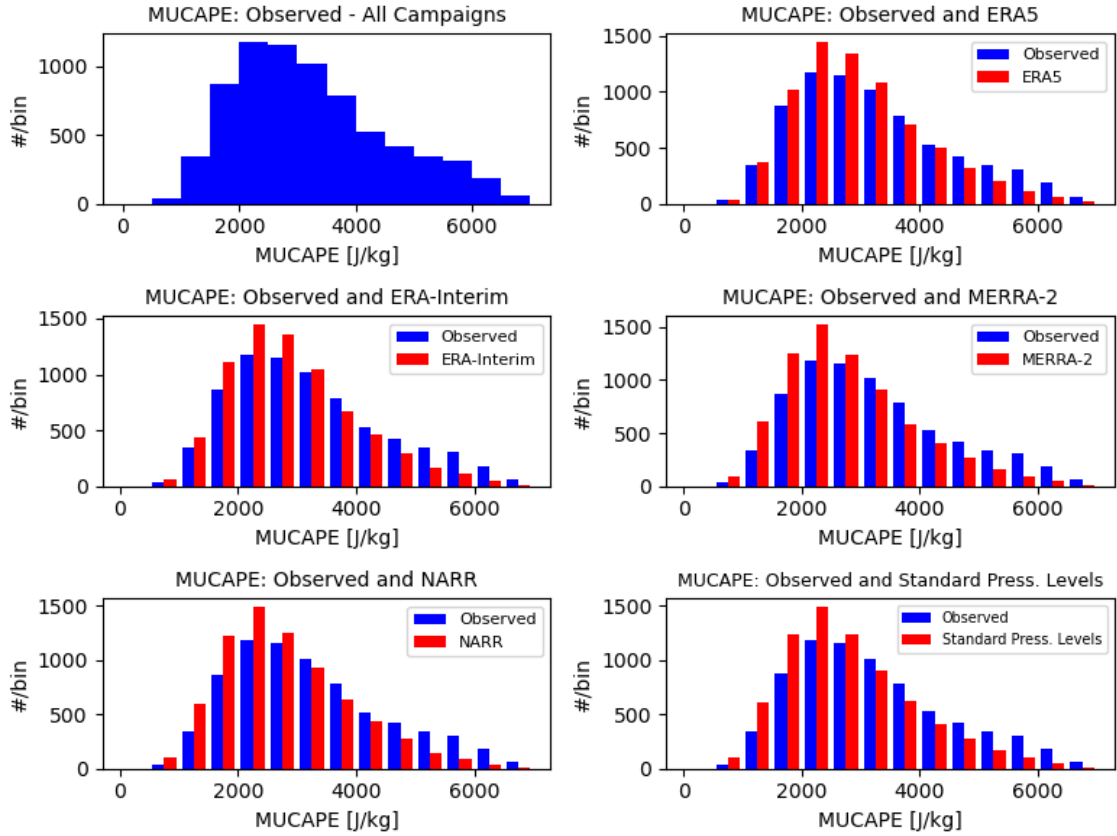
Figure 25. Subplots of histograms displaying SBCAPE distributions for all campaigns. Each

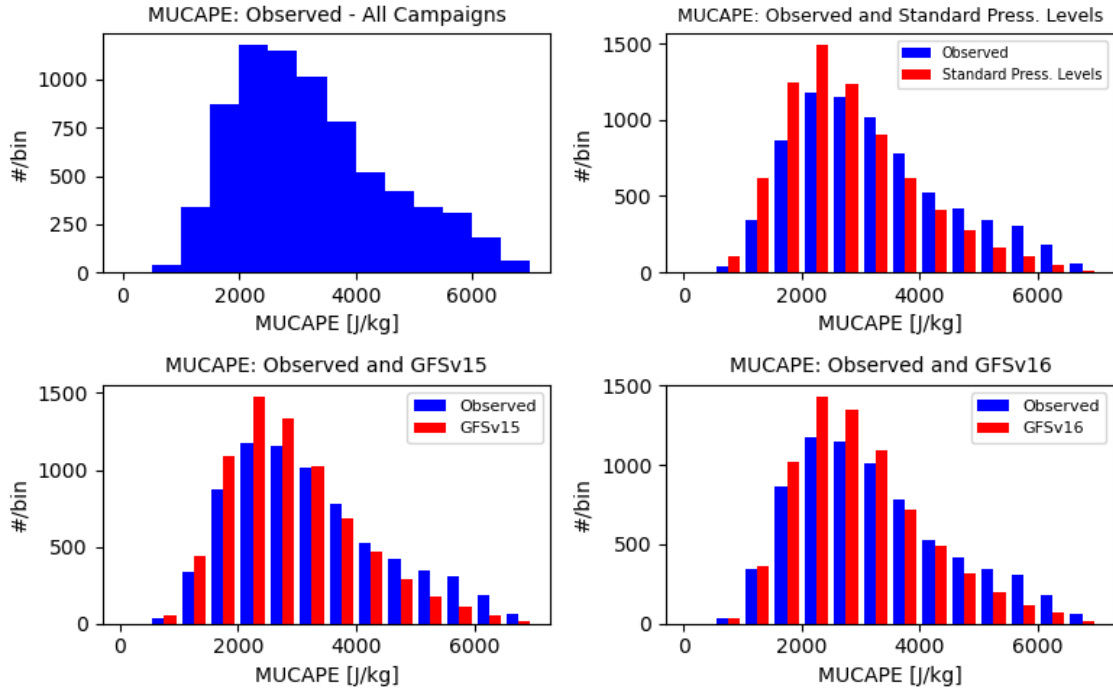subplot compares observed (blue) to model/reanalysis interpolated (red) SBCAPE.
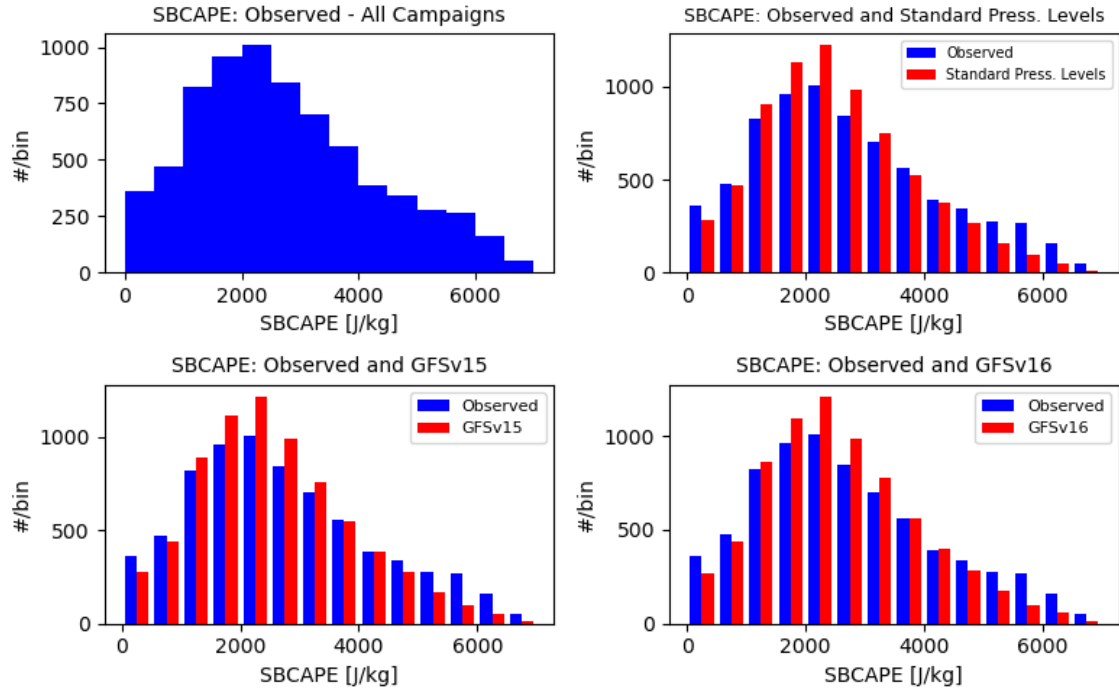
Figure 26. Same as in Fig. 25, but displaying operational model interpolated sets.

Figure 27. Scatter plot showing relationship between the interpolated (y) and observed (x)

datasets for MLCIN with all campaigns. Legend displays each interpolated model/reanalysis

dataset and its corresponding color marker.

Figure 28. Scatter plot showing relationship between the interpolated (y) and observed (x)

datasets for MLCIN with all campaigns. Midlatitude campaigns (blue) and tropical campaigns

(red).

Figure 29. Subplots of histograms displaying MLCIN distributions for all campaigns. Each subplot compares observed (blue) to model/reanalysis interpolated (red) MLCIN.

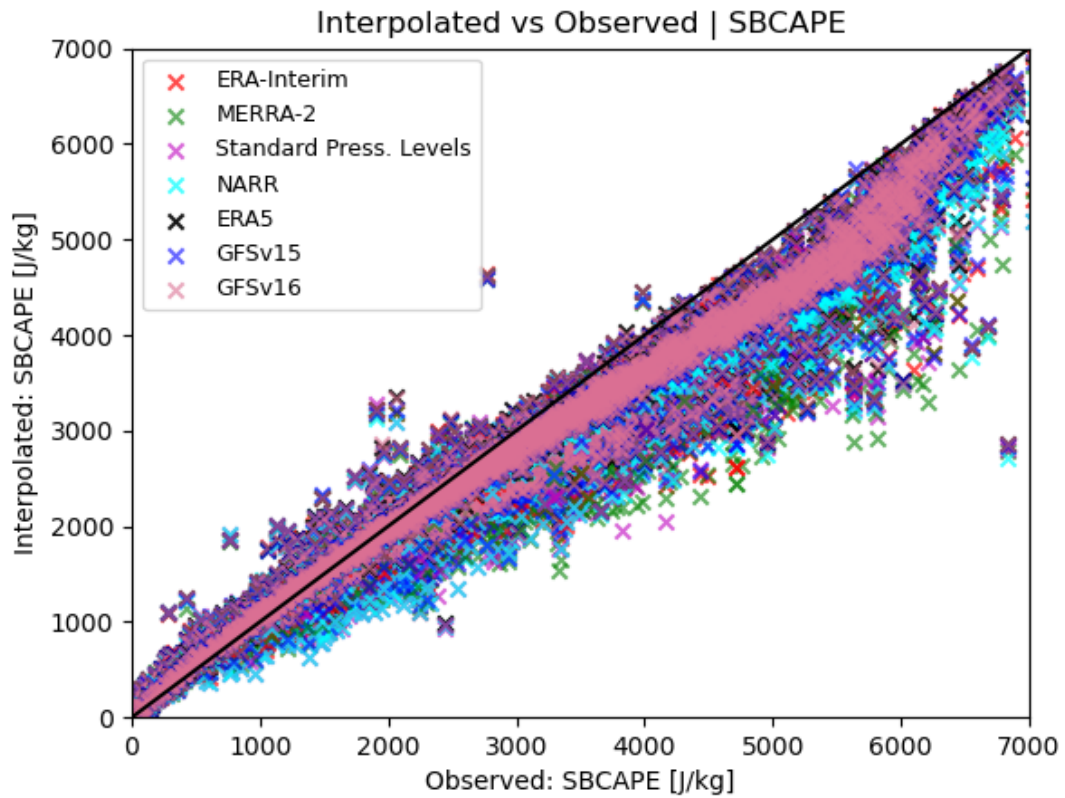Figure 30. Same as in Fig. 29, but displaying operational model interpolated sets.

Figure 31. Scatter plot showing relationship between the interpolated (y) and observed (x)

datasets for MUCIN with all campaigns. Legend displays each interpolated model/reanalysis
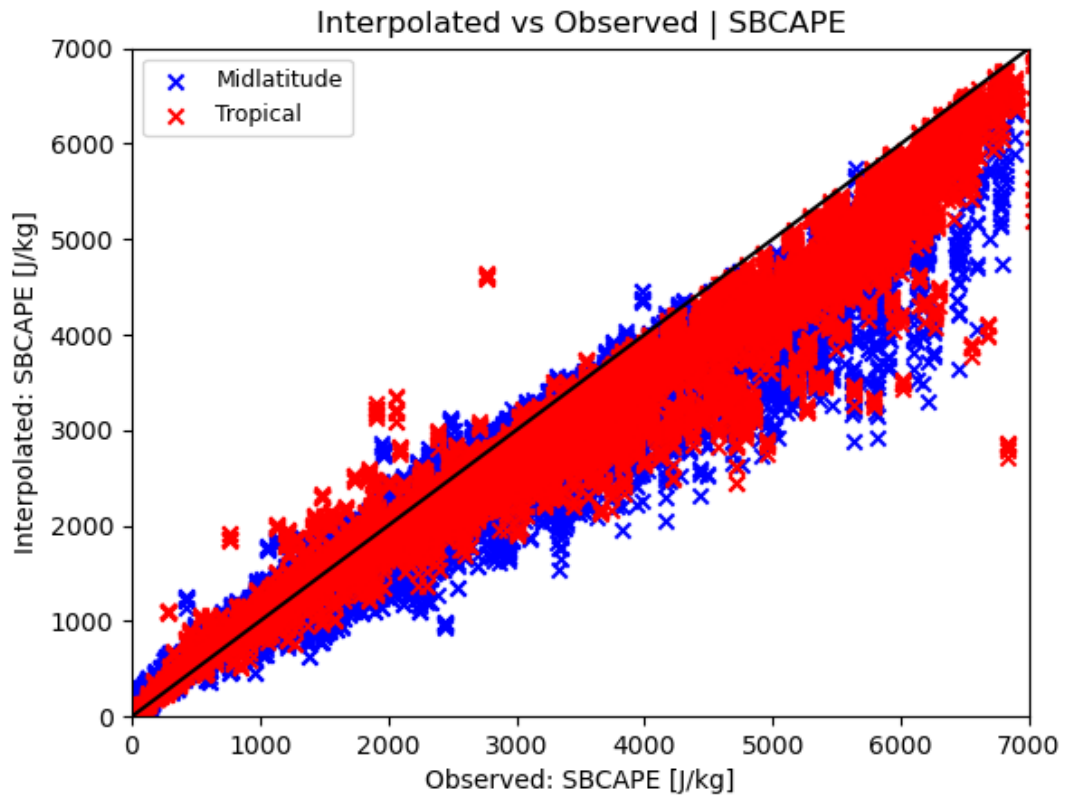
dataset and its corresponding color marker.

Figure 32. Scatter plot showing relationship between the interpolated (y) and observed (x)

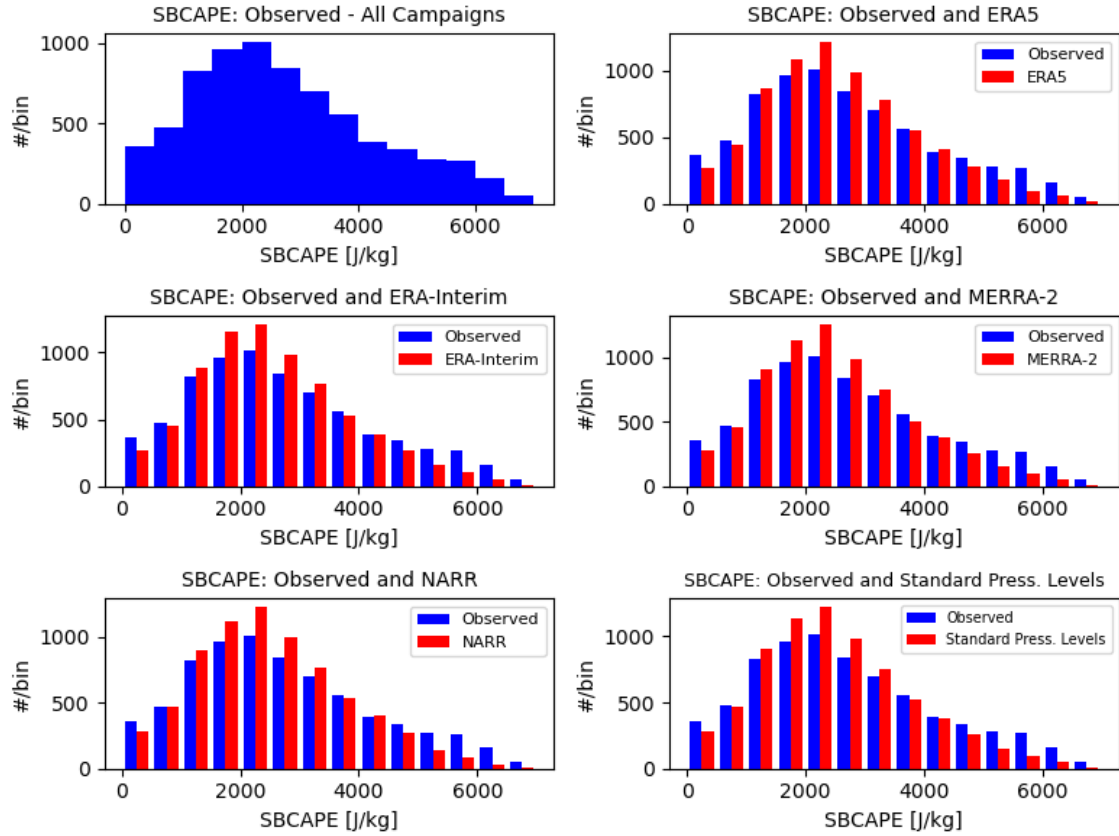datasets for MUCIN with all campaigns. Midlatitude campaigns (blue) and tropical campaigns

(red).
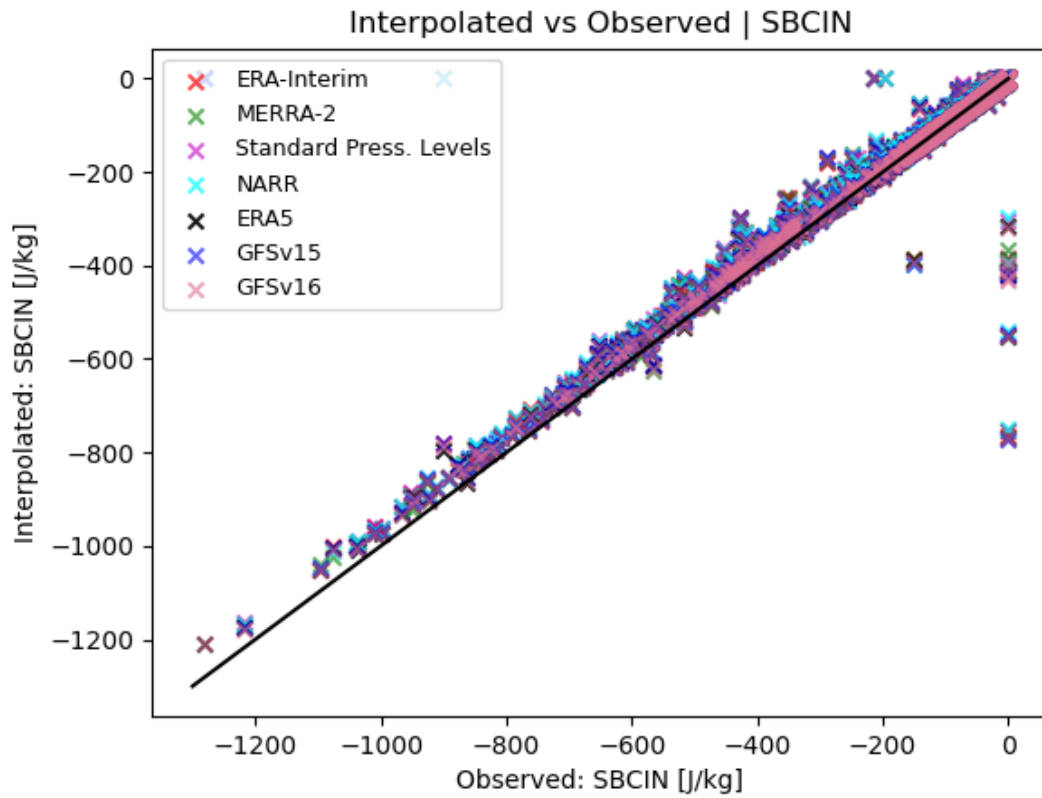
Figure 33. Scatter plot showing relationship between the interpolated (y) and observed (x) datasets for SBCIN with all campaigns. Legend displays each interpolated model/reanalysis dataset and its corresponding color marker.
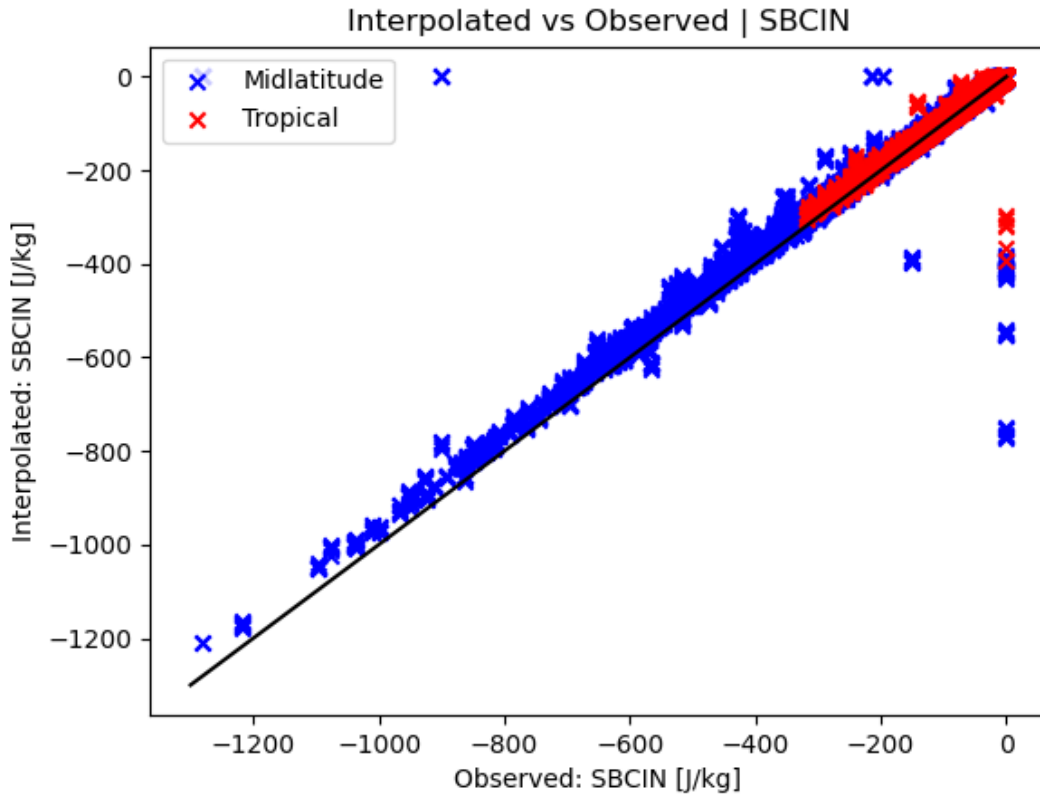
Figure 34. Scatter plot showing relationship between the interpolated (y) and observed (x) datasets for SBCIN with all campaigns. Midlatitude campaigns (blue) and tropical campaigns (red).
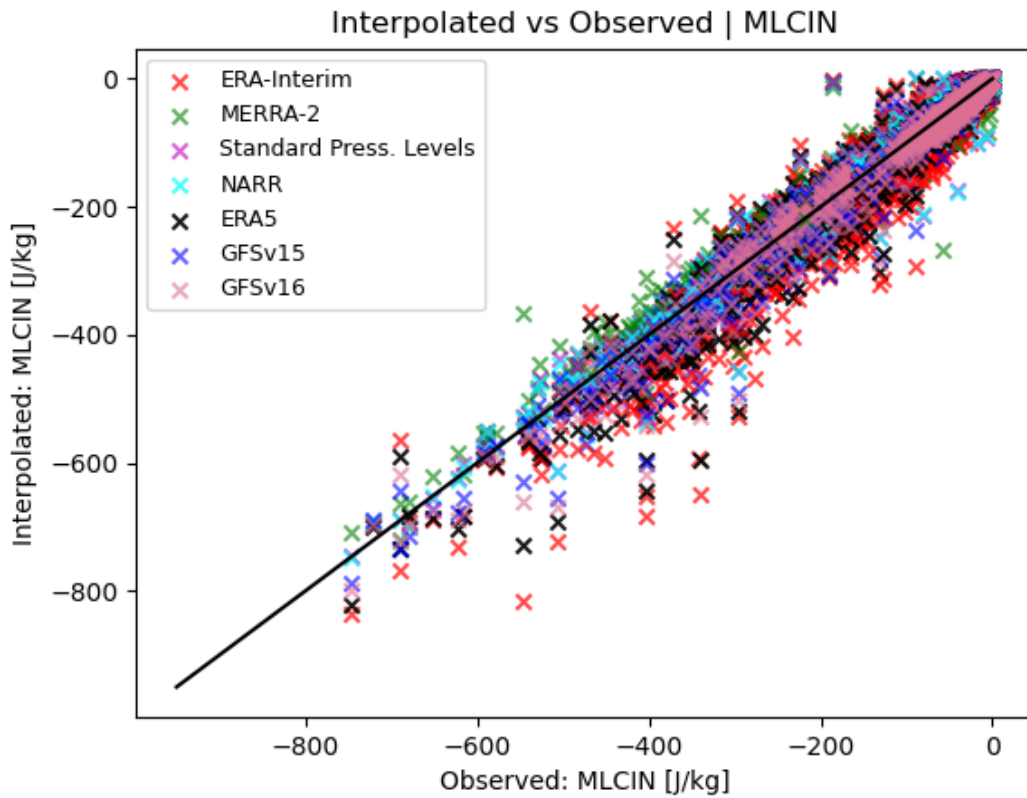
Figure 35. Scatter plot showing relationship between the interpolated (y) and observed (x) datasets for 0-6 km bulk shear with all campaigns. Legend displays each interpolated model/reanalysis dataset and its corresponding color marker.
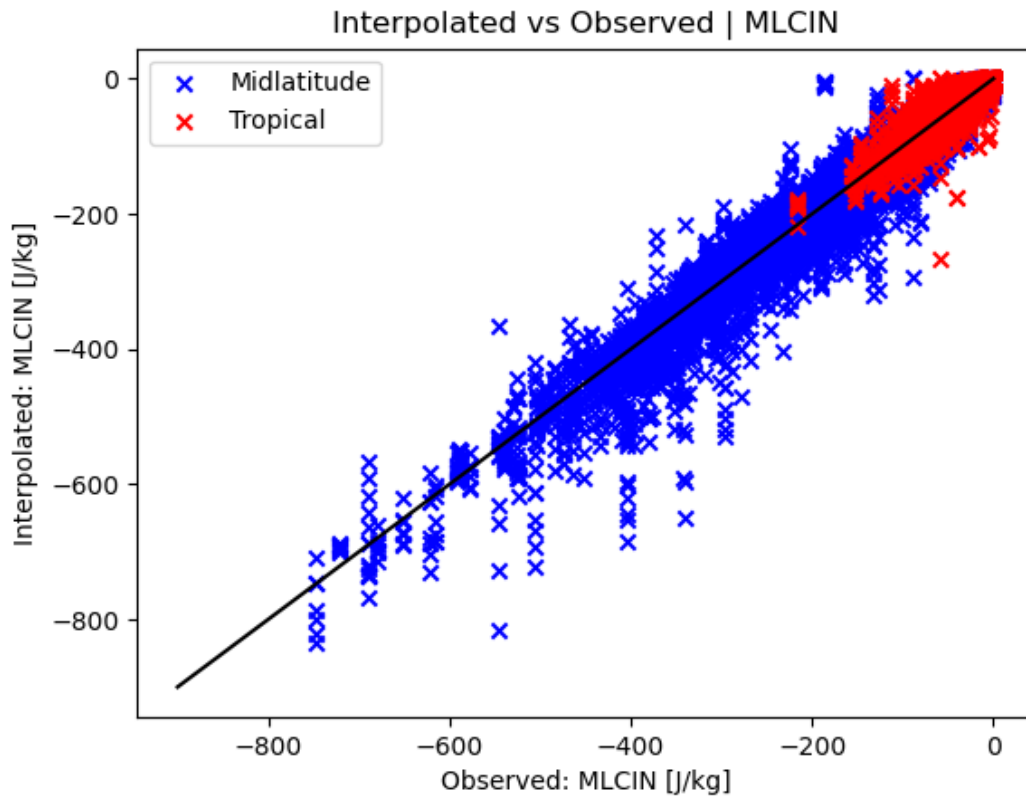
Figure 36. Scatter plot showing relationship between the interpolated (y) and observed (x) datasets for 0-6 km bulk shear with all campaigns. Midlatitude campaigns (blue) and tropical campaigns (red).
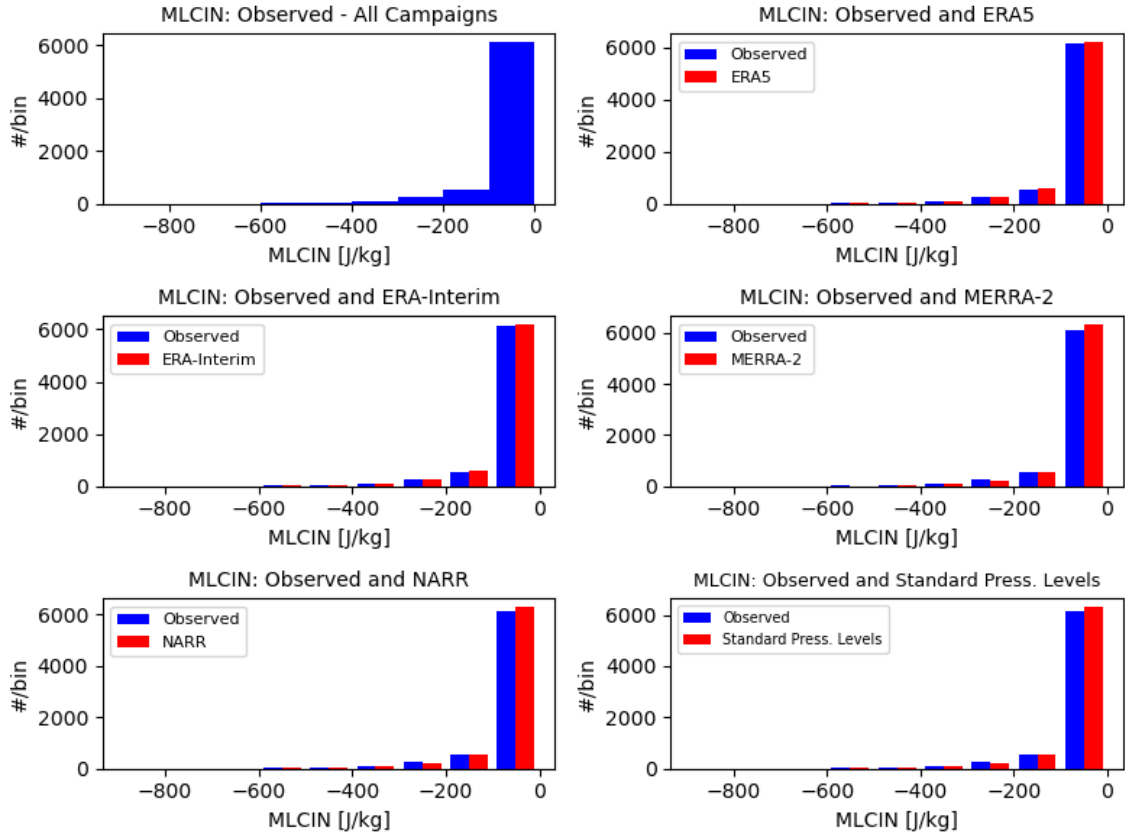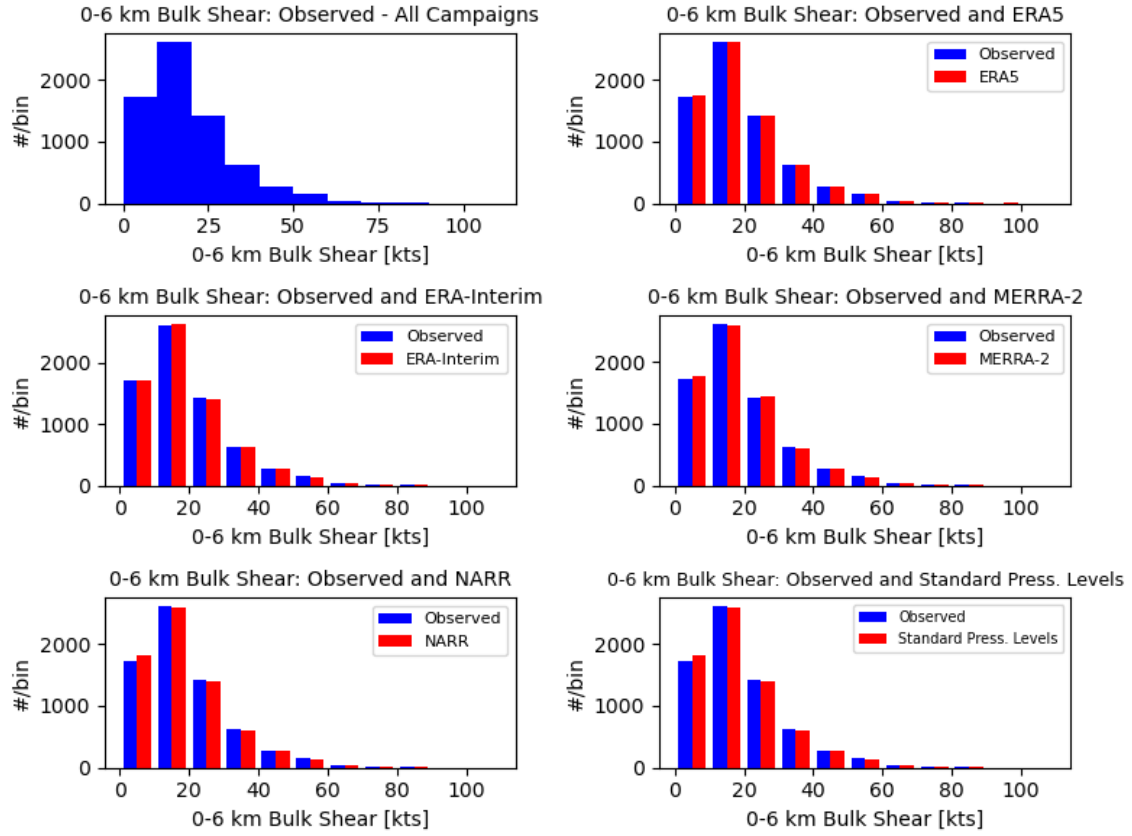
Figure 37. Subplots of histograms displaying 0-6 km bulk shear distributions for all campaigns.

Each subplot compares observed (blue) to model/reanalysis interpolated (red) 0-6 km bulk shear.
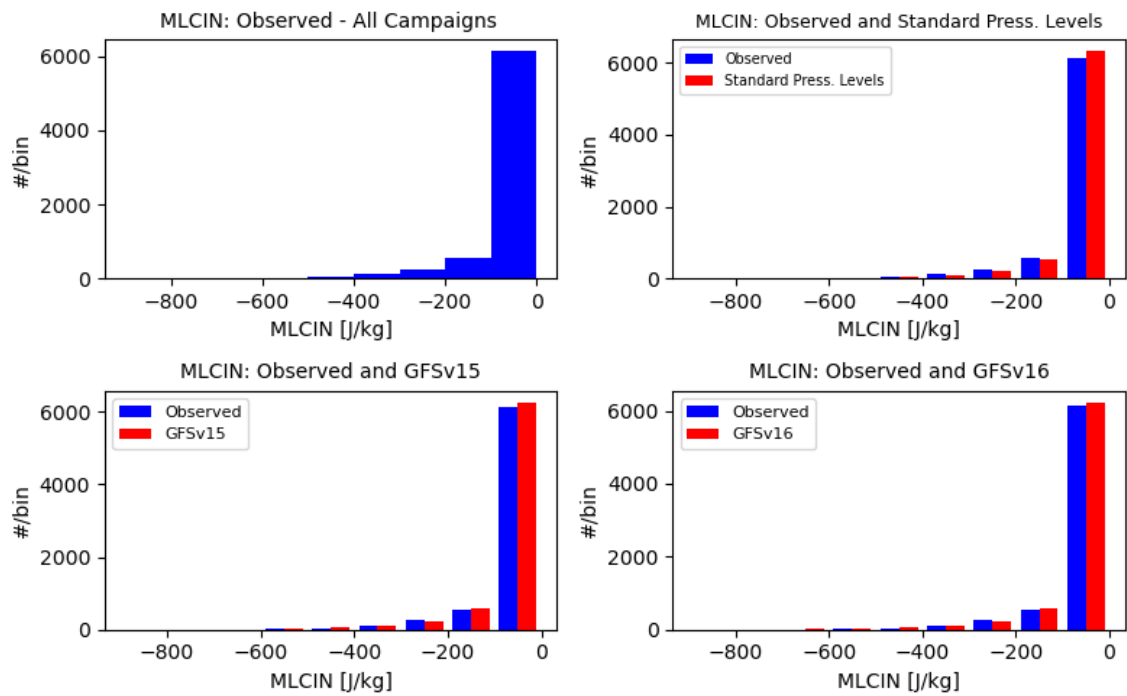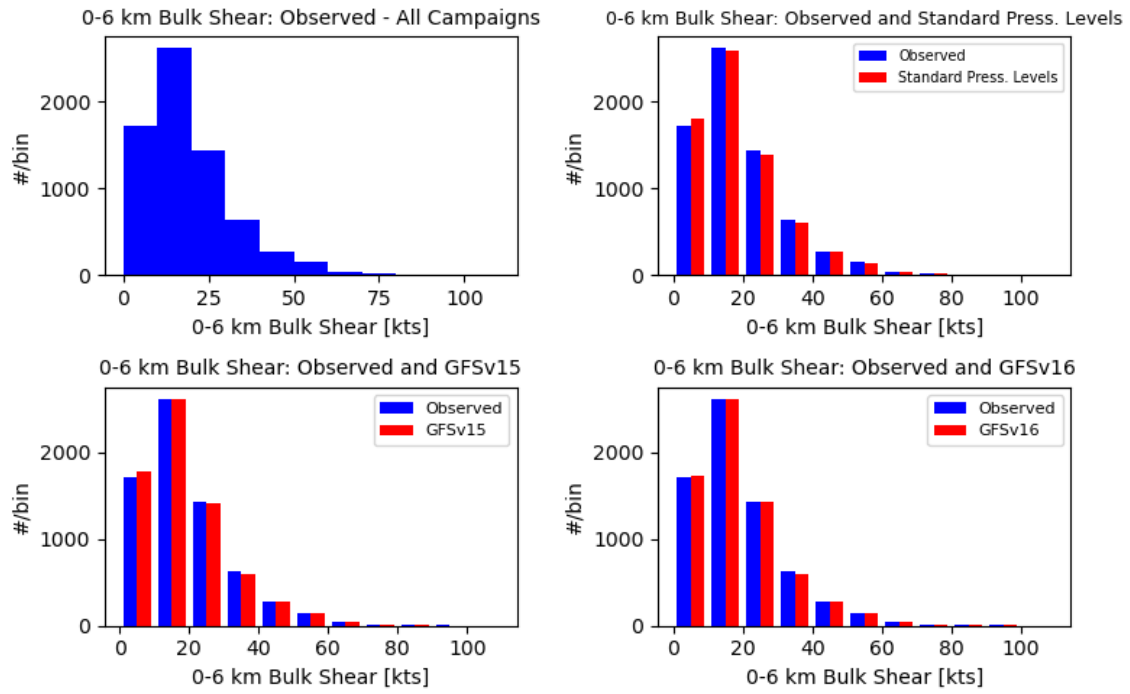
Figure 38. Same as in Fig. 37, but displaying operational model interpolated sets.
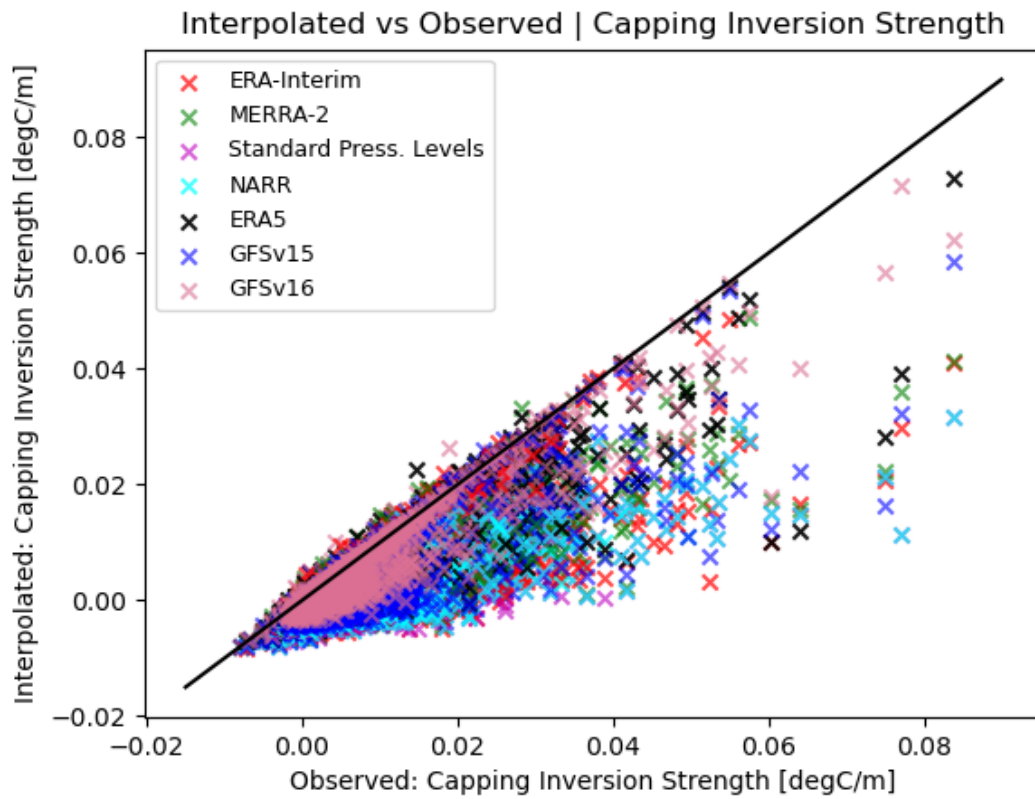
Figure 39. Scatter plot showing relationship between the interpolated (y) and observed (x) datasets for capping inversion strength with all campaigns. Legend displays each interpolated model/reanalysis dataset and its corresponding color. marker.
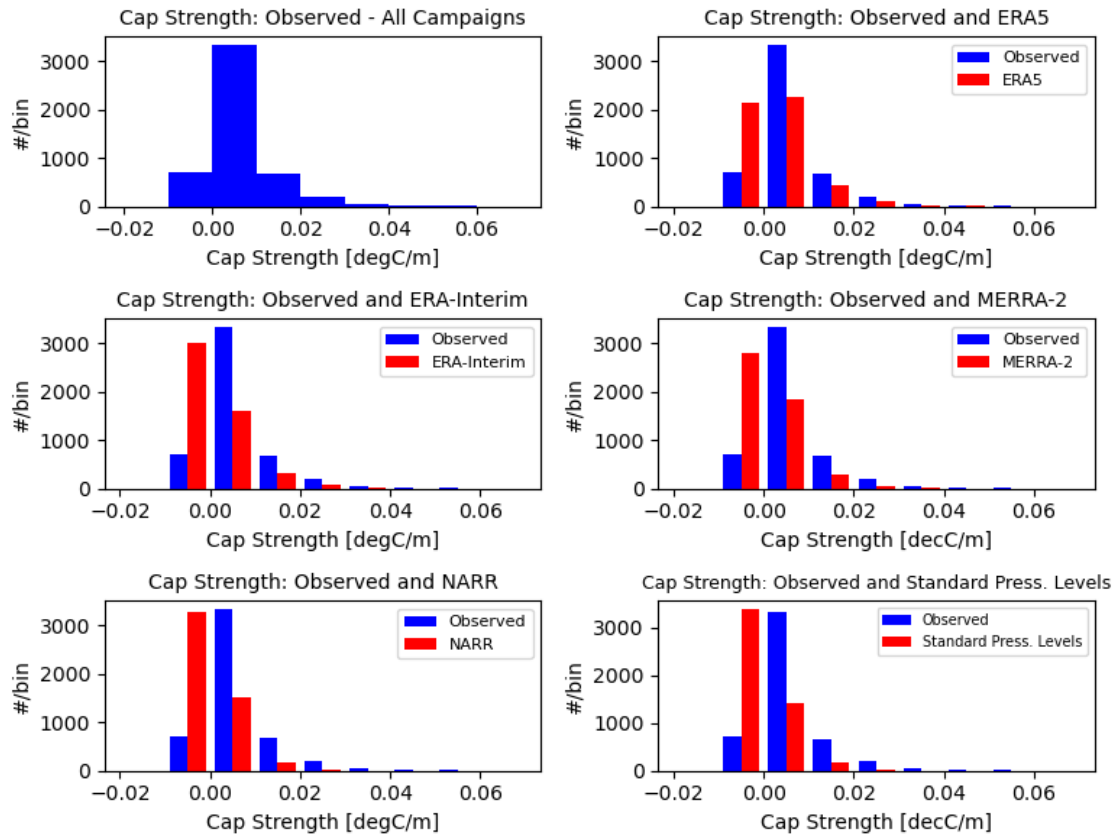
Figure 40. Subplots of histograms displaying cap strength distributions for all campaigns. Each subplot compares observed (blue) to model/reanalysis interpolated (red) cap strength.
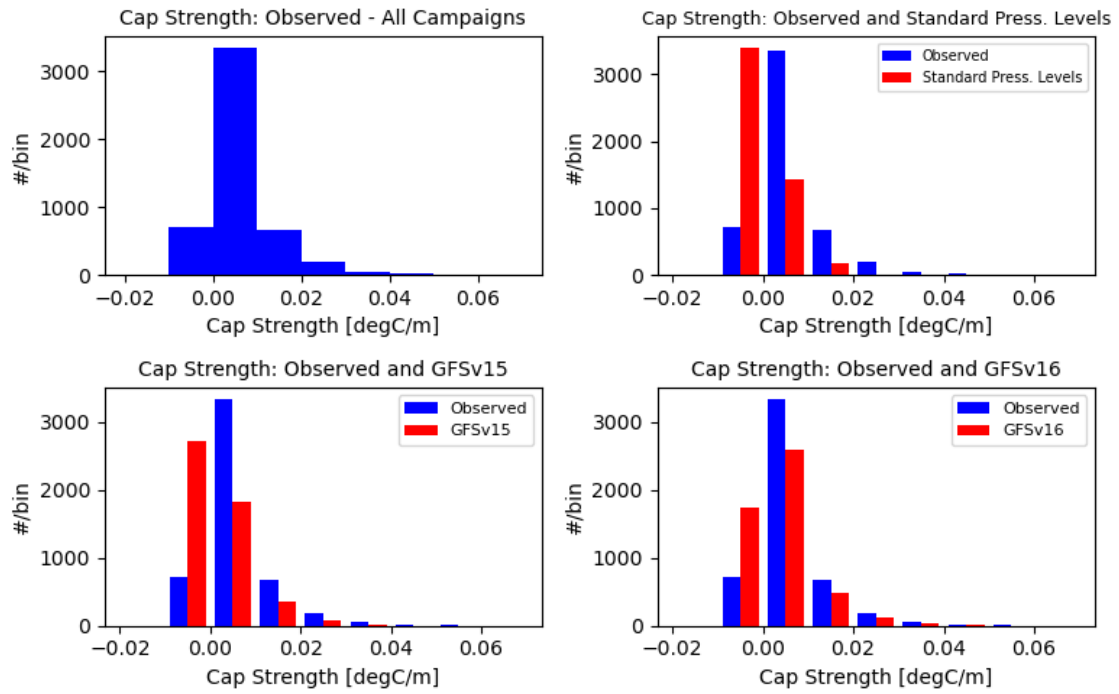
Figure 41. Same as in Fig. 40, but displaying operational model interpolated sets.
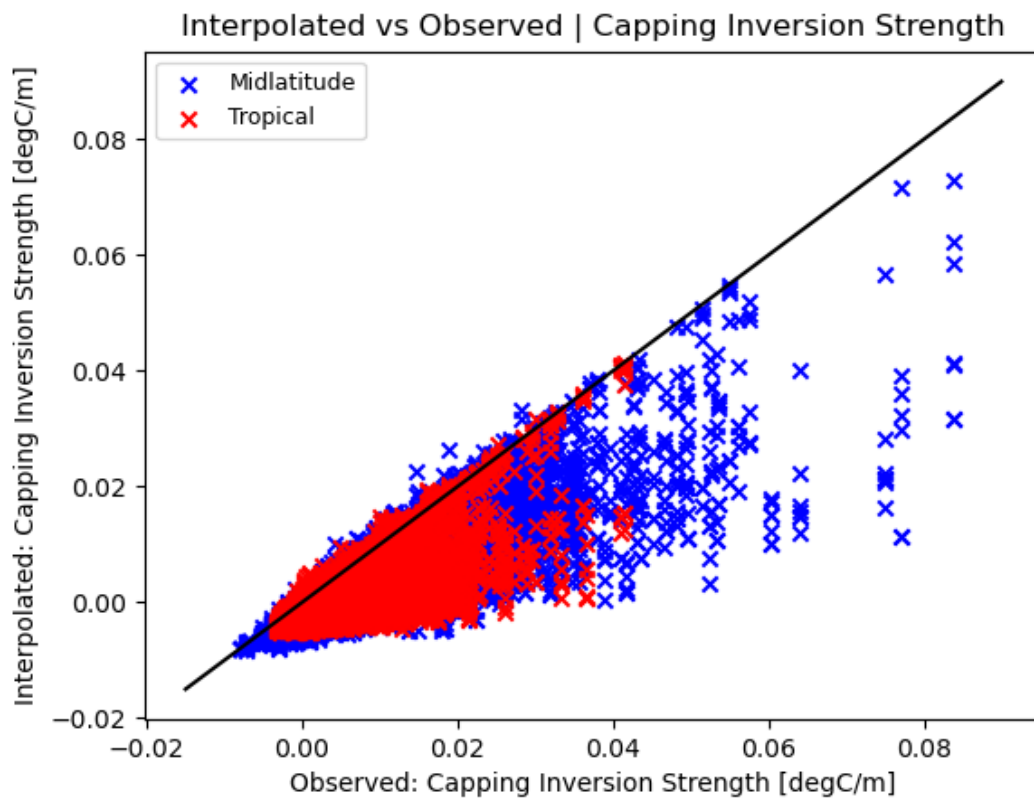
Figure 42. Scatter plot showing relationship between the interpolated (y) and observed (x) datasets for capping inversion strength with all campaigns. Midlatitude campaigns (blue) and tropical campaigns (red).
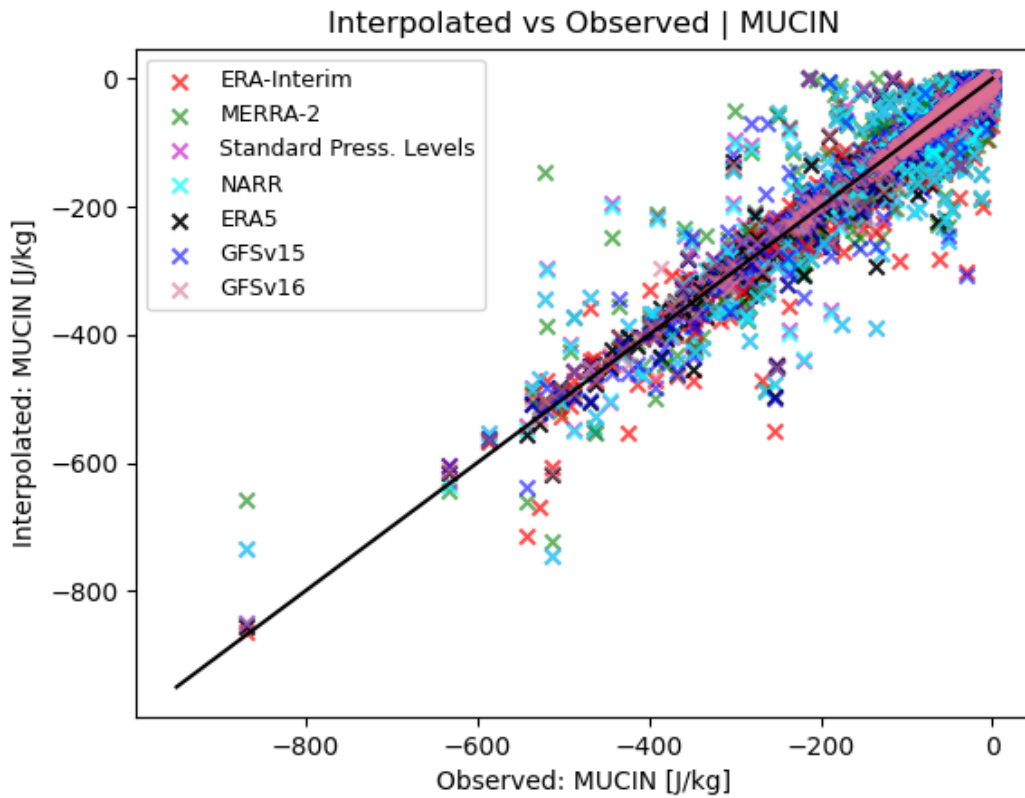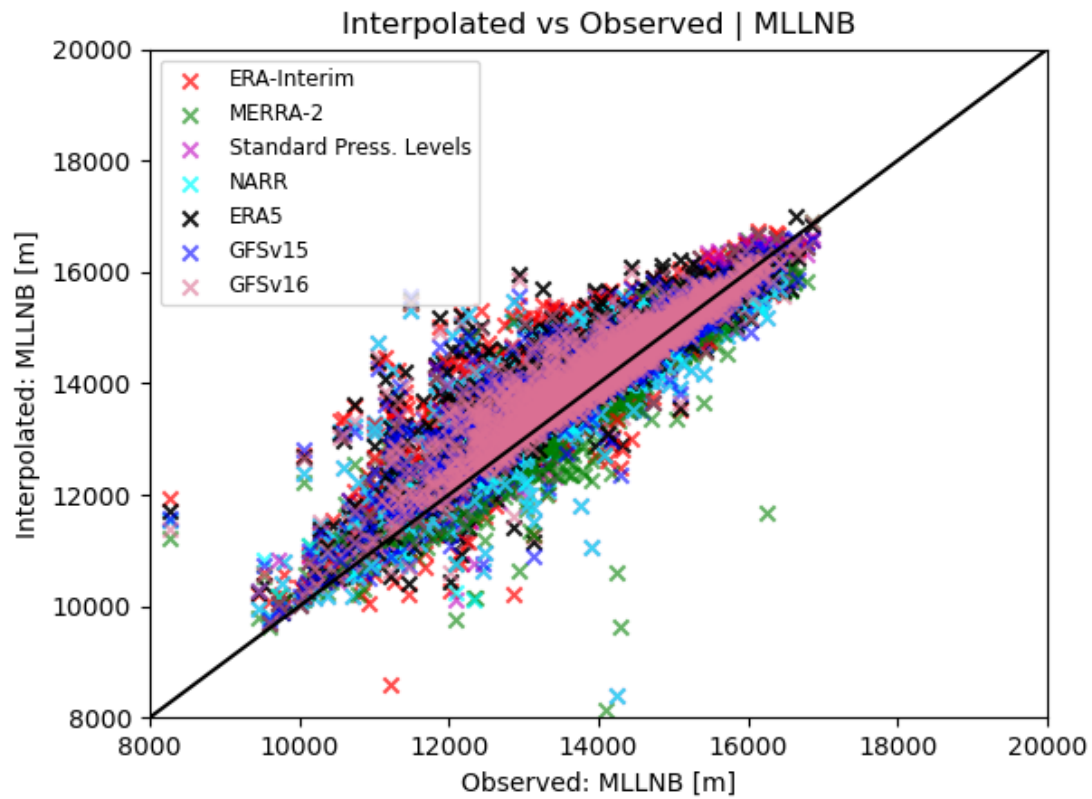
Figure 43. Scatter plot showing relationship between the interpolated (y) and observed (x) datasets for MLLNB with all campaigns. Legend displays each interpolated model/reanalysis dataset and its corresponding color marker.
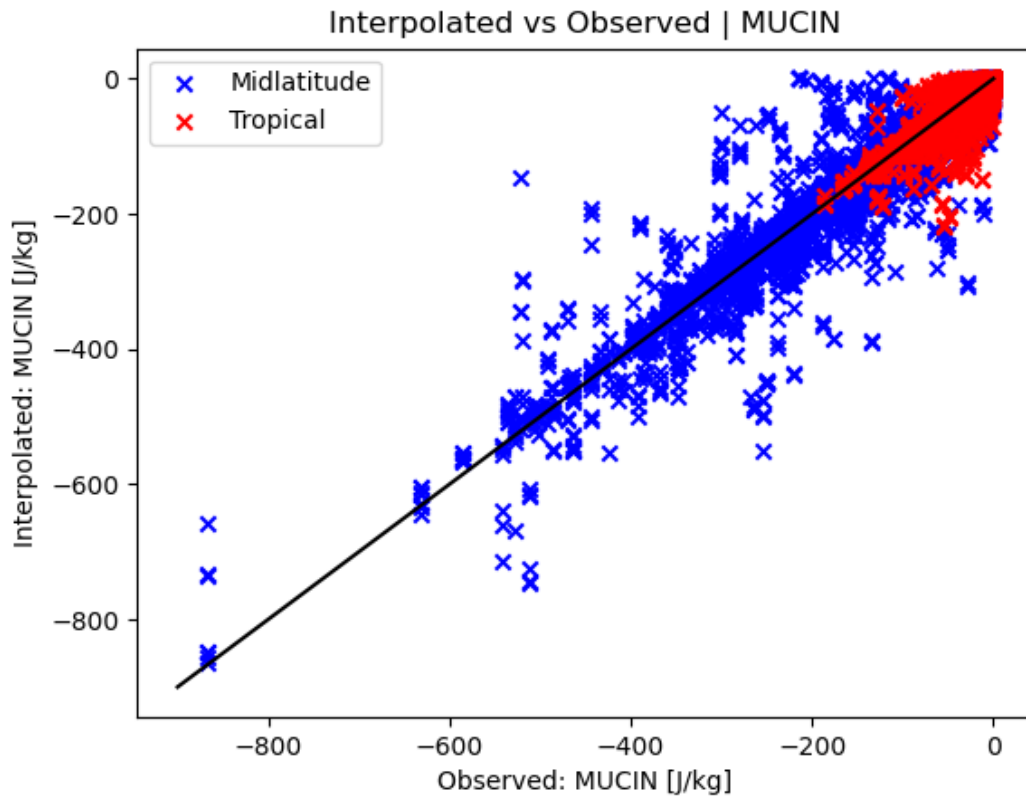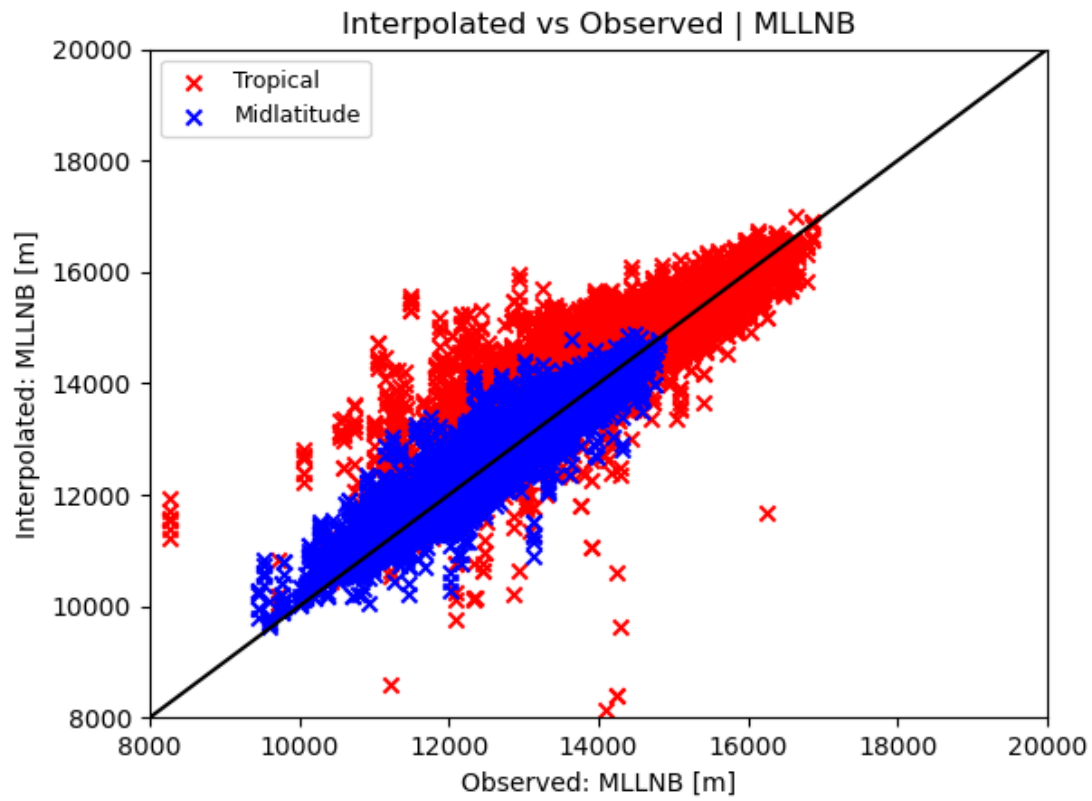
Figure 44. Scatter plot showing relationship between the interpolated (y) and observed (x)

datasets for MLLNB with all campaigns. Midlatitude campaigns (blue) and tropical campaigns

(red).
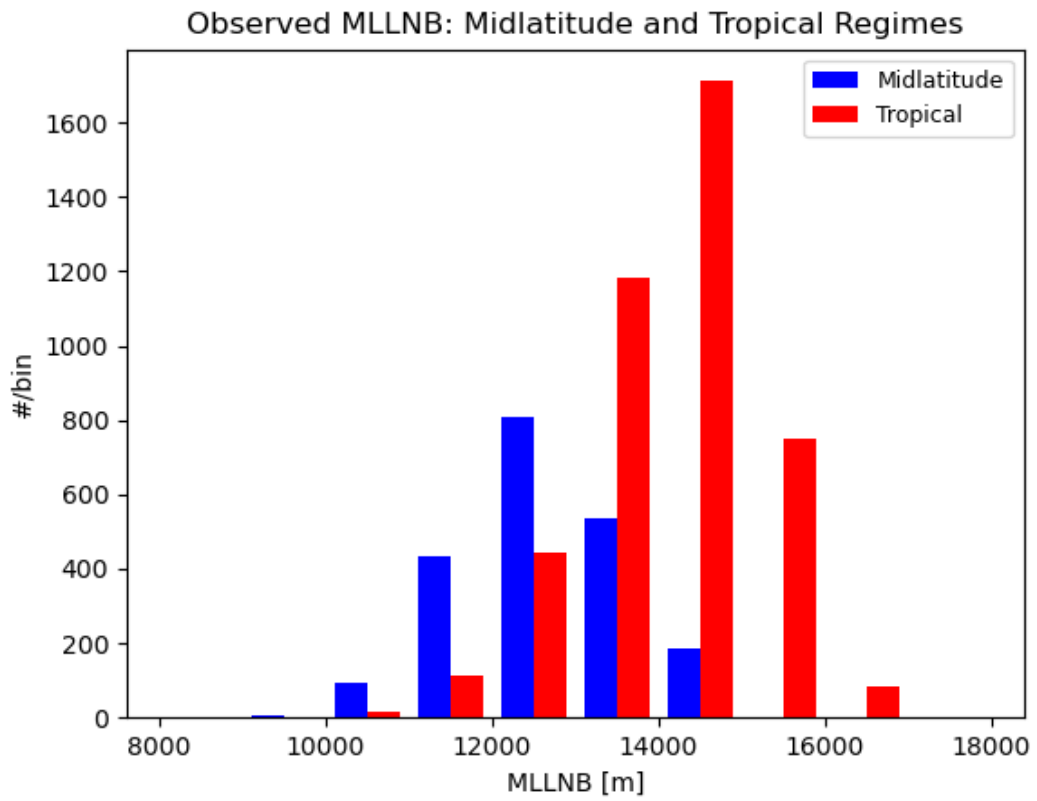
Figure 45. Histogram displaying observed distributions for MLLNB categorized by regime type.

Midlatitude campaigns (blue) and tropical campaigns (red).
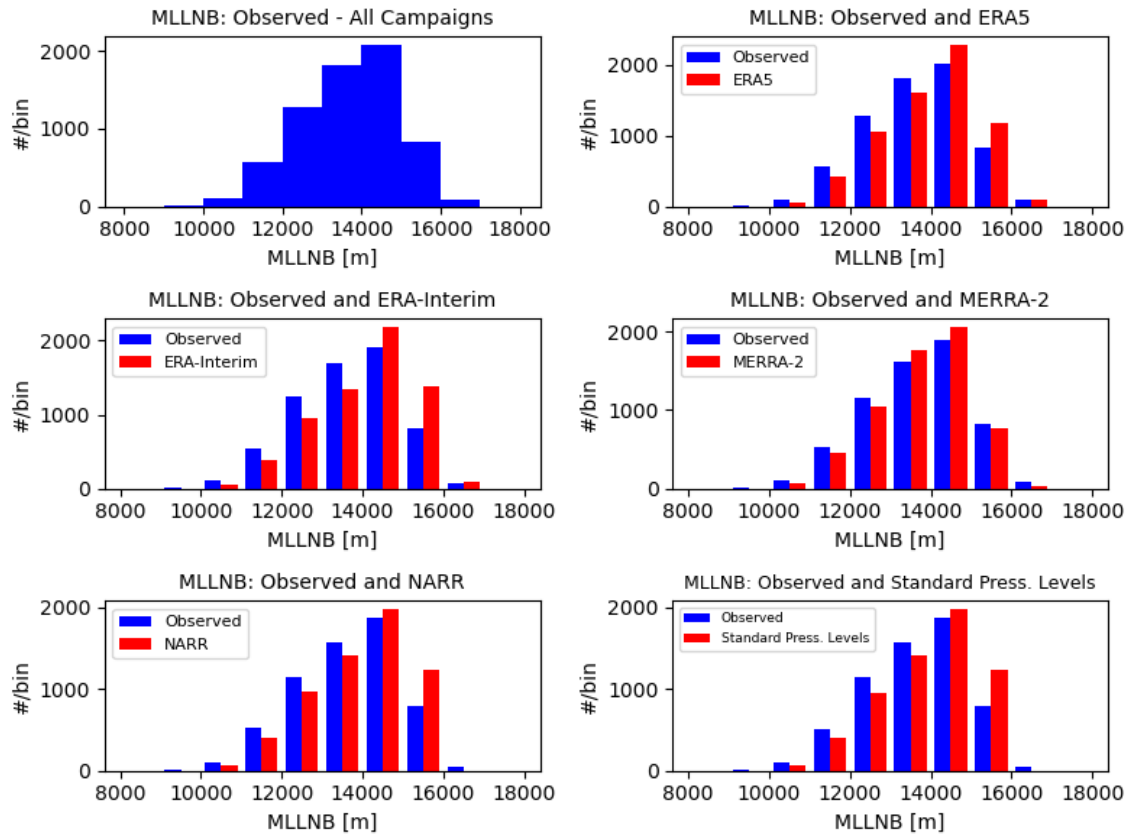
Figure 46. Subplots of histograms displaying MLLNB for all campaigns. Each subplot compares

observed (blue) to model/reanalysis interpolated (red) MLLNB.
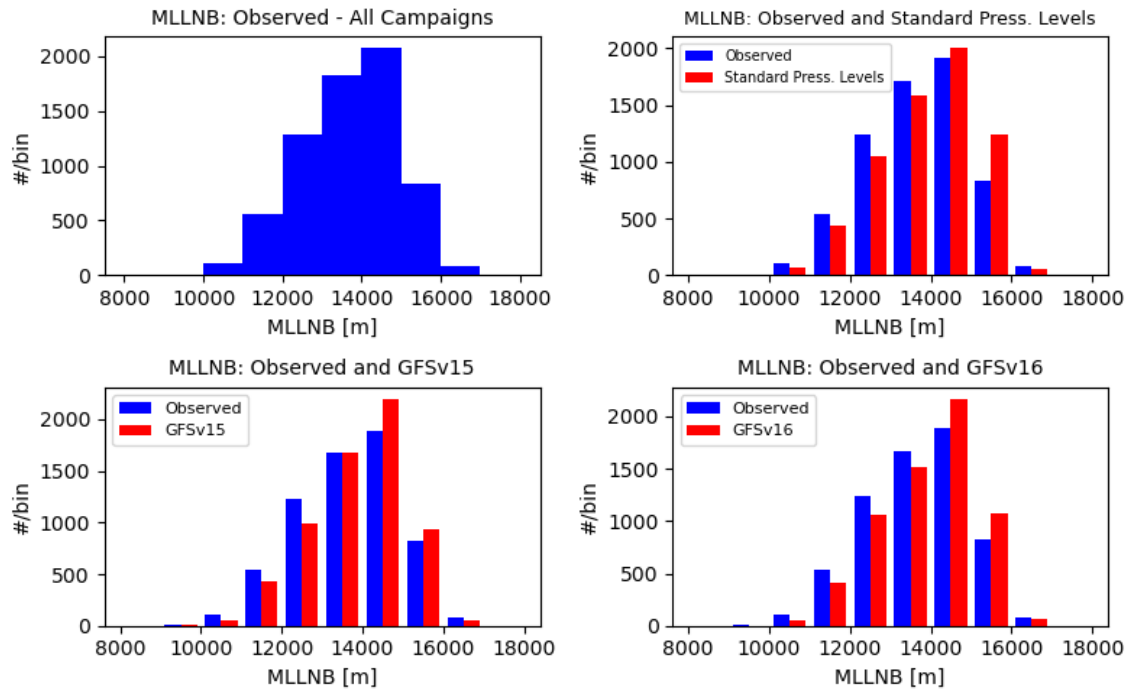
Figure 47. Same as in Fig. 46, but displaying operational model interpolated sets.
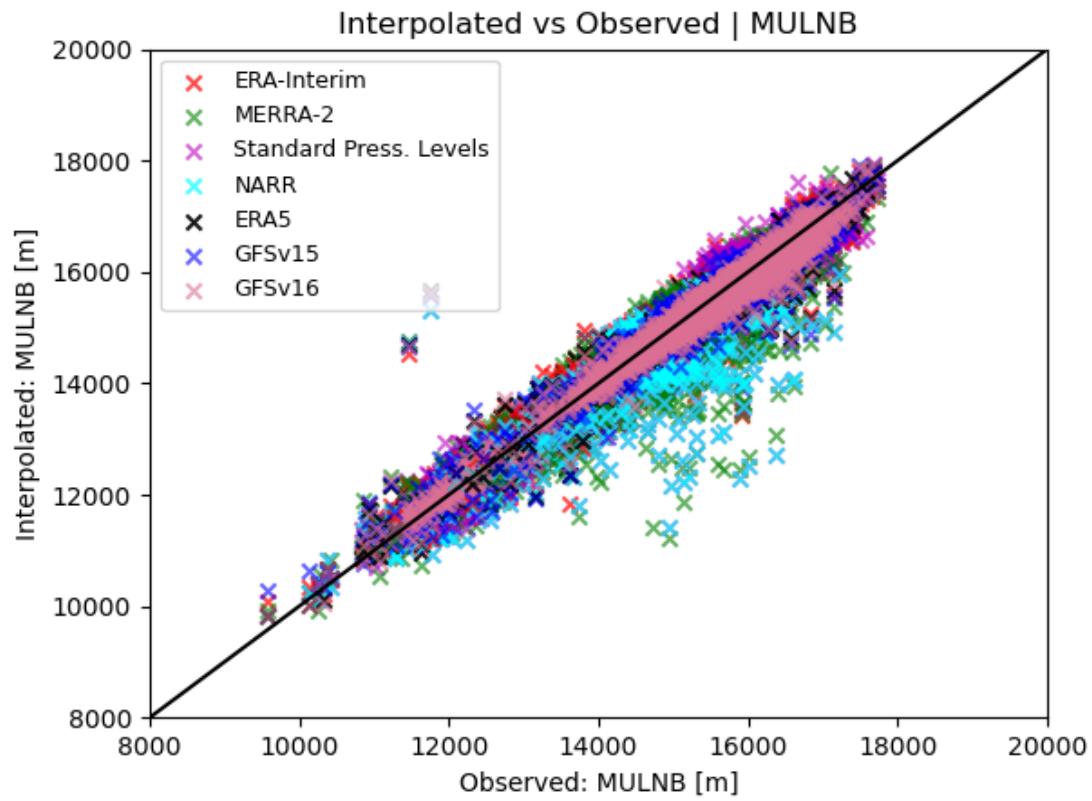
Figure 48. Scatter plot showing relationship between the interpolated (y) and observed (x) datasets for MULNB with all campaigns. Legend displays each interpolated model/reanalysis dataset and its corresponding color marker.
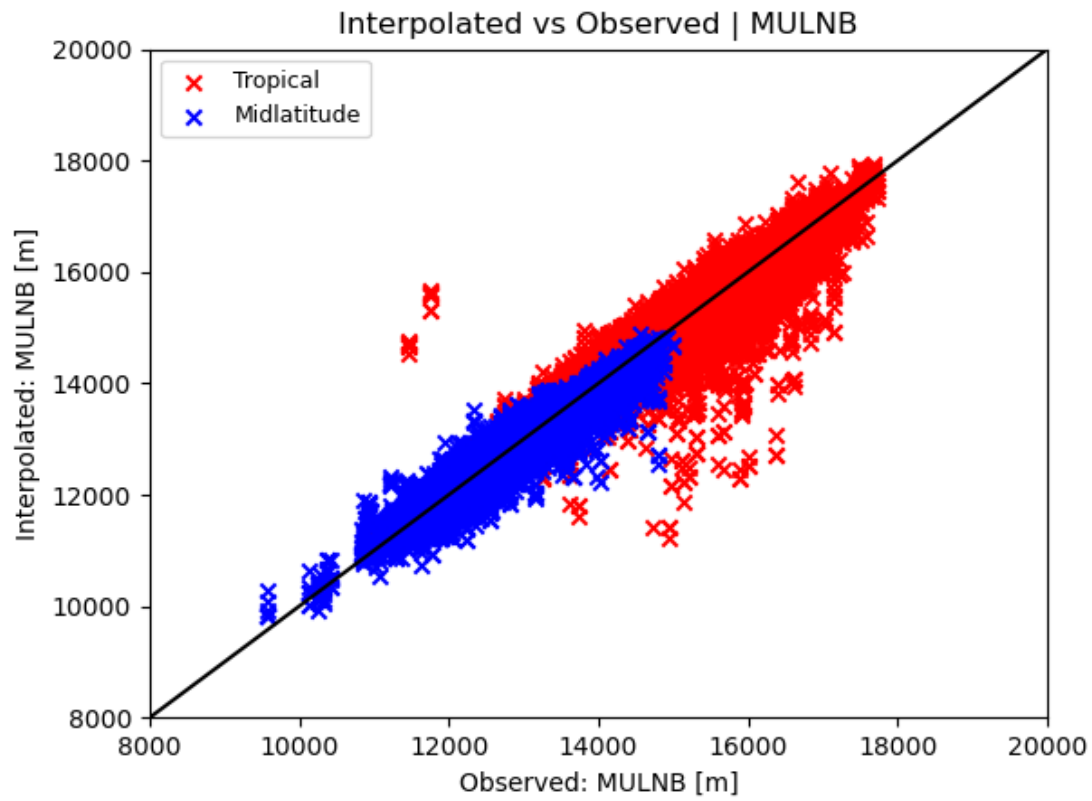
Figure 49. Scatter plot showing relationship between the interpolated (y) and observed (x)

datasets for MULNB with all campaigns. Midlatitude campaigns (blue) and tropical campaigns
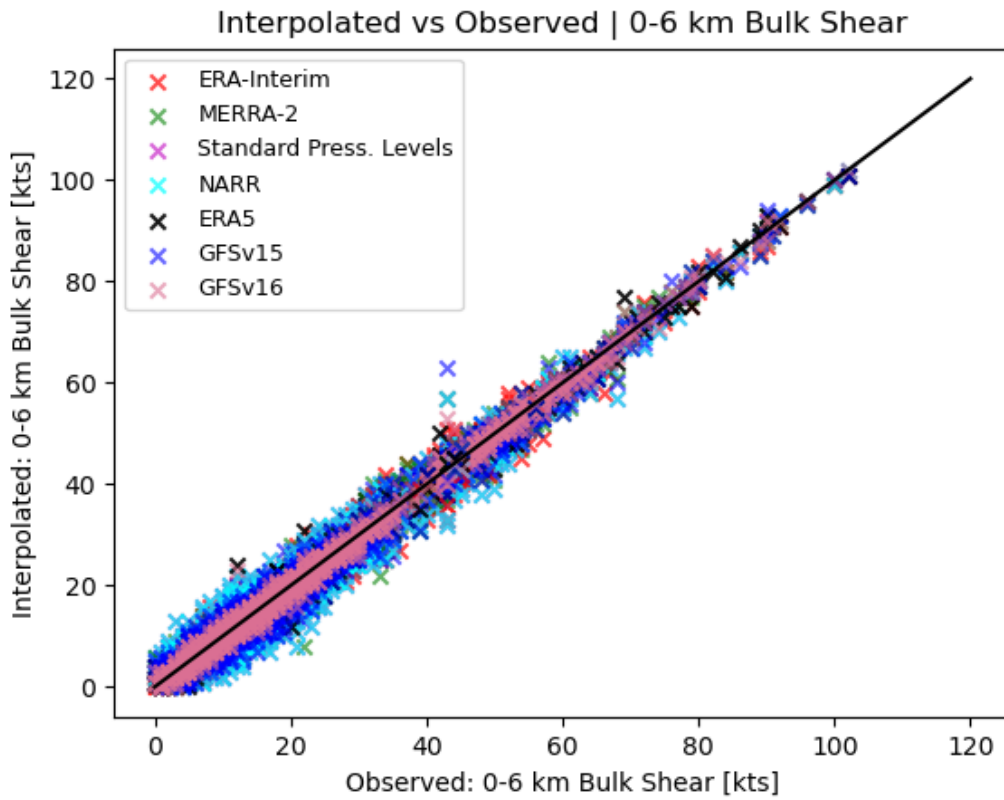
(red).
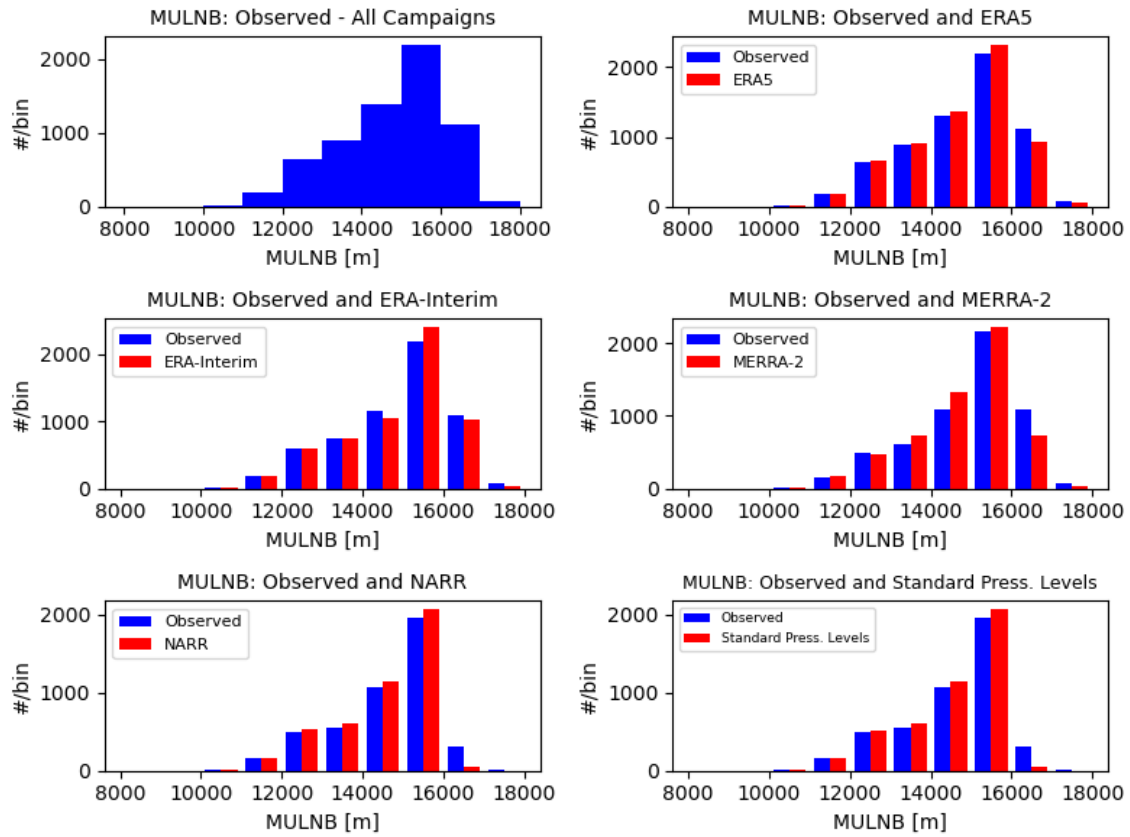
Figure 50. Subplots of histograms displaying MULNB for all campaigns. Each subplot compares

observed (blue) to model/reanalysis interpolated (red) MULNB.
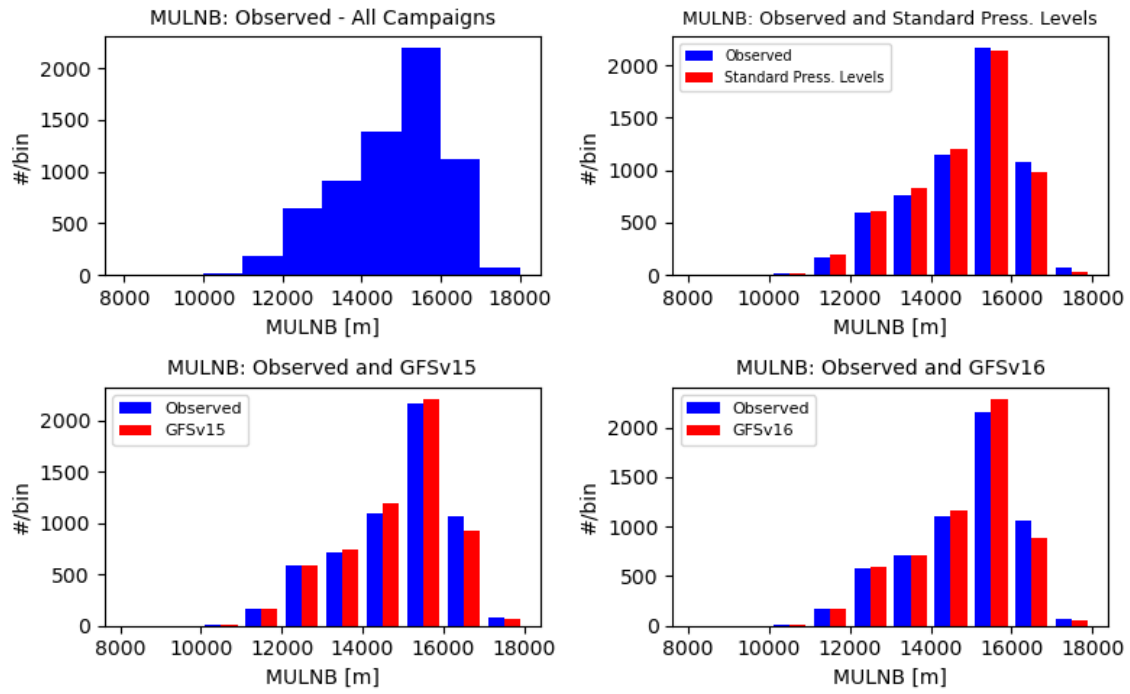
Figure 51. Same as in Fig. 50, but displaying operational model interpolated sets.
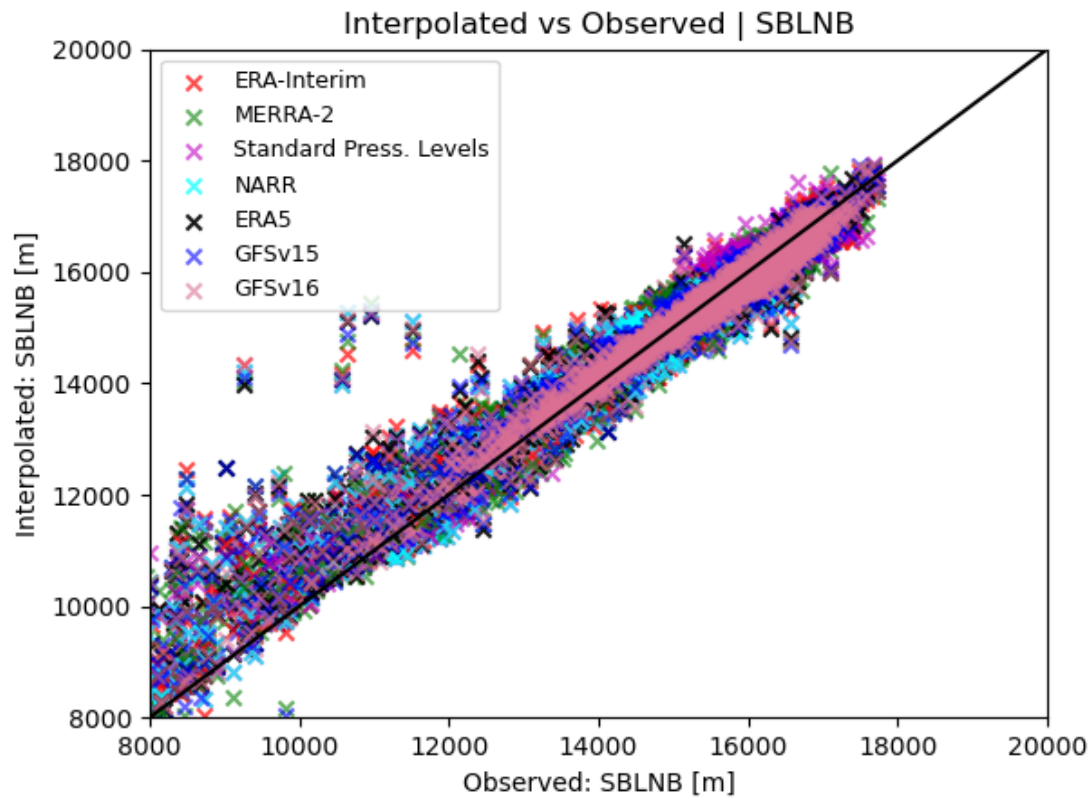
Figure 52. Scatter plot showing relationship between the interpolated (y) and observed (x)

datasets for SBLNB with all campaigns. Legend displays each interpolated model/reanalysis
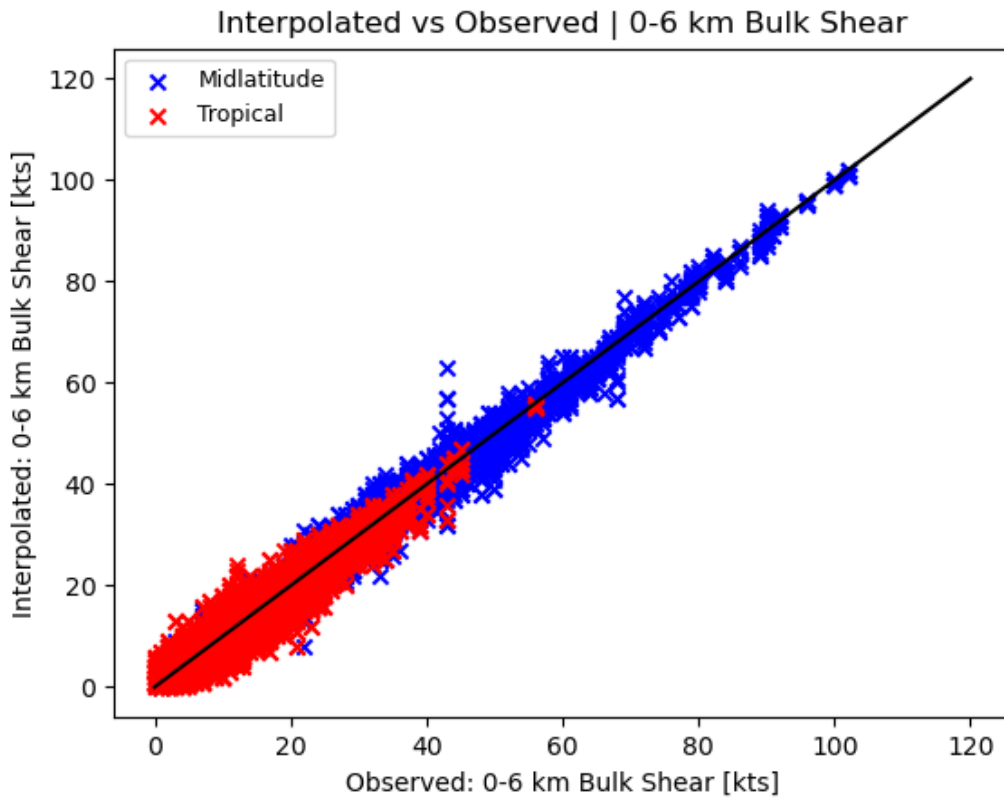
dataset and its corresponding color marker.
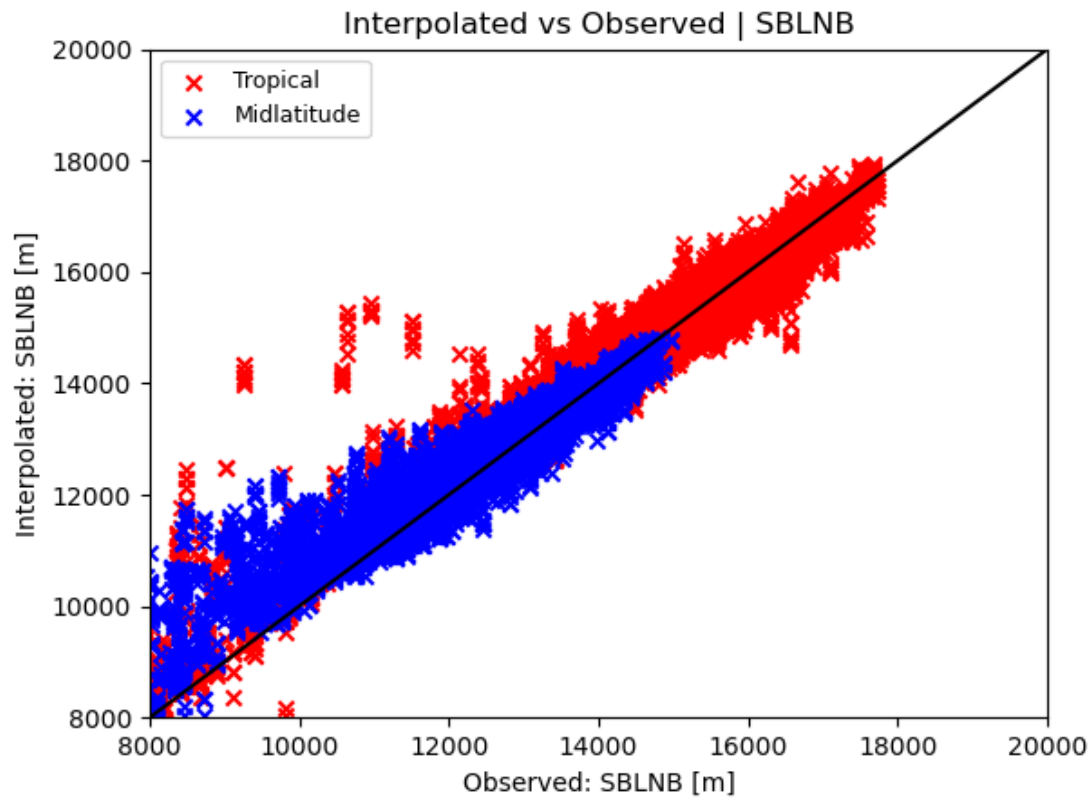
Figure 53. Scatter plot showing relationship between the interpolated (y) and observed (x)

datasets for SBLNB with all campaigns. Midlatitude campaigns (blue) and tropical campaigns

(red).
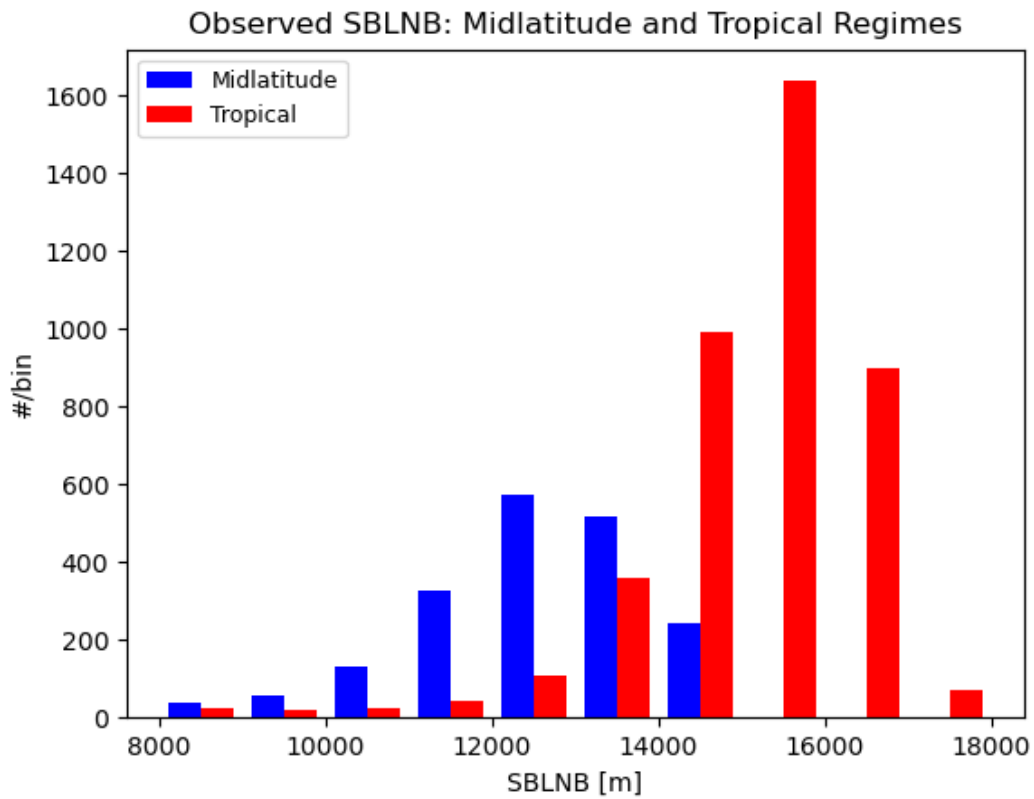
Figure 54. Histogram displaying observed distributions for SBLNB categorized by regime type.

Midlatitude campaigns (blue) and tropical campaigns (red).
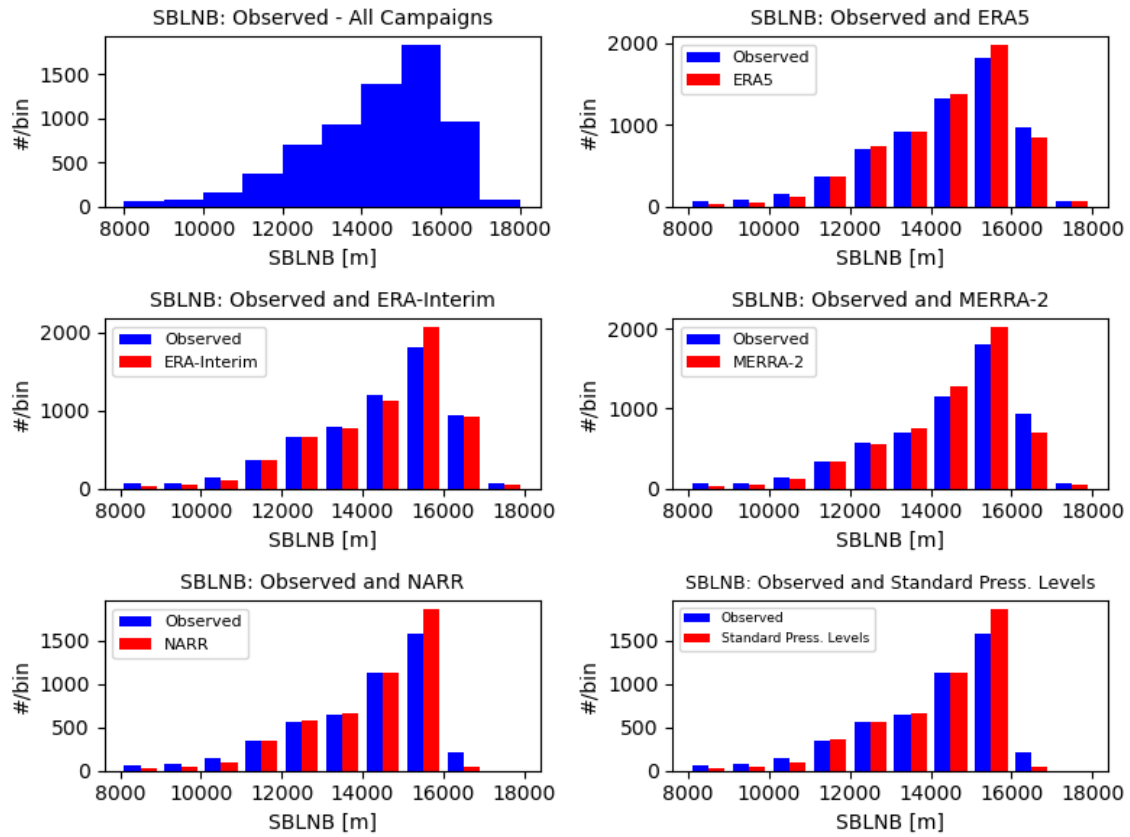
Figure 55. Subplots of histograms displaying MULNB for all campaigns. Each subplot compares observed (blue) to model/reanalysis interpolated (red) SBLNB.
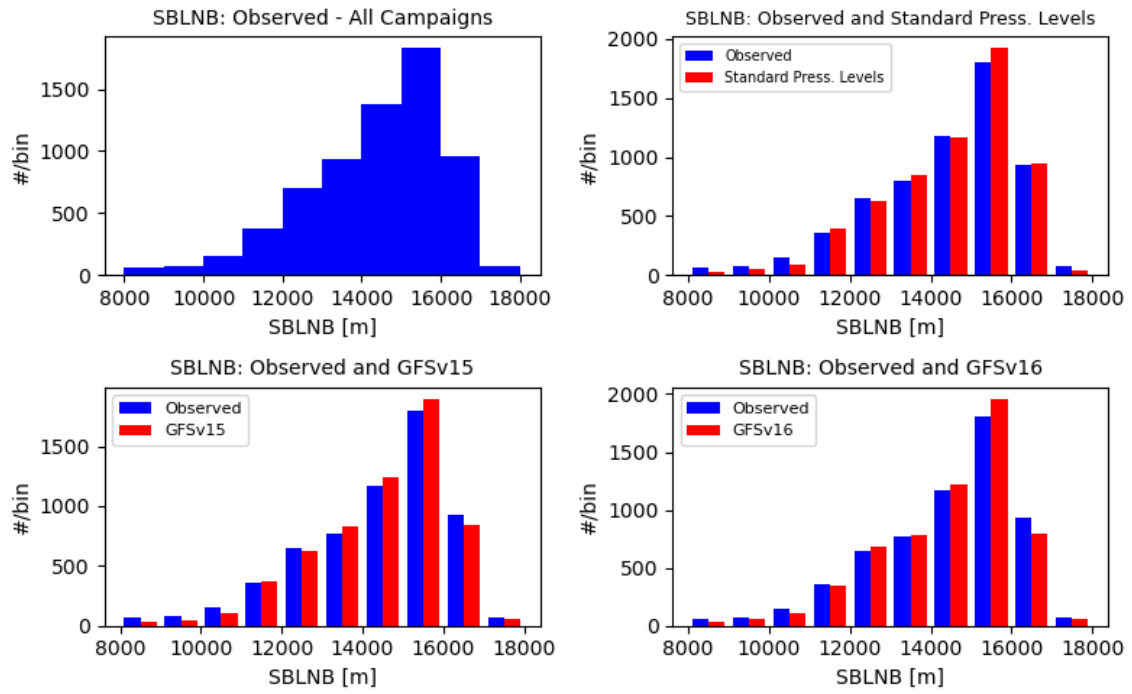
Figure 56. Same as in Fig. 55, but displaying operational model interpolated sets.

Table 4. Correlation coefficients of calculated convective parameters. Shaded boxes represent stronger correlations.

Parameters	ERA5	ERA-Interim	MERRA-2	NARR	Standard Press. Levels	GFSv15	GFSv16
MLCAPE	0.95	0.92	0.94	0.94	0.94	0.96	0.96
MUCAPE	0.97	0.96	0.93	0.94	0.93	0.96	0.97
SBCAPE	0.98	0.98	0.97	0.98	0.98	0.98	0.98
MLCIN	0.98	0.97	0.99	0.99	0.99	0.99	0.98
MUCIN	0.99	0.98	0.96	0.96	0.96	0.98	0.99
SBCIN	0.99	0.99	0.98	0.98	0.98	0.99	0.99
6 km Bulk Shear	0.99	0.98	0.99	0.98	0.98	0.99	0.99
3 km Bulk Shear	0.99	0.99	0.99	0.99	0.98	0.99	0.99
Cap Strength	0.89	0.78	0.85	0.83	0.82	0.82	0.94

CHAPTER 5

DISCUSSION

In Chapter 4, results showed that certain convective environmental parameters displayed clear increasing biases with decreasing vertical resolution. In order to further investigate this trend, CAPE, LNB, and capping inversion strength were further analyzed through the use of example cases.

5.1. Example Cases

5.1.1. Underestimation of CAPE

As discussed in the previous chapter, results exhibited an underestimation bias for CAPE cases above 3000 J/kg. To further investigate this bias, example soundings from each regime (tropical or midlatitude) were selected. In order to ensure selected cases were representative of the observed bias, soundings needed to have at least 3,000 J/kg of MLCAPE. Additionally, the selected example cases were representative of cases that had large underestimations (>1,000 J/kg).

During the process of selecting example cases, it was observed that soundings that met the above criteria also commonly had no LNB (sounding cut off early). Some soundings cut off during the more buoyant part of the sounding effectively cutting off the CAPE calculation. In Fig. 56, a sounding selected from DC3 presents an example in which the lifted profiles remain positively buoyant at the max height of the sounding. In extreme cases such as in Fig. 57, thermodynamic calculations such as CAPE and LNB are impacted. These soundings were not removed from the overall dataset used in this project, and they therefore did have some impact on the overall statistics. As can be seen in Fig. 57, the observed sounding profile has a maximum height of approximately 9 km while the profile

interpolated to standard pressure levels reached only approximately 8 km. This reduction in one km of area in the "fat" part of the buoyancy significantly reduced the CAPE in the interpolated sounding. Future studies should remove all soundings with this sort of profile.

Fig. 57 displays an overview of the observed and interpolated model vertical profiles from a sounding selected from the DC3 field project. Observed temperature and dewpoint profiles are plotted as solid lines while interpolated temperature and dewpoint profiles are in the dashed lines. Lifted parcel profiles are also plotted with the observed profiles plotted as dashed lines and the interpolated as dotted lines. Overall, the temperature and dewpoint profile are adequately represented by the dataset interpolated to standard pressure levels. Some exceptions include marginal smoothing of the temperature and dewpoint profiles in presence of sharper changes in values (e.g., capping inversion). Differences of approximately 1,379 J/kg (MLCAPE), 1,130 J/kg (SBCAPE), and 1,137 J/kg MUCAPE between the observed and interpolated soundings are calculated demonstrating a considerable underestimation (Fig. 58). The marginal smoothing of the sharper temperature and dewpoint changes in the vertical profile were a likely factor for the underestimation of CAPE. Fig. 59 displays the same sounding except focused in the first 7 km and displaying the surface-based lifted parcel profile for easier viewing. It became clearer that the interpolated profiles in the first 2 km were more accurately represented, but degraded slightly after that in proximity to larger gradients in the observed dewpoint and temperature profiles.

Another evident feature was in the lifted parcel profiles as the interpolated profile diverged from the observed profiles around 6 km, in the vicinity of the freezing level (Fig. 58, Fig. 59). Limited points in the interpolated profiles may create a "lag" at which the data

points reach the freezing level compared to the high-resolution data points. Ice processes and associated latent heat release near this level can subsequently impact the buoyancy of the profile; therefore, a lag in timing could result in a less buoyant interpolated lifted profile. In Fig. 60, profiles are plotted as data points as opposed to the traditional lines. The high-resolution observed profiles for temperature and dewpoint take on the appearance of lines due to their high density of points while the points associated with standard pressure levels are quite visible. Near the freezing level, it is visible that there is a large distance to the next interpolated point once the freezing level was reached likely contributing to the lag issue. The slight deviation of the lifted interpolated parcel profile from the observed before the freezing level may also suggest that this is a cumulative effect as the parcel is lifted past other significant levels for latent heating effects (e.g., LCL).

Fig. 61 compares the observed profile to a higher resolution interpolated set, ERA5. Sharper features are better represented by the interpolated set compared to the standard pressure levels (Fig. 58). The CAPE differences of 1,136 J/kg (MLCAPE), 903 J/kg (SBCAPE), and 910 J/kg MUCAPE demonstrate a smaller degree of underestimation by ERA5. Fig. 62, displays the plotted profiles similar to Fig. 60, but instead displays ERA5 data points. The higher resolution of ERA5 is quite evident as there are considerably more data points in the profile compared to standard pressure levels in Fig. 60. In addition, the divergence of the interpolated lifted profiles from the observed are also visible in this example near the freezing level.

The next example features a sounding selected from the DYNAMO field project representative of a tropical regime. Fig. 63 displays an overview of the vertical profiles for the observed and interpolated (standard pressure levels). Overall, the temperature and

dewpoint profiles were adequately represented by the interpolated set. Minimal smoothing in the interpolated dewpoint profile is displayed compared to the observed. The dewpoint profile is sufficiently represented in the first 2 km; however, sharper dewpoint changes beyond 2 km resulted in considerable smoothing. Quantitatively, this case had calculated underpredictions of 1,300 J/kg (MLCAPE) and 667 J/kg (SB/MUCAPE). The same feature of the lifted interpolated profile diverging of the observed near the freezing level is also seen in this example.

Fig. 64, displays the same example sounding except the interpolated model set is now ERA5, a much higher vertical resolution reanalysis model. The profiles both look better represented overall compared to the observed profile, being especially visible in the dewpoint profile. In regards to CAPE calculations, there are some slight improvements as the degree of underestimation slightly decreased when using ERA5. Respectively, differences from the observed were 1,183 J/kg (MLCAPE) and 610 J/kg (SB/MUCAPE). The previously mentioned feature of the interpolated lifted profile becoming less buoyant than the observed near the freezing level is still quite visible as well (Fig. 64).

5.1.2. Underprediction of Capping Inversion Strength

Capping inversion strength for interpolated profiles displayed a clear negative bias for stronger cap cases (Fig. 39). A case was selected from the VORTEX2 campaign dataset that reflected a strong cap case (.075°C/m). Fig. 65 displays a comparison of profiles interpolated to reanalysis model levels of NARR (29 levels) and ERA5 (137 levels) to the observed. Temperature and dewpoint profiles for the interpolated sets are plotted as dashed lines and the observed profiles are plotted as solid lines. The NARR interpolated temperature profile displayed the largest degree of smoothing of the capping inversion. In

comparison to NARR, the ERA5 interpolated temperature profile better represented the strength of the cap; however, some differences in strength and depth of the cap are still notable. Both NARR and ERA5 interpolated profiles underestimated the observed cap strength with the NARR magnitude of .022°C/m and ERA5 magnitude of .028°C/m. Interestingly, the calculated values from NARR and ERA5 aren't far from each other despite a large difference in the number of levels in this example. As shown in Fig. 11, NARR overall has a larger Δz between levels than ERA5. Towards the level of the cap (approximately 2 km), Δz increases for both reanalysis models which contributes to the underestimation of the cap strength. Although NARR has fewer levels, they are distributed in such a way that Δz doesn't increase rapidly in the first few kilometers which may explain why the NARR calculated cap strength was closer to ERA5.

The same example case from VORTEX2 was utilized for analyzing the impacts of interpolating the observed profiles to vertical levels of global operational models, GFSv15 (64 levels) and GFSv16 (127 levels, most recently implemented). Fig. 66 compares the GFS interpolated profiles with the observed. The GFSv15 temperature profile demonstrates considerable smoothing of the capping inversion resulting in a weaker positive lapse rate and a cap structure occurring over a greater depth than the observed. This smoothing resulted in a significantly weaker cap strength of .016°C/m, a considerable underestimation from the observed strength of .075 °C/m. Fig. 11 displays vertical resolution in the GFSv15 to quickly drop off within the first few kilometers resulting in difficulty representing the strong capping inversion at the cap height. GFSv16 shows the best representation of the capping inversion out of all the interpolated sets mentioned. In Fig. 66, the temperature profile of GFSv16 appears close to the observed temperature profile. This improvement in

representing the cap is quantitatively supported by a calculated cap strength of .056°C/m, considerably closer to the observed. The smaller magnitude of underprediction comes as no surprise due to the larger number of levels and higher density of levels in the lower layer (Fig. 11). The increase in number of vertical levels in the GFSv16 shows improvements in representing sharper features in the vertical profile which can have positive implications for the performance of this operational model in forecasting potentially convective environments. Given the relation of the capping inversion to CIN calculations, future work should determine if there is a correlation of high cap cases to underprediction of CIN to further illustrate the impact on other parameters.

5.2. Broader Impacts

Results regarding kinematic parameters agreed with previous work (King and Kennedy 2019; Gensini et al. 2014; Taszarek et al. 2021) as kinematic parameters were strongly correlated to the observed. CAPE calculations displayed a consistent negative bias in this study which corresponds well to results in Taszarek et al. (2021). For select reanalyses, a negative bias for CAPE calculations was determined in King and Kennedy (2019); however, NARR and JRA-55 displayed the smallest biases out of the reanalyses analyzed. Gensini et al. (2014) found regional biases and a general overestimation bias for thermodynamic parameters such as CAPE which differed from the results of the study. However, other factors (e.g., low-level moisture fields) relating to the reanalysis (NARR) may have contributed to the this observed bias. The mentioned studies exhibited similar results despite differing methodologies to this study as this study did not utilize reanalysis model data.

On a similar note, since this study simplistically interpolated high-resolution sounding data to match other models, other factors associated with model runs such as impacts of data assimilation or parameterizations (e.g., boundary layer, vertical advection schemes) were not considered. Errors associated with data assimilation and parameterizations could further degrade the representation of the vertical profile and its subsequent parameter calculations. Previous work investigated the linkage of model-related factors to issues representing the capping inversions and other convective parameters. Planetary boundary layer schemes were linked to poorly resolved capping inversions with no particular scheme improving the representation (Burlingame et al. 2017). Another study concluded that the addition of vertical levels did not improve depiction of the capping inversion (Kain and Coauthors 2017) which differs from the results of this study; these results show that errors due to parameterizations and initialization dominate degradation due to vertical resolution. Nevius and Evans (2018) investigated the potential impacts of implicit damping of third-order-accurate vertical advection finite differencing schemes on representation of the capping inversion. Results showed that usage of a fourth-order scheme did not improve the cap, but did show that the capping inversions were consistently weak meaning that other damping mechanisms could be responsible. It was also noted in this study that as a result of the smoothed profile, the negative buoyancy was spread over too deeply of a layer. This was a feature seen in Fig. 66 as GFSv15 weakened the strong cap while also resulting in a larger depth of the inversion itself. While prior studies have shown the significant impact of model processes and initialization on capping inversions, our study highlights the need to consider vertical resolution improvements that complement improvements that reduce model error.

5.3. Future Work

Future work will focus on applying additional quality control procedures to soundings that were cut-off early. As mentioned in the previous section, soundings that were cut off before the LNB was reached will pose issues in the accuracy of CAPE calculations. Sub setting of select parameters is also an area of future work. This would include investigating how select parameters are related with each other in cases of evident bias (e.g., if underestimated CAPE cases consistently correspond to issues in calculating CIN or capping inversion). Correlation analysis can be further expanded within the sub set parameters. Further analysis can be added upon regarding the feature in the lifted profiles near the freezing level as the interpolated profiles become less buoyant than the observed. Direct comparison of the interpolated ERA5 and standard pressure levels lifted parcel profile trajectories may provide more clarity if there are any relative impacts or improvements with increasing vertical resolution.

Figure 57. Plot of height vs. temperature comparing observed T and Td profiles with the interpolated profiles (Standard pressure levels) from a DC3 sounding. Lifted parcel profiles also plotted for the observed and interpolated soundings. Note this sounding has a max observed height of 9 km.

Figure 58. Plot of height vs. temperature comparing observed T and Td profiles with the interpolated profiles (Standard pressure levels) for a DC3 sounding. Lifted parcel profiles also plotted for the observed and interpolated soundings.
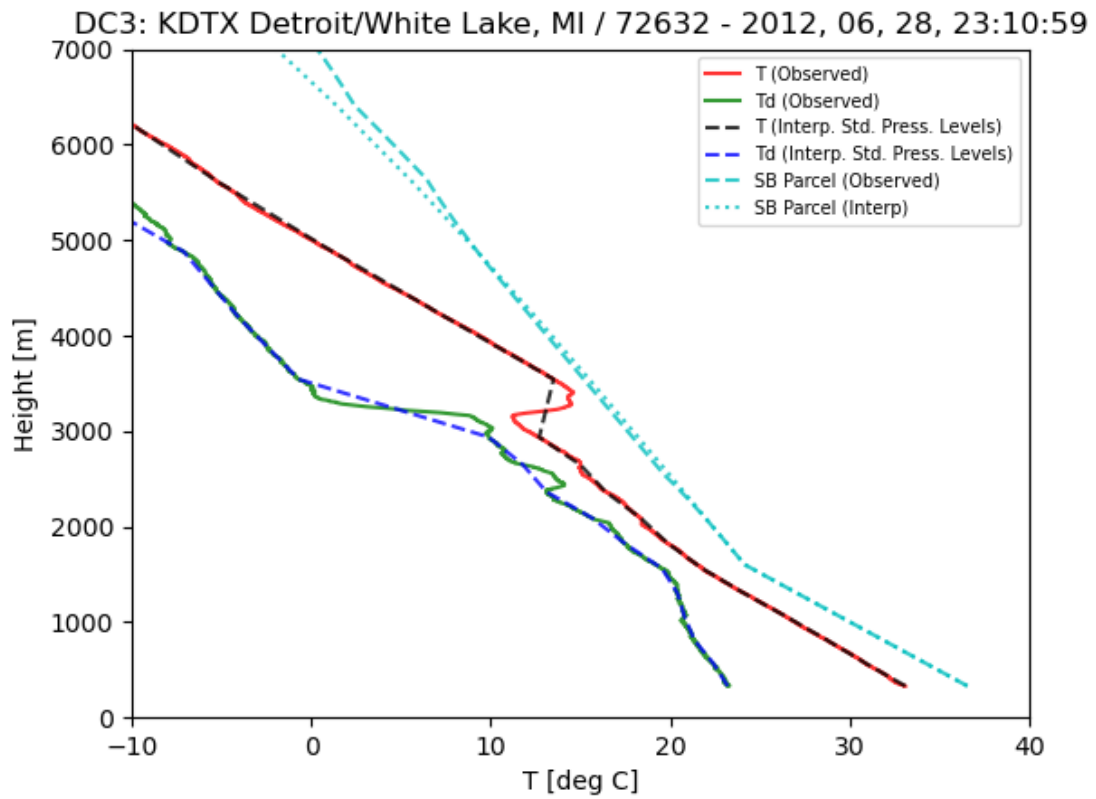
Figure 59. Same as in Fig. 58 except focused in the first 7 km and only displaying the surface-based lifted profile as the parcel profile.
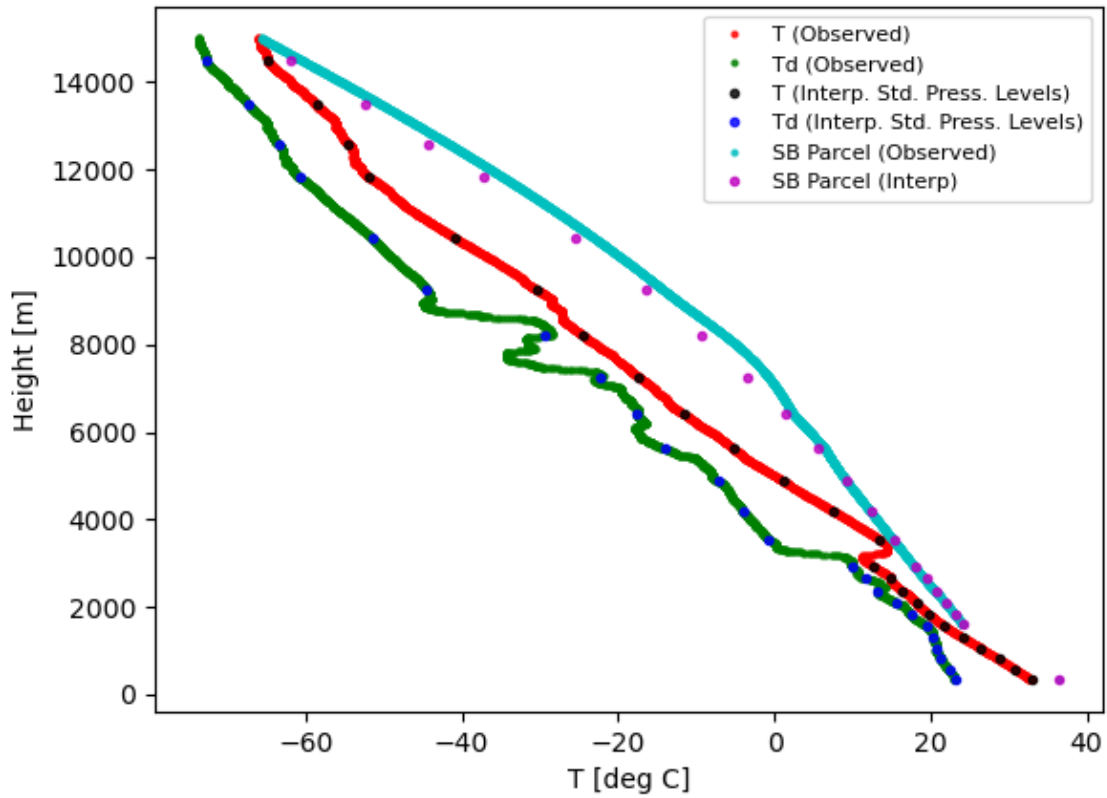
Figure 60. Plot of height vs. temperature comparing observed T and Td profiles with the interpolated profiles (Standard pressure levels) for a DC3 sounding. Surface-based lifted parcel profile is plotted for both interpolated and observed. Profiles are plotted with circular markers instead of lines (see legend).
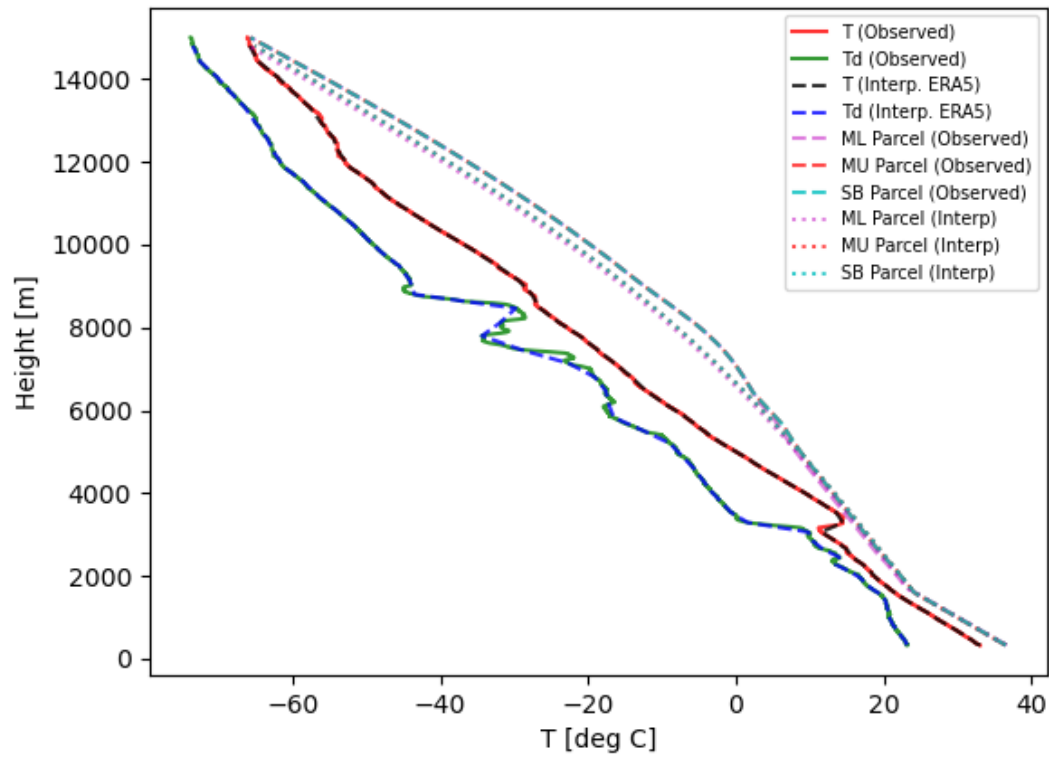
Figure 61. Plot of height vs. temperature comparing observed T and Td profiles with the interpolated profiles (Standard pressure levels) for a DC3 sounding. Lifted parcel profiles also plotted for the observed and interpolated soundings.
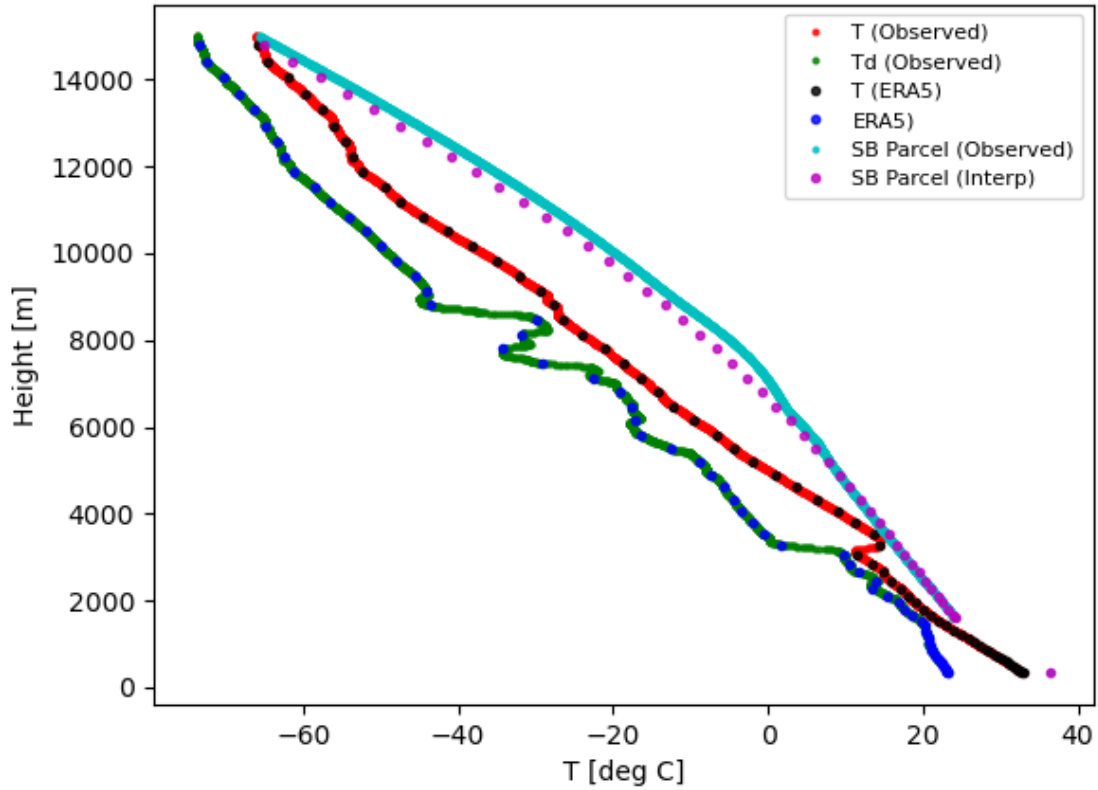
Figure 62. Plot of height vs. temperature comparing observed T and Td profiles with the interpolated profiles (ERA5) for a DC3 sounding. Lifted parcel profiles also plotted for the observed and interpolated soundings. Profiles are plotted with circular markers instead of lines (see legend).
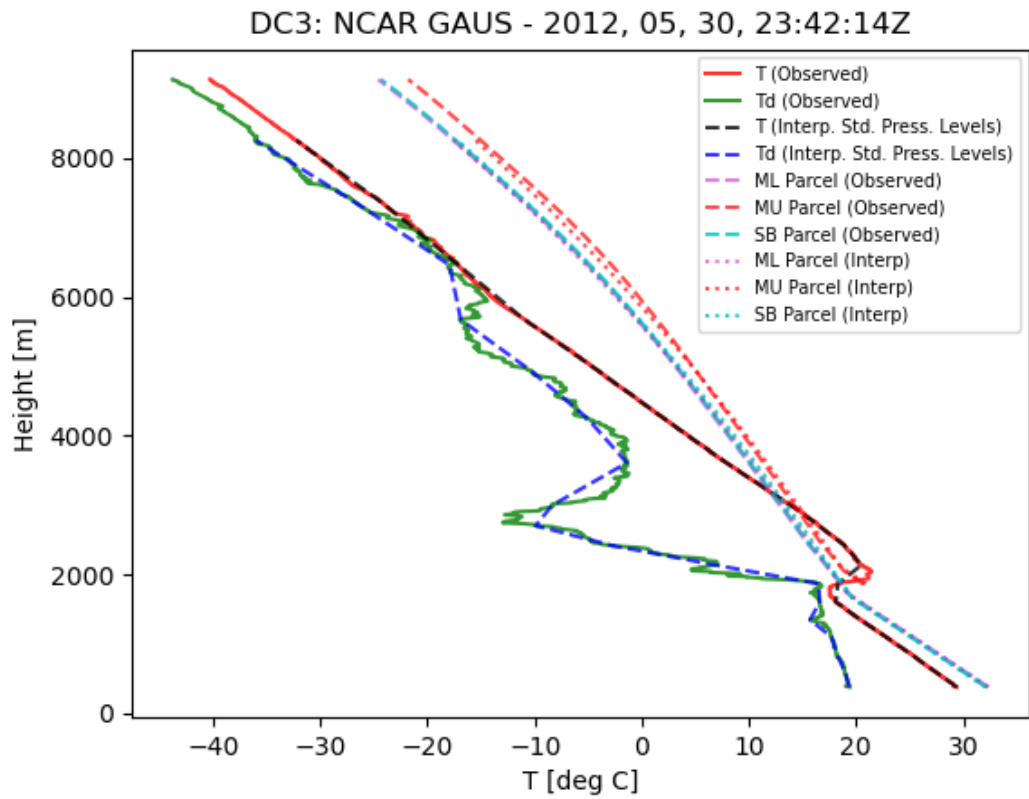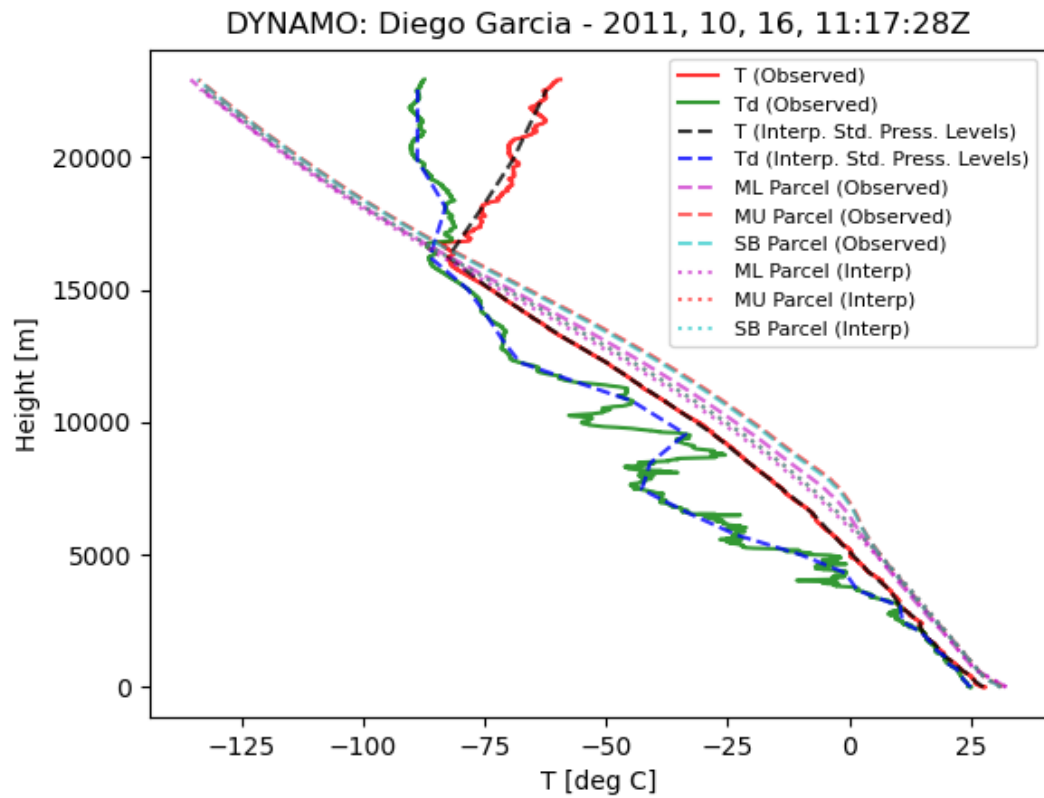
Figure 63. Plot of height vs. temperature comparing observed T and Td profiles with the interpolated profiles (Standard pressure levels) for a DYNAMO sounding. Lifted parcel profiles also plotted for the observed and interpolated soundings.
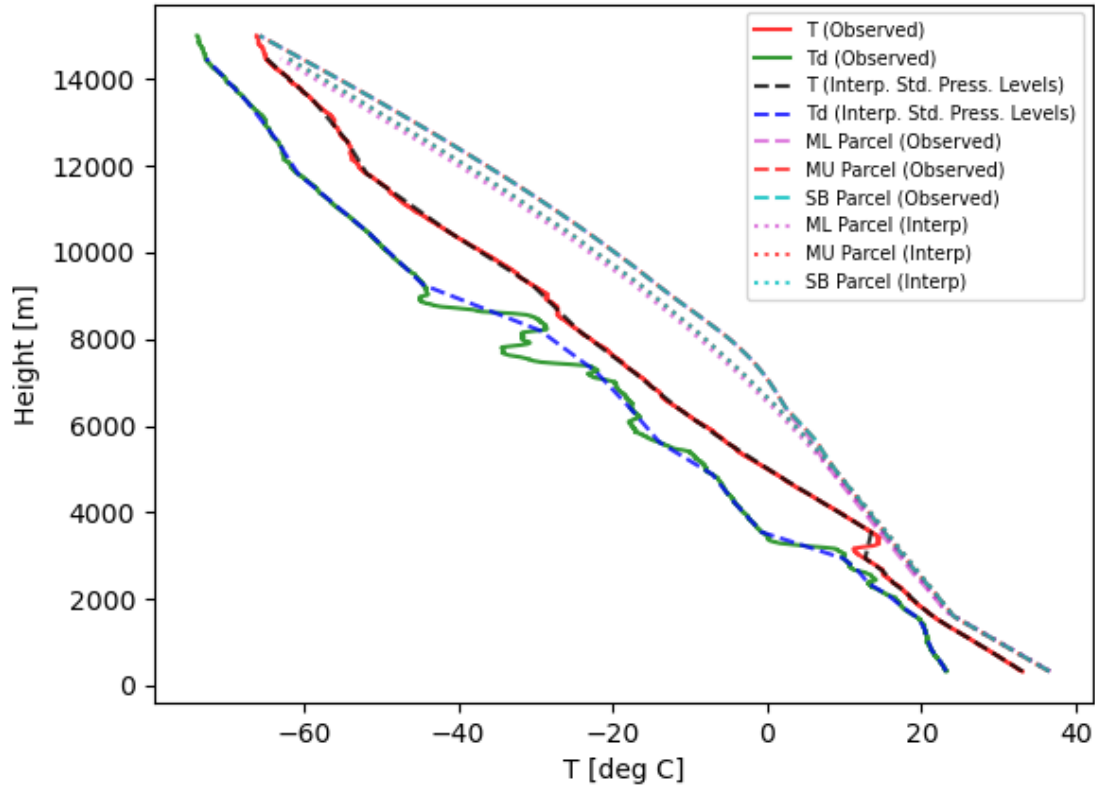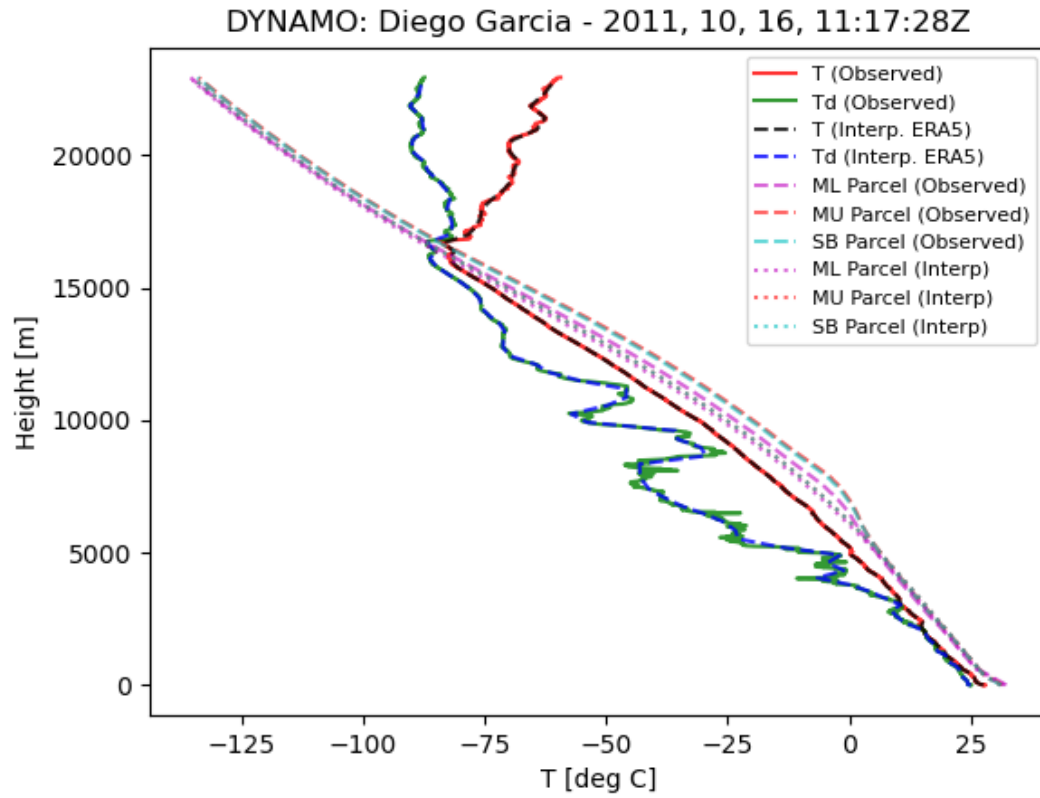
Figure 64. Plot of height vs. temperature comparing observed T and Td profiles with the interpolated profiles (ERA5) for a DYNAMO sounding. Lifted parcel profiles also plotted for the observed and interpolated soundings.
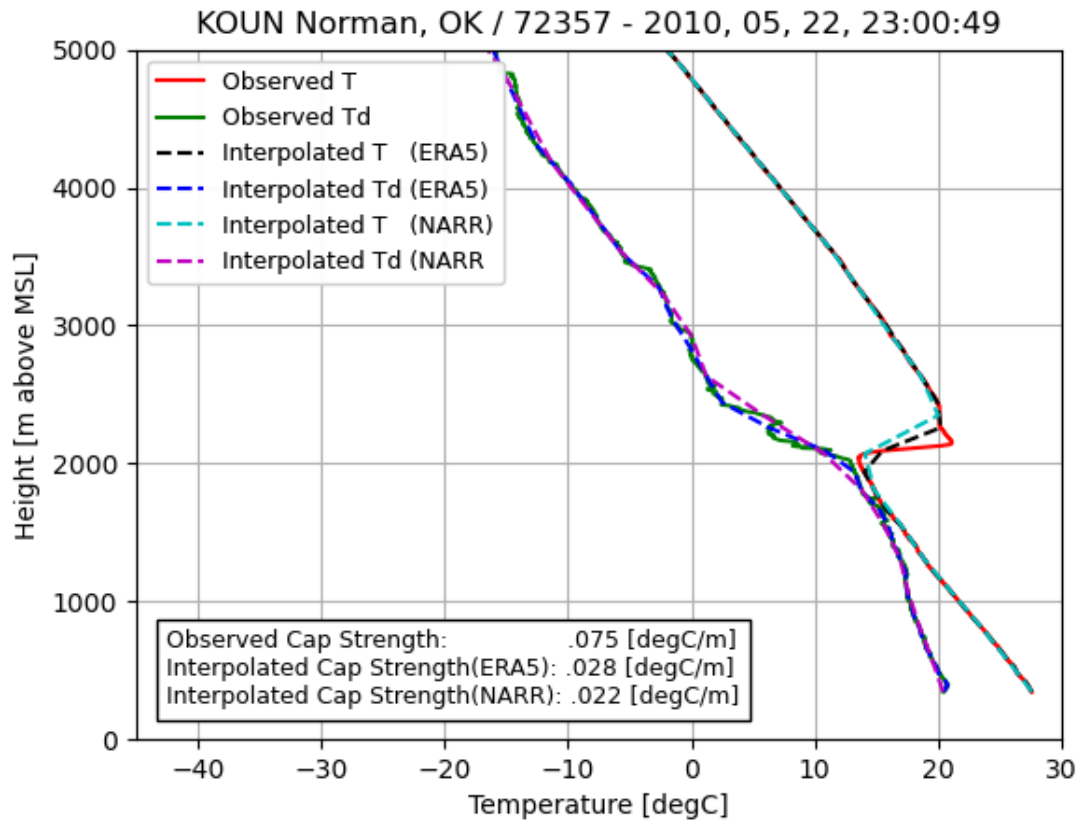
Figure 65. Plot of height vs. temperature of the first 5 km comparing observed temperature and dewpoint profiles to profiles interpolated to reanalysis levels of ERA5 and NARR. Note colors in legend differ slightly from previous CAPE/LNB examples soundings. Bottom left box displays the calculated cap strength values.
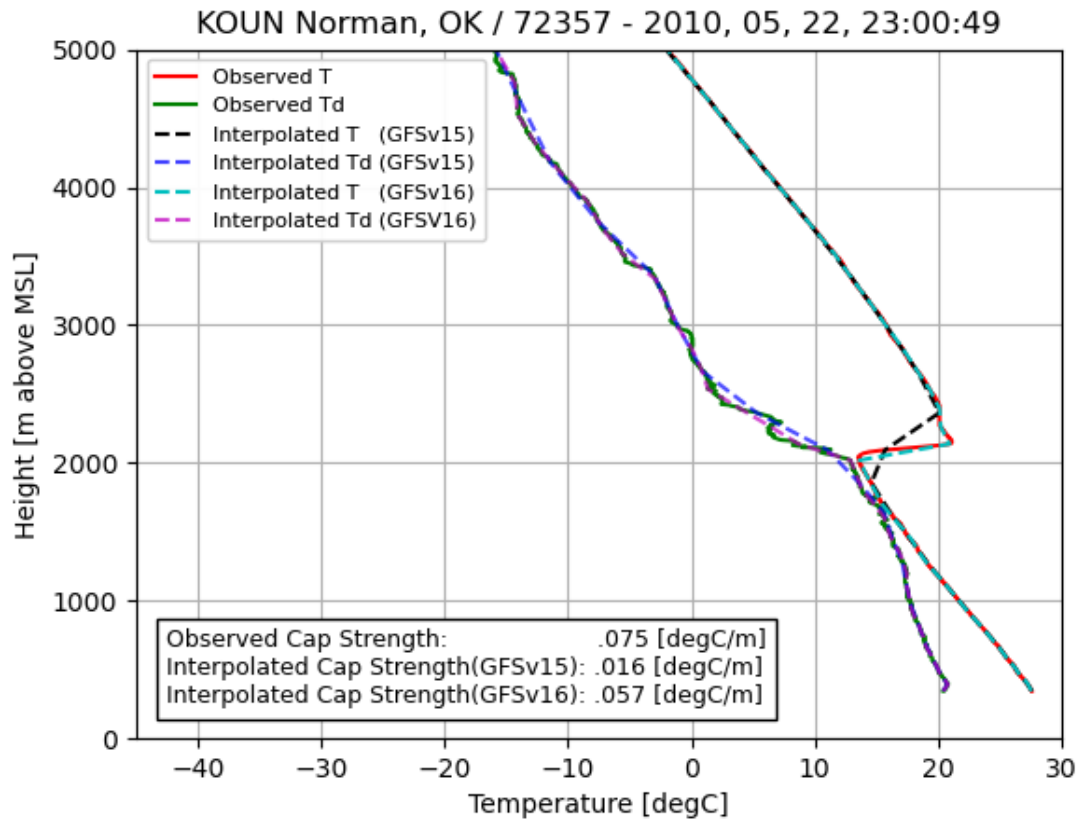
Figure 66. Plot of height vs. temperature of the first 5 km comparing observed temperature and dewpoint profiles to profiles interpolated to model levels for GFSv15 and GFSv16. Note colors in legend differ slightly from previous CAPE/LNB examples soundings. Bottom left box displays the calculated cap strength values.

CHAPTER 6

CONCLUSIONS

In this study, high resolution radiosonde data was interpolated to the pressure levels of various reanalyses and operational models to determine if lower vertical resolution impacted the ability of a model to represent a potentially convective environment. High resolution sounding data were retrieved from multiple field projects from both midlatitude and tropical regime types. Sounding data analyzed reflected potentially convective environments with MLCAPE values of at least 500 J/kg (tropical) or 1,000 J/kg (midlatitude). Select convective parameters were calculated for both observational and interpolated datasets to evaluate to the performance of different vertical spacings. Findings are summarized below:

- Kinematic variables (e.g., 0-3/0-6 km bulk shear) experienced little to no impacts from reduced vertical resolution as all interpolated sets were highly correlated to the observed. This result is consistent with the results of King and Kennedy (2019), Gensini et al. (2014), and Taszarek et al. (2021).

- CAPE was consistently underestimated for cases greater than 3,000 J/kg. Although calculated correlation coefficient indicated a strong correlation, scatterplots signified a negative bias in higher CAPE cases. The example case analyzed in Chapter 5 showed that ERA5, with high vertical resolution, underestimated CAPE to a lesser extent than at standard pressure levels, which has considerably lower

vertical resolution in comparison. This corresponds to previous work that has noted this negative bias (e.g., Taszarek et al. 2021).

- CIN calculations showed no consistent bias. The interpolated set calculations were overall well correlated to the observed values for the three parcel types. Vertical resolution alone did not significantly impact the accuracy of CIN calculations. This finding differed from previous work where lower correlations were associated with CIN (e.g., King and Kennedy 2018; Taszarek et al. 2021). However, it is important to note that model-related limitations (e.g., parameterizations) aren't reflect in the results of this study unlike previous work due to differing methodology.

- Representation of the capping inversion is sensitive to both the number and distribution of vertical levels. Models with high vertical resolution, especially in the first several kilometers, had stronger correlations to the observed cap strength than models with lower vertical resolution. In the example case (Chapter 5), GFSv15 had issues resolving the cap due to its rapid decrease in vertical resolution near the cap height. In contrast, the GFSv16 interpolated set displayed a considerable improvement in representation of the cap owing to its high resolution and higher density of vertical levels near the cap height. It is important to note that other factors such as PBL and vertical advection schemes would likely impact the representation of the capping inversion in model soundings (Burlingame et al. 2017; Nevius and Evans 2018).

In summary, coarsening the vertical resolution decreased the accuracy of convective parameters with the profiles with the coarsest vertical resolution generally performing the worst. Although not reflected in the results of this study, model-related factors (e.g., parameterizations, data assimilation) mentioned in previous work (e.g., Gensini et al. 2014; Taszarek et al. 2021) are also important to consider when utilizing reanalysis data or operational model runs. Atmospheric reanalyses are a valuable means of analyzing trends and distributions of favorable convective environments. The most recently released reanalyses, ERA5, contains 137 raw levels, but is easiest to download as the 37 derived levels (standard pressure levels), which severely degrades the ability to correctly represent convective parameters such as CAPE. Representation of sharp structures in the vertical profile such as the capping inversion is also negatively impacted by the use of models with lower vertical resolution. When using renalyses data, it is important to be aware of the biases presented in this research. Biases due to vertical resolution also impact information gleaned from operational forecasts. This may potentially impact the accuracy of convection initiation and location of convection which are important factors in a convective forecast. Results of this work, based off of vertical resolution impacts alone, support the greater reliability of using ERA5 native levels for analyzing potentially convective environments as opposed to using the derived levels. In agreement with Taszarek et al. (2021), if available, the utilization of ERA5 native levels is recommended.

REFERENCES

Aligo, E. A., W. A. Gallus Jr., and M. Segal, 2009: On the impact of WRF model vertical grid resolution on Midwest summer rainfall forecasts. *Wea. Forecasting*, **24**, 575–594, https://doi.org/10.1175/2008WAF2007101.1.

Atmospheric Radiation Measurement (ARM) user facility. 2014. Balloon-Borne Sounding System (SONDEWNPN). 2014-01-01 to 2015-12-01, ARM Mobile Facility (MAO) Manacapuru, Amazonas, Brazil; AMF1 (M1). Compiled by E. Keeler, R. Coulter and J. Kyrouac. ARM Data Center, http://dx.doi.org/10.5439/1021460.

Barber, K. A., G. L. Mullendore, and M. J. Alexander, 2018: Out-of-cloud convective turbulence: Estimation method and impacts of model resolution. *J. Appl. Meteor. Climatol.*, **57**, 121–136, https://doi.org/10.1175/JAMC-D-17-0174.1.

Barth, M. C., and Coauthors, 2015: The Deep Convective Clouds and Chemistry (DC3) field campaign. *Bull. Amer. Meteor. Soc.*, **96**, 1281–1309, https://doi.org/10.1175/BAMS-D-13-00290.1.

Blanchard, D. O., 1998: Assessing the vertical distribution of convective available potential energy. *Wea. Forecasting*, **13**, 870-877, *https://doi.org/10.1175/1520-0434(1998)013<0870:ATVDOC>2.0.CO;2.*

Blumberg, W. G., K. T. Halbert, T. A. Supinie, P. T. Marsh, R. L. Thompson, and J. A. Hart, 2017: SHARPpy: An open source sounding analysis toolkit for the atmospheric sciences. *Bull. Amer. Meteor. Soc.*, **98**, 1625–1636, https://doi.org/10.1175/BAMS-D-15-00309.1

Brooks, H. E., J. W.Lee, and J. P.Craven, 2003: The spatial distribution of severe thunderstorm and tornado environments from global reanalysis data. *Atmos. Res.*, **67–68**, 73–94, https://doi.org/10.1016/S0169-8095(03)00045-0.

Bryan, G. H., J. C., Wyngaard , and J. M. Fritsch, 2003: Resolution Requirements for the Simulation of Deep Moist Convection. *Mon. Wea. Rev.*, **131**, 2394-2416, https://doi.org/10/1175/1520-0493(2003)131<2394:RRFTSO>2.0.CO;2

Bunkers, M. J., Klimowski, B. A., and Zeitler, J. W.: The Importance of parcel choice and the measure of vertical wind shear in evaluating the convective environment, Preprints, 21st Conf. Severe Local Storms, San Antonio, American Meteorological Society, J117–J120, 11–16 August 2002.

Burlingame, B. M., C. Evans, and P. J. Roebber, 2017: The influence of PBL parameterization on the practical predictability of convection initiation during the Mesoscale Predictability Experiment (MPEX). *Wea. Forecasting*, 32, 1161–1183, https://doi.org/10.1175/WAF-D-16-0174.1.

Colby, F. P., Jr., 1984: Convective inhibition as a predictor of convection during AVE-SESAME II. *Mon. Wea. Rev.,* **112,** 2239–2252, *https://doi.org/10.1175/1520-0434(1998)013<0870:ATVDOC>2.0.CO;2.*

Coniglio, M. C., J. Correia, P. T. Marsh, and F. Kong, 2013: Verification of convection-allowing WRF Model forecasts of the planetary boundary layer using sounding observations. *Wea. Forecasting*, **28**, 842–862, https://doi.org/10.1175/WAF-D-12-00103.1.

Coniglio, M. C., and M. D. Parker, 2020: Insights into supercells and their environments from three decades of targeted radiosonde observations. *Monthly Weather Review*, 1–68, https://doi.org/10.1175/MWR-D-20-0105.1

Craven, J. P., R. E. Jewell, and H. E. Brooks, 2002: Comparison between Observed Convective Cloud-Base Heights and Lifting Condensation Level for Two Different Lifted Parcels. *Wea. Forecasting*, **17**, 885–890, https://doi.org/10.1175/1520-0434(2002)017<0885:CBOCCB>2.0.CO;2.

Craven, J. P., and H. E.Brooks, 2004: Baseline climatology of sounding derived parameters associated with deep, moist convection. *Natl. Wea. Dig.*, **28**, 13–24.

Dee, D. P. and Coauthors, 2011: The ERA-Interim reanalysis: configuration and performance of the data assimilation system. *Quarterly Journal of the Royal Meteorological Society*, https://doi.org/10.1002/qj.828

Doswell, C., and E. Rasmussen, 1994: The effect of neglecting the virtual temperature correction on CAPE calculations. *Wea. Forecasting*, **9,** 625–62

Gartzke, J., R. Knuteson, G. Przybyl, S. Ackerman, and H. Revercomb, 2017: Comparison of Satellite-, Model-, and Radiosonde-Derived Convective Available Potential Energy in the Southern Great Plains Region. *J. Appl. Meteor. Climatol.*, **56**, 1499–1513, https://doi.org/10.1175/JAMC-D-16-0267.1

Geerts, B., and Coauthors, 2017: The 2015 Plains Elevated Convection At Night Field Project. *Bull. Amer. Meteor. Soc.*, **98**, 767–786, https://doi.org/10.1175/BAMS-D-15-00257.1.

Gelaro, R., and Coauthors, 2017: The Modern-Era Retrospective Analysis for Research and Applications, version 2 (MERRA-2). *J. Climate*, **30**, 5419–5454, https://doi.org/10.1175/JCLI-D-16-0758.1.

Gensini, V. A., and W. S.Ashley, 2011: Climatology of potentially severe convective environments from North American regional reanalysis. *Electron. J. Severe Storms Meteor.*, **6** (8), http://www.ejssm.org/ojs/index.php/ejssm/article/viewArticle/85.

Gensini, V. A., T. L. Mote, and H. E. Brooks, 2014: Severe-Thunderstorm Reanalysis Environments and Collocated Radiosonde Observations. *J. Appl. Meteor. Climatol.*, **53**, 742–751, https://doi.org/10.1175/JAMC-D-13-0263.1.

Halverson, J. B., T. Rickenbach, B. Roy, H. Pierce, and E. Williams, 2002: Environmental Characteristics of Convective Systems during TRMM-LBA. *Mon. Wea. Rev.*, **130**, 1493–1509, https://doi.org/10.1175/1520-0493(2002)130<1493:ECOCSD>2.0.CO;2.

Hanna, S. R., and R. Yang, 2001: Evaluations of mesoscale models' simulations of near-surface winds, temperature gradients, and mixing depths. *J. Appl. Meteor.*, **40**, 1095–1104, https://doi.org/10.1175/1520-0450(2001)040<1095:EOMMSO>2.0.CO;2.

Hersbach, H., and Coauthors, 2020: The ERA5 global reanalysis. *Quart. J. Roy. Meteor. Soc.*, **146**, 1999–2049, https://doi.org/10.1002/qj.3803.

Homeyer, C. R., K. P. Bowman, and L. L. Pan, 2010: Extratropical tropopause transition layer characteristics from high-resolution sounding data. *J. Geophys. Res.*, **115**, D13108, https://doi.org/10.1029/2009JD013664.

Homeyer, C. R., 2015: Numerical simulations of extratropical tropopause-penetrating convection: Sensitivities to grid resolution. *J. Geophys. Res.*, **120**, 7174-7188, DOI: https://doi.org/10.1002/2015JD023356

Kain, J. S., and Coauthors, 2017: Collaborative efforts between the United States and United Kingdom to advance prediction of high-impact weather. *Bull. Amer. Meteor. Soc.*, **98**, 937–948, https://doi.org/10.1175/BAMS-D-15-00199.1.

Kalnay, E., and Coauthors, 1996: The NCEP/NCAR 40-Year Reanalysis Project. *Bull. Amer. Meteor. Soc.*, **77**, 437–471, https://doi.org/10.1175/1520-0477(1996)077<0437:TNYRP>2.0.CO;2.

King, A. T., and A. D. Kennedy, 2019: North American Supercell Environments in Atmospheric Reanalyses and RUC-2. *J. Appl. Meteor. Climatol.*, **58**, 71–92, https://doi.org/10.1175/JAMC-D-18-0015.1.

Markowski ,P. and Y., Richardson, 2010, *Mesoscale Meteorology in Midlatitudes,* Wiley, 397

Martin, S. T., and Coauthors, 2016: Introduction: Observations and modeling of the Green Ocean Amazon (GoAmazon2014/5). Atmos. Chem. Phys., **16**, 4785–4797, doi:https://doi.org/10.5194/acp-16-4785-2016.

May, R. M., Arms, S. C., Marsh, P., Bruning, E., Leeman, J. R., Goebbert, K., Thielen, J. E., and Bruick, Z., 2020: MetPy: A Python Package for Meteorological Data. Unidata, https://github.com/Unidata/MetPy, https://doi.org/10.5065/D6WW7G29.

Mesinger, F., and Coauthors, 2006: North American Regional Reanalysis. *Bull. Amer. Meteor. Soc.*, **87**, 343–360, https://doi.org/10.1175/BAMS-87-3-343.

Mullendore, G. L., A. J. Homann, K. Bevers, and C. Schumacher, 2009: Radar reflectivity as a proxy for convective mass transport. *Journal of Geophysical Research: Atmospheres*, **114**, https://doi.org/https://doi.org/10.1029/2008JD011431.

Mullendore, G. L., A. J.Homann, S. T.Jorgenson, T. J.Lang, and S. A.Tessendorf, 2013: Relationship between level of neutral buoyancy and dual-Doppler observed mass detrainment levels in deep convection. *Atmos. Chem. Phys.*, **13**, 181-190, https://doi.org/10.5194/acp-13-181-2013.

Nevius, D. S., and C. Evans, 2018: The influence of vertical advection discretization in the WRF-ARW model on capping inversion representation in warm-season thunderstorm-supporting environments. *Wea. Forecasting*, **33**, 1639–1660, https://doi.org/10.1175/WAF-D-18-0103.1

NOAA/OAR/ESRL PSL, NCEP North American Regional Reanalysis: NARR. *Physical Sciences Laboratory*. https://psl.noaa.gov/data/gridded/data.narr.html

Rochette, S. M., and J. T. Moore, and P, S. Market, 1999: The importance of parcel choice in elevated CAPE computations. Natl. Wea. Dig., **23**, 20-32.

Romero, R., M.Gayà, and C. A.Doswell III, 2007: European climatology of severe convective storm environmental parameters: A test for significant tornado events. *Atmos. Res.*, **83**, 389–404, https://doi.org/10.1016/j.atmosres.2005.06.011.

Rotunno, R., J. B.Klemp, and M. L.Weisman, 1988: A theory for strong, long-lived squall lines.*J. Atmos. Sci.*, **45,** 463–485.

Simpson, J., R. F. Adler, and G. North, 1988: A Proposed Tropical Rainfall Measuring Mission (TRMM) Satellite. Bull. Amer. Meteor. Soc., 69, 278-295, https://doi.org/10.1175/1520-0477(1988)069%3C0278:APTRMM%3E2.0.CO;2

Solomon, D. L., K. P. Bowman, and C. R. Homeyer, 2016: Tropopause-Penetrating Convection from Three-Dimensional Gridded NEXRAD Data. *J. Appl. Meteor. Climatol.*, **55**, 465–478, https://doi.org/10.1175/JAMC-D-15-0190.1.

Starzec, M., G. L. Mullendore, and C. R. Homeyer, 2020: Retrievals of Convective Detrainment Heights Using Ground-Based Radar Observations. *Journal of Geophysical Research: Atmospheres*, **125**, e2019JD031164, https://doi.org/https://doi.org/10.1029/2019JD031164.

Taszarek, M., J. T. Allen, H. E. Brooks, N. Pilguj, and B. Czernecki, 2020: Differing trends in United States and European severe thunderstorm environments in a warming climate. *Bull. Amer. Meteor. Soc.*, 1–51, https://doi.org/10.1175/BAMS-D-20-0004.1.

Tesche, T. W., and D. E. McNally, 1999: Comparative evaluation of the MM5 and RAMS3C prognostic meteorological models over the midwestern U.S. for two 1991 LMOS intensive measurement episodes. Alpine Geophysics Rep. AG-90/TS-125, 197 pp. [Available from Coordinating Research Council, Inc., 219 Perimeter Center Parkway, Suite 400, Atlanta, GA 30346.].

Weisman, M. L., and J. B. Klemp, 1982: The dependence of numerically simulated convective storms on vertical wind shear and buoyancy. *Mon. Wea. Rev.*, **110**, 504–520, https://doi.org/10.1175/1520-0493(1982)110<0504:TDONSC>2.0.CO;2.

UCAR/NCAR – Earth Observing Laboratory. 2017. Multi-Network Composite Highest Resolution Radiosonde Data. Version 1.0. UCAR/NCAR – Earth Observing Laboratory. https://doi.org/10.5065/D6TX3CSP.

UCAR/NCAR – Earth Observing Laboratory. 2013. Multi-Network Composite Highest Resolution Upper Air Data. Version 1.0. UCAR/NCAR – Earth Observing Laboratory. https://doi.org/10.5065/D6HH6HDM.

UCAR/NCAR – Earth Observing Laboratory. 2010. Multi-Network Composite Highest Resolution Upper Air Data. Version 1.0. UCAR/NCAR – Earth Observing Laboratory. https://doi.org/10.5065/D6RN366M.

UCAR/NCAR – Earth Observing Laboratory. 2012. Diego Garcia Radiosonde L3 Data (ESC Format). Version 1.0. UCAR/NCAR – Earth Observing Laboratory. https://doi.org/10.5065/D6QF8R2Z.

UCAR/NCAR – Earth Observing Laboratory. 2012. Gan ARM AMF Radiosonde L3 Data (ESC Format). Version 1.0. UCAR/NCAR – Earth Observing Laboratory. https://data.eol.ucar.edu/dataset/347.008.

UCAR/NCAR – Earth Observing Laboratory. 2012. Gan MMS Radiosonde L3 Data (ESC Format). Version 1.0. UCAR/NCAR – Earth Observing Laboratory. https://data.eol.ucar.edu/dataset/347.143.

UCAR/NCAR – Earth Observing Laboratory. 2012. Male Radiosonde L3 Data (ESC Format). Version 1.0. UCAR/NCAR – Earth Observing Laboratory. https://data.eol.ucar.edu/dataset/347.013.

UCAR/NCAR – Earth Observing Laboratory. 2014. R/V Roger Revelle Radiosonde L3.1 Data. Version 1.0. UCAR/NCAR – Earth Observing Laboratory. https://doi.org/10.5065/D6TH8K3Z.

UCAR/NCAR – Earth Observing Laboratory, Ciesielski, P. 2019. CSU TRMM-LBA Sounding Data. Version 1.0. UCAR/NCAR- Earth Observing Laboratory. https://data.eol.ucar.edu/dataset/123.006.

Wurman, J., D. Dowell, Y. Richardson, P. Markowski, E. Rasmussen, D. Burgess, L. Wicker, and H. B. Bluestein, 2012: The Second Verification of the Origins of Rotation in Tornadoes Experiment: VORTEX2. *Bull. Amer. Meteor. Soc.*, **93**, 1147–1170, https://doi.org/10.1175/BAMS-D-11-00010.1.

Yoneyama, K., Japan Agency for Marine-Earth Science and Technology (JAMSTEC). 2013. R/V Mirai Radiosonde L3.1 Data. Version 1.0. UCAR/NCAR – Earth Observing Laboratory. https://data.eol.ucar/dataset/347.137.

Yoneyama, K., C. Zhang, and C. N. Long (2013), Tracking pulses of the Madden-Julian Oscillation, *Bull. Am. Meteorol. Soc.*, **94**, 1871-1891, https://doi.org/10.1175/BAMS-D-12-00157.1